Intermediate Filaments Associate with Aggresome-like Structures and Influence Rate of Cellular Expulsion of Neuronal Disease Aggregates

Authors/affiliations: Meghan Lee Arnold[1], Jason Cooper[1], Rebecca Androwski,[1] Sohil Ardeshna[1], Ilija Melentijevic,[1] Joelle Smart,[1] Ryan J. Guasp[1], Ken C.Q. Nguyen[2], Ge Bai[1], David H. Hall[2], Barth D. Grant[1], Monica Driscoll[1]

[1]Department of Molecular Biology and Biochemistry
Rutgers University, Piscataway, NJ USA, 08855

[2]Department of Neuroscience
Albert Einstein College of Medicine, Rose F. Kennedy Center, Bronx, New York 10461

Corresponding Authors: Monica Driscoll and Barth D. Grant

Email Address: driscoll@biology.rutgers.edu and grant@dls.rutgers.edu
Tel: (848-445-7182) (848-445-7339)

Abstract

In human neurodegenerative diseases, toxic protein aggregates can spread between neurons to promote pathology. In the transparent genetic animal model *C. elegans*, stressed neurons can concentrate fluorescently tagged protein aggregates and organelles and extrude them in large, nearly soma-sized, membrane-bound vesicles called exophers that enter neighboring cells. *C. elegans* exophergenesis may occur by mechanisms analogous to those that enable aggregate spreading in the human brain in neurodegenerative disease. Here we report on aggresome-like biology in stressed *C. elegans* neurons that influences exophergenesis. We show that *C. elegans* intermediate filament proteins IFD-1 and IFD-2 can assemble into juxtanuclear structures with characteristics similar to mammalian aggresomes and document that these intermediate filaments are required cell autonomously for efficient exopher production. IFD-concentrating structures expand with age or neuronal stress level, can associate with neurotoxic polyglutamine expansion protein HttQ74, and depend upon orthologs of mammalian adapter proteins, dynein motors, and microtubule integrity for collection of aggregates into juxtanuclear compartments. IFD homolog human neurofilament light chain hNFL can substitute for *C. elegans* IFD-2 proteins in promoting exopher production, indicating conservation of the capacity of intermediate filaments to influence neuronal extrusion. In sum, we identify an unexpected requirement for specific intermediate filaments, counterparts of human biomarkers of neuronal injury and disease, and major components of Parkinson's disease Lewy bodies, in large vesicle extrusion from stressed neurons.

Introduction

Cellular accumulation of misfolded protein aggregates is a hallmark feature of aging and neurodegeneration that can cause functional decline [1]. Aggregates can be transferred from diseased neurons to nearby cells, via an extracellular spreading process that promotes pathological degeneration [2]. Given that both aggregate accumulation and spreading are prominent features in human neurodegenerative disease pathology, a major goal in neurobiology is to understand the intrinsic and extrinsic mechanisms by which cells manage aggregate toxicity.

Well studied cellular mechanisms that mitigate the deleterious effects of aggregates, including internal aggregate collection/concentration (aggresome formation), and degradation via the ubiquitin-proteasome system or the autophagy-lysosome pathway [3]. We discovered another mechanism of neurotoxic aggregate management that relies on extrinsic degradation—*C. elegans* adult neurons can selectively eject toxic material in large (~3.8μm) membrane-bound vesicles called exophers [4]. Exopher production begins with dynamic collection of aggregates within the neuronal soma, concentration at a pre-exopher domain, and later dramatic outward budding of a nearly soma-sized membrane-bound vesicle that can selectively include damaged organelles and toxic proteins [4, 5] (New Figure 1A, 1B). Exopher contents can be delivered directly to neighboring tissues (the glia-like hypodermis, in the case of *C. elegans* touch-neuron-derived exophers that we have studied most), similar to what has been observed for *Drosophila* [5-7] and mammalian neurons [2]. We speculate that the *C. elegans* exopher mechanism is analogous to the mysterious process by which neurodegenerative

disease-associated aggregates spread from cell to cell to promote pathology in human neurodegenerative disease. Thus, mechanistic dissection of exophergenesis and the transfer of exopher contents to neighboring cells within in the informative *C. elegans* genetics model holds potential to provide insight into critical neurodegenerative disease biology.

Mammalian cells can use adapter proteins to collect and link aggregated protein cargoes to dynein motors that transport them via microtubule tracks to juxtanuclear structures called aggresomes [8-10]. Aggresomes, which are surrounded by intermediate filament mesh-works can be targets for autophagosomes and lysosomes as these organelles attempt degradation of aggresome contents; aggresomes are especially prominent under the stress conditions that result when proteasome and autophagy pathways are overtaxed or impaired. The extent to which mammalian aggresome pathways contribute to spreading mechanisms has not been extensively investigated.

Extrinsic factors (food availability, oxidative stress, osmotic stress [11] , presence of eggs ([11, 12] and our unpublished observations) can markedly influence the level of exopher production. In this study, we sought neuron-intrinsic factors that act to influence exopher production. To investigate molecular requirements for exophergenesis, we conducted a candidate RNAi screen that included aggresome-associated components. Our studies identified a cell autonomous requirement for aggresome-associated intermediate filament (IF) D class proteins IFD-1 and IFD-2 in efficient *C. elegans* exophergenesis. We found that IFD-1 and IFD-2 colocalize to proteostress-sensitive

juxtanuclear inclusions that both associate with aggregating human disease proteins and influence exopher production. We document roles of conserved adapter proteins, dynein motors and microtubule proteins in collection and concentration of offending proteins into IF-associated compartments that are highly reminiscent of mammalian aggresomes and show that human neuronal intermediate filament hNFL can execute cell-autonomous exopher-related functions in *C. elegans* neurons. Our data contribute molecular documentation of *C. elegans* neuronal aggresome formation and provide the first demonstration of aggresome component contributions to stress-associated extrusion of compromised neuronal contents. Mechanistic linking of conserved aggresome-associated neurofilaments with neuronal extrusion invites focus on associated mechanisms as a novel angle for mammalian study and potential intervention therapies in neurodegenerative disease.

Results

Electron microscopy suggests that intermediate filament-associated aggresomes are present in proteo-stressed *C. elegans* neurons in the early bud phase of exopher production.

The dynamic process of exopher-mediated expulsion involves collection and localization of noxious cellular contents, neuronal soma expansion, outward budding of a large membrane-surrounded vesicle that can preferentially concentrate specific cell contents, and the release of the loaded membrane-surrounded nascent exopher into the domain of the neighboring cell [4, 5] (New Figure 1A,B). We study exopher biology in a *C. elegans* strain in which the six easily visualized touch receptor neurons express an mCherry reporter at high levels; for

simplicity we refer to transgene *bzIs166*[$P_{mec\text{-}4}$mCherry] as mCherry in the text that follows. During early adult life, the ALMR touch receptor neuron (**A**nterior **L**ateral **M**icrotubule mechanosensory touch neuron, **R**ight side) can bud out a large, nearly soma-sized, vesicle to extrude most of the detectable mCherry fluorophore in one (or less frequently a few) large exopher(s) (example of a touch neuron exopher in Figure 1A, cartoon of budding out exopher production in Figure 1B) [4].

To gain insight into the intracellular events that accompany exopher formation, we examined ultrastructural features of ALM neuron somata from mCherry proteo-stressed touch receptor neurons, focusing primarily on neurons that we visually assessed to be beginning to bud out exophers (morphological stages of exophergenesis described in detail in reference [5]; see Figure 1B). We used high pressure freezing/freeze substitution (HPF/FS) and prepared electron microscopy serial sections from the group of visually selected “early bud” neuron mCherry adult day 2 (Ad2) animals. Electron micrographs generated from twelve distinct neurons revealed that the somata in mCherry-expressing neurons exhibit substantial swelling and contain multiple novel/altered structures.

We noted that the proteo-stressed ALM somas often contained one to two micron-sized rounded structures located close to neuronal nuclei (Supplementary Figure 1A-D). These round structures included a central granular matrix. A striking feature of the juxtanuclear structures was their peripheral-association with 10 nm-wide filaments (9.99 nm; > 150 filaments measured, +/- 0.80 SD), a diameter measure consistent with that

of Intermediate Filaments (IF). Electron tomograms confirm that these 10 nm filaments can be readily distinguished from membrane bilayers (Supplementary Videos 1, 2).

Data from the twelve neurons we examined suggest a potential “growth/maturation” sequence for the spherical structures. Some of these spherical granular structures contain a patched mesh-work-like border of single discontinuous filaments at the periphery, and a few disorganized short loose intermediate filaments inside (Supplementary Figure 1A, B). Some granular structures that may be more advanced featured a series of longer curved filaments assembled in parallel at the periphery, with each filament remaining separate from its neighbors, and fewer short filaments inside the structure (Supplementary Figure 1C). Finally, some rounded juxtanuclear structures display a periphery of loosely-parallel filaments, with some portions of the border having a densely packed layer of filaments; no internal filament structures evident (Supplementary Figure 1D). We also noted that the electron density of the central granular material appears higher in samples with greater filament association.

Although technical challenges precluded our immuno-EM verification of intermediate filament identification, these structures in mCherry ALM neurons are strikingly reminiscent of maturing mammalian aggresomes that form under high proteostress and are characterized by intermediate filament proteins that coalesce around sequestered aggregated protein [8, 13-15]. Given our observations, we hypothesized that aggresome associated intermediate filaments might be important in exopher production.

Intermediate filaments proteins IFD-1 and IFD-2 act in the same genetic process to promote efficient exopher production

Intermediate filaments (IF) are ~ 10 nm thick fibers typically, (but not always) formed of assemblies of conserved light and heavy chain IF proteins [16, 17]. IFs expressed in neurons (neurofilaments, NFs) influence neuronal structure and intracellular transport [18, 19]. Consistent with critical roles in neuronal function, IFs have been implicated in multiple neurodegenerative diseases and their sequelae [20]. For example, neurofilaments (NFs) can surround aggresomes in neurons that express toxic aggregating proteins [21] and NFs are major components of α-synuclein-containing Lewy bodies that characterize Parkinson's disease pathology [22]. The secretion of NFs in cerebrospinal fluid, and more recently, blood plasma, serves as a highly utilized indicator of neuronal injury and neurodegeneration in human clinical assessment [23]. The precise roles of NFs in neuropathology are not well understood, nor does much data address how NFs come to be secreted components present in CSF and blood plasma.

Given the prominent IF-like structures observed in the EM analysis of proteostressed touch neurons as they begin to produce exopher buds, we used genetic disruption approaches to test requirements for IF proteins in exophergenesis, beginning with: 1) an RNA interference (RNAi) feeding approach to knock down expression of each of the eleven *C. elegans* IF genes in a strain engineered such that all non-neuronal cells + touch receptor neurons were RNAi-amenable (Supplementary Figure 2A), and 2) RNAi knockdown of nine IF genes in a strain in which only neurons were RNAi amenable

(New Supplementary Figure 2B). We found that RNAi knockdown of multiple IF genes reduced exopher levels - the first implication of IF functions in large-vesicle extrusions from neurons in a physiological context. Given the relatively strong RNAi suppression effects for both members of the IFD subclass *ifd-1* and *ifd-2* in multiple backgrounds, the documented transcriptional expression of *ifd-1* [24] and *ifd-2* [24-26] in touch neurons, and the limited study of the biological roles of the *C. elegans* IFD genes to date [27-31], we pursued details of IFD family members *ifd-1* and *ifd-2* contributions to exophergenesis.

To confirm RNAi outcomes, we tested whether null alleles of *ifd-1* and *ifd-2* act as exopher suppressors. We obtained a mutant strain containing the *ifd-1(ok2404)* deletion and used CRISPR/Cas9 technology to generate a deletion allele of *ifd-2* named *bz187.* The *ifd-1(Δ)* and *ifd-2(Δ)* mutants exhibited normal or near normal developmental timing (*ifd-2(Δ)* ~5 hour average delay to L4) and longevity, WT morphology and brood size, WT osmotic stress survival, normal (*ifd-2(Δ))* or elevated oxidative stress sensitivity (for *ifd-1(Δ)*), and WT or modest suppression *(ifd-2(Δ))* of baseline *gst-4*::GFP expression (GST-4::GFP is a *daf-16*/FOXO/ SKN-1/NRF responsive glutathione-S-transferase reporter commonly used to report stress conditions [32]). In terms of touch neuron-specific features, we measured normal touch neuron function and touch neuron morphology during aging (New Supplementary Figures 4). Overall, *ifd-1* or *ifd-2* deletions do not confer substantial consistent systemic physiological disruption in the animal or in the touch neurons in which we characterize exophergenesis.

We crossed the *bzIs166*[$P_{mec\text{-}4}$mCherry] reporter into the *ifd-1(Δ) and ifd-2(Δ)* backgrounds and measured exophers at Ad2. We found that *ifd-1(Δ)* and *ifd-2Δ)* each suppress exopher production (Figure 1C), confirming RNAi observations and definitively establishing a role for *C. elegans* IFDs in promoting exopher formation. To confirm exopher suppression in a reporter background different from mCherry, we crossed *uIs31*[$P_{mec\text{-}17}$GFP] (a *mec-17* promoter-driven cytosolic-GFP transgene commonly used as a cytoplasmic touch neuron reporter), with *ifd-1(Δ) and ifd-2(Δ)* and measured exophers at Ad2. Both *ifd-1(Δ)* and *ifd-2(Δ)* deletions significantly suppress exophers visualized with the GFP marker (New Supplementary Figure 5). Thus *ifds* appear to act generally -- in multiple neuronal-tagging backgrounds, rather than by specifically enacting a response to elevated mCherry expression.

Despite the fact that null alleles of *ifd-1* and *ifd-2(Δ)* remove nearly all protein coding sequences, neither *ifd-1(Δ)* nor *ifd-2(Δ)* fully eliminated exophers, suggesting that *ifd-1* and *ifd-2* might function in redundant pathways that promote exopher formation. To address whether *ifd-1* and *ifd-2* might act in the same, or in parallel, pathways in exophergenesis, we constructed an *ifd-1(Δ)* and *ifd-2(Δ)* double mutant and compared exopher levels to those in single *ifd* mutants (Figure 1C). We found that exopher production in the *ifd-1(Δ)* and *ifd-2(Δ)* double mutant was suppressed to the same extent as in the single mutants, suggesting that *ifd-1* and *ifd-2* are likely to act in the same pathway to influence exopher production. Because some exopher production still occurs when *ifd-1* and *ifd-2* are both absent, we infer that a redundant activity or a parallel pathway must also contribute to exopher formation, with additional intermediate

filaments being candidates for participation in that process (New Supplementary Figure 2C).

Intermediate filaments proteins IFD-1 and IFD-2 act cell autonomously to promote exopher production

To gain insight into functions of IFD-1 and IFD-2 in exopher production, we expressed single-copy fluorescently-tagged reporters exclusively in the touch receptor neurons. We added GFP to the N-terminus of IFD-1 and mNeonGreen to the N-terminus of IFD-2, fused these reporters to the strong touch neuron promoter *mec-7*, and used miniMos technology [33] to introduce the transgenes in single copy; we also crossed mCherry into the background to enable soma and exopher tracking and potentiate exopher production.

To test function of the tagged-*ifd* constructs, we introduced the *bzSi3*[$P_{mec\text{-}7}$GFP::IFD-1] and *bzSi37*[$P_{mec\text{-}7}$mNeonGreen::IFD-2] transgenes into cognate *ifd* deletion backgrounds and assayed ALMR exopher production at Ad2. We found that single copy *bzSi3*[$P_{mec\text{-}7}$GFP::IFD-1] rescues the exopher deficit phenotype of the *ifd-1(Δ)* mutant (Figure 1D). Similarly, single copy *bzSi37*[$P_{mec\text{-}7}$mNeonGreen::IFD-2] rescues the exopher deficit phenotype of the *ifd-2(Δ)* mutant (Figure 1E). These results imply cell-autonomy for IFD activity in exophergenesis.

Because *ifd-2* is also expressed in the intestine [34] (New Supplementary Figure 8) and mutants can have intestinal morphology defects [30], we also tested for rescue of the

neuronal exopher phenotype in a single copy *bzSi45*[$P_{vha\text{-}6}$mNeonGreen::IFD-2]; mCherry line, in which mNeonGreen::IFD-2 is specifically expressed in the intestine. Intestinal expression of mNeonGreen::IFD-2 does not rescue the neuronal exopher phenotype of *ifd-2(Δ),* (New Supplementary Figure 9*)*—consistent with a driving role for *ifd-2* in exophergenesis that lies outside of the intestine*.*

In sum: 1) touch neuron-specific rescue of the exopher establishes that IFD-1 and IFD-2 act cell autonomously to influence exopher production, a conclusion consistent with neuron-specific RNAi outcomes (New Supplementary Figure 2); and 2) fluorescently tagged IFD-1 and IFD-2 proteins confer functional complementation of exophergenesis and are therefore likely to localize to, and indicate the identity of, their native subcellular compartments.

Additional details showing that high copy rescue by tagged *ifd-1* or *ifd-2* also can be accomplished without conferring dominant negative effects on exophergenesis or without driving high levels of exophergenesis; and some capacity for trans-complementation of *ifd-2* for *ifd-1* and *visa versa* are presented and discussed in New Supplementary Figure 6 and New Supplementary Figure 12.

IFD-1 and IFD-2 colocalize in juxtanuclear foci that are distinct from Golgi, lysosomes and mitochondria

Specialized cellular distribution can inform on protein function, and thus we studied the subcellular localization patterns of functional fluorescently tagged GFP::IFD-1 and mNeonGreen::IFD-2 proteins expressed in touch neurons from single copy transgenes. We found that in the mCherry background, GFP::IFD-1 and mNeonGreen::IFD-2 typically appear in one to three ~ 1 μm foci located near the nuclear membrane (Figure 2A-B, Supplementary Figure 10A-B, Supplementary Figure 11), with two IFD foci being most common during early adult life when exophergenesis is highest (Supplementary Figure 10A). The IFD foci increase in size from L4 to later adulthood (Figure 2C, Supplementary Figure 10B). GFP::IFD-1 foci assembly and overall size does not depend on *ifd-2* (New Supplementary Figure 7). Interestingly, the IFD foci appear akin in size and position to the IF-associated structures we observed in EM in the absence of expressed tagged IFD proteins (Supplementary Figure 1).

We found that similar concentrated juxtanuclear IFD foci can be visualized using multiple different fluorescent reporter-tagged versions of IFD-1 and IFD-2 (*i.e.,* for mNeonGreen, RFP, and mScarlet fluorescent tags **(**Supplementary Figure 11); indicating the subcellular localization pattern of IFDs is independent of fluorescent tag identity. Elevated expression of the tagged *ifd-1* or *ifd-2* reporters does not change subcellular localization or alter exopher levels (Supplementary Figure 12). Although we could not detect expression from native *ifd* promoters or native *ifd* promoter transgenes in touch neurons (New Supplementary Figure 8) (a reporter outcome we often observe for native promoter-single copy reporters in touch neurons including channel *mec-4*, dynein heavy chain *dhc-1*, and *rab-11, a*GTPase required for recycling endosome

function, for example [[35, 36], and our observations in TNs]; the functional complementation of the IFD reporters, lack of dominant negative effects of expressed *ifd* reporter transgenes, and consistent localization of different reporter fusion proteins to the same subcellular site support that IFD-1 and IFD-2 normally concentrate into distinctive juxtanuclear foci in proteo-stressed touch neurons.

To determine whether IFD-1 and IFD-2 colocalize with each other in the juxtanuclear foci, we tested for co-incidence in strains that expressed both GFP::IFD-1 and RFP::IFD-2 in touch neurons (Figure 2D). We find that GFP::IFD-1 and RFP::IFD-2 signals are nearly completely colocalized (quantitation in Figure 2H), consistent with genetic data that suggest that IFD-1 and IFD-2 influence exophers via the same pathway (Figure 1C).

To address whether the juxtanuclear IFD foci correspond to cell compartments that are distinct from other organelles, we tracked IFD-1 and IFD-2 localization relative to Golgi, lysosomes, and mitochondrial reporters. We found that tagged IFD proteins did not colocalize substantially with Golgi marker AMAN-2::tagBFP (Figure 2E, I), late endosome and lysosome marker LMP-1::mScarlet (Figure 2F, J), or mitochondria tagged with MitoROGFP (Figure 2G, K). Thus, our data support that the IFDs localize to a neuronal compartment distinct from Golgi, lysosomes, and mitochondria. We did note that IFD inclusions were often found next to Golgi or lysosomes, and thus the possibility that the IFD compartments might interact with these organelles, potentially via transient associations, should be entertained in future study.

IFD foci are highly homologous to mammalian aggresomes

Under high proteostress conditions, ubiquitinated and non-ubiquitinated aggregated proteins in mammalian (and other) cells can be linked to adapters such as HDA-6/HDAC6, SQST-1/p62, and the HSP-1/BAG3/14-3-3 complex that connect to dynein motors and move along microtubule tracks to juxtanuclear sites to deposit aggregate cargos [37], [38] [39]. IFs concentrate at these juxtanuclear sites, which are called aggresomes. Since our data reveal juxtanuclear concentration for IFDs and implicate IFDs in the proteostress response of exophergenesis, we tested the hypothesis that IFD foci are *C. elegans* aggresome counterparts by manipulating facets of aggresome biogenesis and probing for colocalization of IFDs and aggresome proteins reported in the mammalian literature.

To test microtubule (MT) requirements for juxtanuclear IFD concentration, we treated $P_{mec\text{-}7}$GFP::IFD-1 expressing animals with the potent microtubule inhibitor colchicine [40, 41] from L4 to Ad2 (Figure 3B-C, Supplementary Figure 13A-B). We find that colchicine disrupts the juxtanuclear concentration and increases the number of dispersed GFP::IFD-1 foci, suggesting a requirement for MTs in the juxtanuclear localization of the *C. elegans* IFD compartment, as occurs for mammalian aggresomes.

Colchicine treatment acts systemically and could act via non-autonomous influences, and thus we also used the auxin-inducible degradation system ([36]) to degrade dynein

heavy chain component DHC-1 specifically in touch neurons. We introduced a degron-tagged *dhc-1* allele into a strain engineered for touch neuron-specific expression of the ubiquitin ligase adapter TIR1, which promotes rapid degradation of degron-linked sequences when auxin is added to the culture. We treated animals with auxin from L4 to Ad2 to enable auxin-promoted degradation of DHC-1::degron and scored GFP::IFD-1 inclusions. We found that in the presence of auxin (and therefore when DHC-1::degron was degraded), IFD inclusions were small, mobile, dispersed, and more numerous than controls (Figure 3D-E, Supplementary Figure 13C-D). We conclude that a touch neuron-expressed DHC-1-containing dynein motor acts cell autonomously in IFD collection and concentration into large juxtanuclear inclusions, similar to dynein motor roles in mammalian aggresome formation.

We also tested for molecular associations of IFDs with homologs of aggregate adapter proteins documented to contribute to, and associate with, mammalian aggresomes. Mammalian aggregate collection and delivery to aggresomes occurs via at least three distinct molecular adapters that link aggregates to dynein motors for MT transport to juxtanuclear IF-rich inclusions [8, 39, 42, 43]: SQSTM1/p62 autophagy/adapter, HDAC6 deacetylase, and 14-3-3 protein, the latter of which functions in an adapter complex that includes BAG3 and chaperone Hsc70 [43] (Figure 3A). We constructed strains harboring GFP::IFD-1 and tagged *C. elegans* homologs of *sqst-1/*SQSTM1, *hsp-1*/HSP1 and *ftt-2/*14-3-3. For each adapter tested, we find colocalization with the juxtanuclear GFP::IFD-1 protein, akin to their characterized mammalian counterparts (Supplementary Figure 17G, Figure 3F-G).

Mammalian aggresomes can collect ubiquitinated proteins [8, 44, 45] and therefore we also asked whether IFD inclusions colocalize with sites of ubiquitin concentration. We co-expressed single copy transgene mNeonGreen::UBQ-2 in touch neurons together with mScarlet::IFD-1 (Figure 4A) or mScarlet::IFD-2 (Figure 4B) and found that although some fluorescently tagged ubiquitin can be dispersed or concentrated elsewhere in the neuronal soma as expected, mNG-tagged ubiquitin also concentrates in the IFD-1 and IFD-2 inclusions. We conclude that, like mammalian aggresomes, the *C. elegans* neuronal juxtanuclear IFD inclusions are associated with concentrated ubiquitinated proteins.

Although details of cargo collection, specific dynein/dynactin components involved, and microtubule biology remain to be elaborated, it is striking that IFD foci concentration and co-localizations we examined to date closely mirror involvement of homologs of proteins involved in mammalian aggresome formation. We conclude that *C. elegans* IFD proteins localize to a juxtanuclear aggresome compartment. Since most reports mentioning *C. elegans* aggregated proteins as aggresomes to date have not included colocalization studies that confirm aggresome identity, our data both establish that stressed *C. elegans* neurons can form structures homologous to mammalian aggresomes and support that aggresome biology is likely to be conserved.

C. elegans **aggresomes can include neurotoxic polyQ disease aggregates**

Ubiquitin colocalization is suggestive of concentrated misfolded/aggregated proteins (Figure 4A-B). To address whether a characterized toxic aggregating human neurodegenerative disease protein can concentrate in the IFD-aggresome inclusions, we focused on polyglutamine expansion proteins, which have been found to aggregate and stress *C. elegans* neurons [46, 47]. We constructed and co-expressed a single copy transgene encoding mNG::HttQ74, which includes much of the first exon of the human Huntingtin gene fused to a HttQ74 expansion [48], together with mScarlet::IFD-1 or mScarlet::IFD-2 reporters. We identified strong localization of mNG::HttQ74 to IFD-1 and IFD-2 inclusions in the touch neuron soma (Figure 4C-D) when mNG::HttQ74 is expressed at levels at which visible aggregation is present. We also examined a published HttQ128::CFP line expressed from an integrated high-copy-number array along with mScarlet::IFD-1 and observed coincident fluorescence (Figure 4E). Our data establish that expanded polyglutamine proteins can concentrate at IFD inclusions, consistent with the idea that IFDs mark and sequester a domain of aggregated protein, and similar to what has been reported for mammalian aggresomes.

Interestingly, we noted that association of IFDs and HttQ128::CFP can adopt multiple relative configurations, being mostly coincident for smaller presumptively newly formed aggresomes (Figure 4) but more frequently exhibiting less complete “covering” with advancing time or when relative expression of HttQ128::CFP and IFDs is unbalanced (Figure 4, Supplementary Figure 14). Dynamic patterns of polyQ concentrations and maturation have been reported *in vivo* in *C. elegans* [49]) and in HEK cells [50]; our data further support a dynamic interaction of IFDs and aggregates, and challenge the

concept that aggresomes are static structures in which IFs fully “cage” sequestered materials (see Discussion).

We also characterized the localization of highly expressed touch-neuron mCherry, relative to IFD foci. Overexpressed mCherry *bzIs166[*$P_{mec\text{-}4}$mCherry] marks touch neurons and exophers and increases proteostress to elevate baseline exopher numbers; mCherry can concentrate into particular subcellular foci [4], [5]. There are likely multiple pools of mCherry in the cell, complicating using its localization in analyzing aggresomes. We found dimmer mCherry concentrations colocalized with IFD-1 in a few ALM neurons, but most highly concentrated mCherry in touch neuron somata was within LMP-1::GFP positive lysosomes (Supplementary Figure 16B) (LMP-1 is the lysosomal membrane protein LAMP1 ortholog [51]), as also occurs in mammalian cells [52]). Thus, although mCherry is a powerful reporter of whether an exopher has been produced [4], [5], [11], and exophers are filled with heterogenous cargo [4], the mCherry trajectory does not strictly align with that of the IFD aggresome.

In summary, colocalization analyses indicate that cargoes of different character (*i.e.*, expanded poly-Q proteins and mCherry) are differentially handled, concentrated, and/or stored prior to expulsion within exophers, and that the expanded poly-Q proteins associate with, and linger within, IFD inclusions (Figure 4C-D, Supplementary Figure 14, Supplementary Figure 15). We speculate on the nature of cargo dichotomy and its implications for exophergenesis in the Discussion.

IFD-positive foci can be expelled within exophers, but not all exophers contain IFD-1 positive foci.

A critical question in deciphering the roles of IFDs in exophergenesis is whether the IFD inclusions are themselves expelled from the soma within exophers. We examined exophers in a strain that co-expressed mSc::IFD-1 and mNG::HttQ74 after 6 hours of food withdrawal, a culture condition that increases exopher production [11]. Focusing first on the simplest question of whether IFD-1 can be extruded into exophers, we found that out of 30 total exopher events we scored, 14 included detectable mSc::IFD-1 (Supplementary Figure 16A, top) establishing that tagged intermediate filament mSc::IFD-1 can be extruded in exophers. Since mSc::IFD-1 is present only in about half of the exophers we imaged, we infer that substantial IFD-1 extrusion is unlikely to be a mechanistic requirement in all exophergenesis.

Ejected IFD foci colocalize with mNG::HttQ74 in most extrusion events

To assess the IFD-1 status relative to ejected cargo, we looked at the mNG::HttQ74 overlap with the mSc::IFD-1 that were ejected in exophers (i.e., in exophers that included mSc::IFD-1 puncta/ae). Of the 14 mSc::IFD-1-positive exophers we reported in Supplementary Figure 16A bottom, 11 exophers contained species in which mSc::IFD-1 and mNG::HttQ74 colocalized to the same puncta; only 3 exopher events had mSc::IFD-1 foci in exophers(s) that lacked co-enrichment of mNG::HttQ74 (Supplementary Figure 16A). We conclude that IFD-1-aggresomes hosting HttQ74-cargo are often components of extruded exophers in this test strain.

In a complementary study focused on cases in which HttQ74 aggregates leave the cell, we looked at the same 30 exopher events with an initial emphasis on the mNG::HttQ74 reporter. We found that 22 of the 30 exophers contained at least one identifiable mNG::HttQ74-enriched punctum (Supplementary Figure 16B top). Of those 22 exopher events that included mNG::HttQ74 punctae, we asked whether the ejected HttQ74 was accompanied by IFD-1. We find 11 out of 22 exophers also displayed mSc::IFD-1 colocalized with mNG::HttQ74 (Supplementary Figure 16B bottom). Data indicate that HttQ74-aggregates are often extruded into exophers as an IFD-1+ aggresomes, although HttQ74 can leave the soma in the exopher compartment nearly as frequently without co-IFD-1 association; IFD-1 association does not appear strictly required for HttQ74 extrusion.

Adapter proteins have a role in both aggresome formation and exopher ejection

We reasoned that if IFDs engage aggresome biology to influence exopher production; disruption of adapters that influence aggresome loading might also modulate exophergenesis.

We examined available viable mutants for *C. elegans* counterparts of three aggregate collection pathways: *hda-6*/HDAC6, *sqst-1/*SQSTM1, and *ftt-2*/14-3-3. We scored aggresome dimensions as reported by GFP::IFD-1 and exopher levels using mCherry to visualize touch neurons and exophers (Supplementary Figure 17A-F, Figure 5A-C).

We find that no individual adapter disruption eliminates the IFD compartment. Thus, in physiological context in *C. elegans*, no single aggregate collection pathway is essential, and multiple routes likely function in parallel for aggresome filling, consistent with reported mammalian biology [43, 53]).

We did quantitate some significant change in aggresome dimensions in the adapter mutant backgrounds (Supplementary Figure 17A-B, D-E, Figure 5A-B). ALM touch neurons in the *sqst-1(ok2892)* have significantly smaller GFP::IFD-1 puncta, with increased puncta numbers (Supplementary Figure 17D-E); *ftt-2(n4426)* ALMs have significantly smaller GFP::IFD-1 aggresomes without a change in number of aggresomal sites per cell (Figure 5A-B). Aggresome features suggest roles for SQST-1 and FTT-2 in GFP::IFD-1 aggresome growth.

Regarding exopher production, we note that *sqst-1(ok2892)* increases variation in exopher levels, but overall note there is no significant change in exopher number compared to WT in the *sqst-1* mutant (New Supplementary Figure 17F). Variation might be attributed to the roles SQST-1 plays in both aggresome formation and autophagy (autophagy disruption usually increases exopher levels as reported[4], and in New Supplementary Figure 10E-F). *hda-6(ok3204)* (which did not significantly impact GFP::IFD-1 formation) increased exopher levels (New Supplementary Figure 17A-C). Although deciphering the reason for exopher elevation in the *hda-6* mutant will require further experimentation, mammalian HDAC6 modulates tubulin cytoskeleton as well as aggresome loading so outcome might reflect dual activities.

The 14-3-3 mutant *ftt-2(n4426),* which induced a significant reduction in aggresome size (Figure 5A-B), had a clear exopher suppressor phenotype (New Figure 5C). In addition, we used both a neuron sensitized and neuron-specific RNAi approach and confirmed FTT-2's role in exophergenesis (New Figure 5 F, H) in a cell autonomous manner.

We also sought to test another component of the FTT-2/14-3-3 adapter cormplex, *hsp-1/Hsc70* [37]. RNAi against *hsp-1* similarly reduced exophers in an RNAi strain engineered to enhance knockdown in *mec-18* touch neurons via expression of SID-1 RNAi transporter (New Figure 5E) (and trended to suppress exopher production in a strain targeting specifically neurons (i.e. *sid-1* mutant background with transgenic pan-neuronal expression of *sid-1*) (P = 0.221, 78% confidence). Note that trending but non-significant data could reflect HSP-1s multiple roles or RNAi gene targeting efficacy.

Results support that 1) the FTT-2 aggresome-related binding partner, HSP-1, plays a role in exophergenesis, and 2) results further support dual role of the HSP-1/FTT-2 adapter complex in both aggresome formation and exophergenesis.

Complementary to results suggesting cell-autonomous exopher related function of FTT-2 (New Figure 5F-G), adding an extra single copy of *ftt-2* expressed from the *mec-7* promoter in touch neurons ($P_{mec\text{-}7}$ FTT-2::mSc; $P_{mec\text{-}4}$ mCherry), significantly elevated exophers indicating cell autonomous activity in exopher increase (New Figure 5H). [54]

Overall, we conclude that both adapter biology and IF biology can influence exophergenesis in a cell autonomous mechanism. Our data suggest that the HSP-1/Hsc70/FTT-2/14-3-3 collection might be particularly influential in aggresome formation and exophergenesis. Data both support a conserved mechanism of aggresome formation from nematode to human and establish a role for the aggresome organelle in exopher levels. Our findings raise the possibility that aggresome structures play critical roles in influencing mammalian aggregate extrusions.

Human neuronal intermediate filament protein hNFL can complement *C. elegans ifd-2* deletion to promote exopher formation, suggesting conserved function in neuronal extrusion

Mammalian intermediate filament proteins are integrated into the neuronal proteostasis network and can associate with juxtanuclear aggresomes [8, 21, 55, 56]. Roles for mammalian IFs in neuronal aggregate extrusion have not been reported, but our *C. elegans* observations raise the possibility that higher organism neuronal IFs might act in exopher-related biology [57] [58, 59]. To begin to address this possibility, we asked if a human neuronally-expressed intermediate filament protein can complement an *ifd(Δ)* for exopher production deficits.

We focused on testing human neurofilament light chain (hNFL) because hNFL is a mammalian neuron-specific intermediate filament protein and hNFL exhibits ~24/45% sequence identity/similarity to *C. elegans ifd-1* and *ifd-2* (for comparison, human Bcl2 and *C. elegans ced-9,* homologs demonstrated to complement for apoptosis regulation

across species[60] score as 24/43% identity/similarity). Moreover, human hNFL is clinically evaluated as a circulating blood/CSF biomarker of neuronal injury and neurodegenerative disease [61] [62] despite mysteries surrounding its origins in circulation.

We optimized the human hNFL gene for expression in *C. elegans* based on codon bias and inclusion of short introns using *C. elegans* Codon Adapter Software [63]. We first documented the subcellular distribution of the tagged mNG::hNFL expressed under the direction of a *mec-7* promoter from a single copy insertion in touch neurons (Supplementary Figure 18). mNG::hNFL concentrated to juxtanuclear foci that colocalize with *C. elegans* intermediate filament reporter mSc::IFD-1 (Figure 6A). mScarlet::hNFL colocalizes with ubiquitin mNG::UBQ-2 (Figure 6B), and with mNG::HttQ74 (Figure 6C) in aggresome compartments. Although the predominant localization of mNG::hNFL is to one or two punctate juxtanuclear locations (Supplementary Figure 18D, quantified in New Supplementary Figure 18F-K with both single copy and high copy mNG::hNFL reporters, we did note that FP-tagged hNFL could also be distributed more broadly in the neuron as compared to FP::IFDs, also appearing in the axon, nucleus, and in filamentous patterns in the cytoplasm in some neurons (Supplementary Figure 18A-C). Nonetheless, *C. elegans* IFDs and hNFL clearly localize similarly to aggresome compartments.

Having documented distribution of human hNFL that reflects that of *C. elegans* IFDs at aggresomes, we introduced the $P_{mec\text{-}7}$mNG::hNFL single copy transgene into an *ifd-2(Δ);* mCherry background and compared exopher production in *ifd-2(Δ)* vs. *ifd-2(Δ)*;

$P_{mec\text{-}7}$mNG::hNFL. Single copy $P_{mec\text{-}7}$mNG::hNFL can rescue *ifd-2(Δ)* exopher deficits (P=0.0046; new Figure 6E). mNG::hNFL single or overexpressed constructs, similarly to tagged IFD constructs, do not elevate nor suppress exopher levels on their own, indicating that the rescuing activity is not caused by transgenic protein aggregation (New Supplementary Figure 19A-B). hNFL rescue of *ifd-2(Δ)* exopher deficits reveals that human neuronal intermediate filament protein hNFL can serve a conserved role in exopher biology and suggests a novel potential cellular activity for hNFL in extrusion of human neuronal materials.

Can hNFL itself be extruded via an exopher-like mechanism? Akin to what we documented for the *C. elegans* IFD-aggresome (Supplementary Figure 16A-B), we found that hNFL inclusions is be expelled within about half of *C. elegans* exophers (Figure 6D). We suggest that an exopher-like mechanism might mediate extrusion of the hNFL biomarker in human disease.

In sum, our finding that human hNFL compensates for *ifd-2* function (New Figure 6E), shows overlapping subcellular localization with *C. elegans* IFD and aggresome components (Figure 6A-C), and is expelled from the soma in exophers (Figure 6D), raises the possibility that mammalian IFs may play roles in cellular extrusion that are conserved from nematodes to humans, inviting the re-examination of mammalian aggresome biology in the context of mechanisms of human aggregate spread.

Discussion

Overview and Significance. The fundamental mechanisms by which proteo-stressed neurons deal with toxic aggregates remains a central question in neurodegenerative disease [2]. In mammals, processes strikingly similar to *C. elegans* exophergenesis have recently been described for extrusions from mouse cardiomyocytes, [57, 64], HeLa cells [65], and retinal ganglion cells [66], highlighting a novel aggregate management strategy for offloading toxic aggregates and organelles that may operate in cells across phyla [66]. Although molecular links among the associated extrusion events remain to be rigorously established, initial observations support the hypothesis that exopher-like responses are within the capacity of a variety of stressed cells in a range of tissues (See Review on Heterophagy: [67]).

Here we took initial steps toward deciphering cell autonomous mechanisms by which *C. elegans* neurons transfer neurotoxic contents out of the cell in large exopher extrusions, finding that specific intermediate filament proteins IFD-1 and IFD-2 are required within the stressed neuron for efficient exophergenesis. At the cell biological level, intermediate filament proteins IFD-1 and IFD-2 concentrate into stress-responsive juxtanuclear puncta that are strikingly analogous in position and composition to what has been reported for mammalian aggresomes; additional cargo adapter/aggresome component 14-3-3/FTT-2 and binding partner HSP-1/Hsc70, are also needed for efficient exophergenesis. The conserved nature of the associated biology is supported

by our finding that expression of human neuronal intermediate filament protein hNFL in *C. elegans* neurons can functionally substitute for *C. elegans ifd-2* in exopher production.

Stressed *C. elegans* neurons produce aggresomes via conserved mechanisms. The original description of mammalian aggresomes (focused in CHO and HEK cultured cells) defined multiple aggresome features, including prominent juxtanuclear concentration of aggregates with distinct localization from Golgi and lysosomes, association with intermediate filaments under proteostress conditions (aggregate-prone protein over-expression or inhibition of the proteasome; ubiquitinated and heterogeneous cargoes included), and requirement for microtubule and dynein motor integrity for biogenesis [8]. Follow up studies established that p62/SQST1, HDAC6, and 14-3-3 BAG3 HSP1 complex associate with small foci that move into the large perinuclear aggresome [37, 68]. We find that most of these mammalian aggresome features are in common with the IFD-associated puncta in proteo-stressed *C. elegans* touch neurons, including collection of aggregated polyQ protein, enrichment in folding chaperones, ubiquitin, and dynein motor adapters, and a requirement for intact microtubules and dynein activity to collect such materials into one or two juxtanuclear sites. Furthermore, we report a requirement for FTT-2/14-3-3 adapter (and possibly HSP-1/Hsc70 chaperone) in exophergenesis, additional evidence suggesting aggresome formation is linked to exopher production levels.

Aggresome appearance associated with the expression of human neurodegenerative disease proteins [69, 70] or ROS stresses [71] have been reported for *C. elegans* cells, but the data we present contributes the first multi-component characterization of *C. elegans* neuronal aggresomes and definitively establishes that aggresome formation mechanisms are conserved from nematodes to humans. *C. elegans* are thus a legitimate model for deciphering the relative role of aggresomes in maintaining neuronal proteostasis in an *in vivo* context.

Aggresome-related mechanisms influence exopher levels. Our data implicate aggresome-associated proteins that collect and associate with protein aggregates in promoting exophergenesis levels. Although it is possible that FTT-2/14-3-3 and IFDs act in additional cellular processes, the implication of multiple aggregate collection factors (FTT-2/14-3-3, HSP-1/HSP1, IFD-1/IF, and IFD-2/IF and hNFL) localized to the same compartment with shared functional capacity to modulate exopher extrusion levels links aggresome biology to extrusion.

Outcomes of our studies make a few points with regard to aggresome/exopher connection. First, IFs can be co-extruded with offensive proteins such as polyQ aggregates. However, since co-extrusion of IF and aggregates occurs in many but not all cases, IFDs are not essential structural components of all aggregate cargos in exophers. Although it is possible that the IFD domain might quickly dissociate and degrade once inside the exopher compartment, or that distinct or redundant IF types not tracked in our study might function for some cargo types, it seems most likely that a main function for IFD with

respect to aggregate collection/concentration transpires in the soma, rather than solely in the exopher compartment.

Second, over-expression of IFDs does not have capacity to elevate exopher levels. Thus, if IFD compartments drive exophergenesis, they likely require additional components for efficacy. That *ftt-2* over-expression can enhance exopher production suggests that a particular cargo type or level might factor into the neuronal decision to produce an exopher. Third, although the challenge of defining the precise cellular conditions that trigger the formation of an exopher remains, we have speculated that a simple increase in misfolded protein would increase exopher production; the observed decrease in exopher production upon depletion of protein folding chaperone HSP-1/Hsc70 supports that more than sensing of folding levels is needed to drive exophergenesis.

The contents of *C. elegans* exophers are highly heterogeneous and can include multiple protein cargos and a range of organelles [4] [72] yet exophers often appear to distinctly concentrate particular reporters. Some of this distribution may be accomplished by collection of specific targets into aggresome-like compartments via multiple pathways, at least one of which is the 14-3-3/HSP-1 route. HDA-6 can influence exopher levels, but potential roles in tubulin modulation vs. aggregate collection [73] remain to be teased apart in future work.

Our data do suggest a potential alternative mechanism for clearing aggresomes in mammals, which might have been missed in cell culture studies, but is highly relevant to the question of how pathological aggregates may spread in neurodegenerative disease. We suggest that aggresomes might serve a staging role for specific types of neuron-threatening contents, with the overall level of proteo-stress influencing the decision for extrusion.

Aggresome development in a whole animal context. Ultrastructural analysis of the early bud stage of exophergenesis suggests the assembly of a juxtanuclear domain surrounded by intermediate filament-sized proteins that may progressively mature to feature more surrounding IFs are mesh-like, rather than tight cages in nature (Supplementary Figure 1). The literature on aggresome growth and assembly details is limited, and it has been suggested that in HEK cell aggresome biogenesis, factors are involved in early seeding of an aggresome, but major expansion occurs by diffusion [74]. Detailed mechanisms of aggresome development and maturation should be genetically and cell biologically tractable in physiological context in the *C. elegans* model, with findings coupled to assays of exophergenesis to expand on deciphering the molecular relationship of aggresomes, aggregate load, and aggregate extrusion.

Aggregates, intermediate filaments, and extrusion. How aggregates interface with IFs at the aggresome compartment, and the function of intermediate filaments associated with these compartments, is not well understood. The mature IF meshwork could act as a proteostasis-linked signaling scaffold around aggresomes, promoting

proteostress pathway activation, including an exophergenesis response, or alternatively, the meshwork might act as a brake on such signaling if offensive material is fully encapsulated.

We noticed that under single copy expression of tagged IFD and HttpolyQ74 reporters, extensive co-localization of IFD and aggregate is common; but when HttpolyQ128 is highly expressed from multi-copy transgenes, IFDs do not fully envelop HttQ128 (Supplementary Figure 14). In mammals, some IFs “uncoat” from aggresomes prior to lysosome engagement for internal content degradation in a mechanism that involves subunits released from over-stressed proteosomes [75, 76]. Partial coverage, or “uncoating”, induced under high proteostress might engage an exophergenesis trigger. Another consideration is that mammalian IF vimentin can function to bring proteasomes to the aggresome to promote protein turnover at that site [77]. Were *C. elegans ifd-1* and *ifd-2* IFs needed for such activity, their disruption would limit aggresome resolution, possibly restricting dissociation required to activate extrusion. Beyond a signaling role, the IF meshwork could promote movement of aggresomes into the exopher bud, but testing this is difficult given the low rate of exopher formation when IFs are missing.

Implications of IF roles in exophergenesis for human biology. CSF and blood presence of neurofilament light protein (hNFL) are measured in the clinic as biomarkers for neuronal disease and injury [78-80]. Exactly how hNFL is released into human fluid spaces is not well documented. We found that IFD-1 and IFD-2, sharing 24% identity and 45% similarity with mammalian neuronal intermediate filament NFL, can be expelled within exophers in a significant fraction of exopher events.

Interestingly, a major protein component of extruded cardiomyocytes (a likely mammalian exopher variant [57, 58] were intermediate filaments; so there is a hint that mammalian cells can extrude intermediate filament aggresomes via an exopher-related mechanism.

Our findings in *C. elegans* reveal a novel way in which IFs are released from proteo-stressed neurons and raise the possibility that the commonly used biomarker of human neuronal injury and disease might also reflect active neuronal exopher expulsion mechanisms, an option not generally considered.

Exopher-like mechanisms involving IFs might influence a range of disease processes. Heritable mutations in neurofilaments can cause several neurological diseases including Giant Axonal Neuropathy, Charcot-Marie-Tooth (CMT) disease, Amyotrophic Lateral Sclerosis (ALS), and Parkinson's disease (PD) [81, 82]. The molecular mechanisms underlying these diseases remain unclear. Our data introduce the possibility that deficits in neuronal trash expulsion under stress conditions might be unexpected contributors to disease pathology.

Neurofilaments have also been widely implicated in a number of neurodegenerative diseases due to their concentrated presence within characteristic pathological inclusions [78, 80]. Pathological neurofilament accumulations are features in Parkinson’s disease (with α-synuclein), in Alzheimer's disease (with Aβ and tau), in polyglutamine CAG trinucleotide repeat disorders, and in ALS. For example, the likely relationship between

aggresomes and the Lewy body inclusions diagnostic for Parkinson's disease have been noted [83]. We document a novel functional role for IFDs and human NFL—we provide the first definitive demonstration that the specific IF proteins, that intimately associate with aggresomes and their neurotoxic cargo, actually regulate exopher formation and thus ejection of neurotoxic cargo and IFs themselves from neurons. Research into IFD or NFL management and ejection requirements in *C. elegans* may help explain basic mechanisms promoting aggresome- and -Lewy body like inclusion pathology that results in disease, while also providing the molecular understanding to clinical assays used currently to assess pathology.

Additional information: Supplementary information is available for this paper.

Acknowledgements. We thank past and present members of the Exopher Club for exopher-related discussions, and members of M.D. and B.D.G. laboratories at Rutgers University. We thank H. Ushakov for injection of some genetic lines.

Research was supported by the National Institutes of Health under award numbers R37AG56510, R01AG047101, and 1F31AG066405-01A1. K.N. and D.H.H. were supported by NIH OD010943. We thank Florian Geissler/Rudolf E Leube for providing plasmid DNA templates for IFD promoter amplification [34]. We thank Malene Hansen for RNAi allele(s) and RNAi related discussions. Some strains were provided by the CGC (which is funded by NIH Office of Research Infrastructure Programs (P40 OD010440) and the OK *C. elegans* Deletion Mutant Consortium. The content is solely the responsibility of all authors and does not necessarily represent the official views of the National Institutes of Health.

Author Contributions M.L.A., J.F.C., R.A., S.A., I.M., A.J.S., and R.J.G., conducted and designed experiments, along with M.D., M.L.A., and B.D.G, who wrote the manuscript with input from J.F.C., R.A., and R.J.G.. G.B. provided some plasmid constructions. K.C.N. and D.H.H. carried out electron microscopy fixation, interpretation, and analysis.

Competing interests statement: The authors declare that they have no competing financial interests.

Data Availability: Correspondence and requests for materials should be addressed to Barth D. Grant via email (grant@dls.rutgers.edu).

Reprints and permissions information is available at www.nature.com/reprints.

Methods

Strains and media. We cultured *C. elegans* strains at 20°C with standard methods as described [5]. We fed animals fed *Escherichia coli* OP50 unless we initiated RNAi or a 6-hour fasting protocols to induce proteostress-exophers. Extrachromosomal arrays were harbored on antibiotic selection plates (Hygromycin B or G418); for exopher measurements, animals were removed from selection plates and placed onto standard OP50 plates after L4 identification.

Strains. Transgenic alleles are noted in figure legends and in the strain list, Table 1. Animals expressing *igIs*1[$P_{mec\text{-}7}$YFP $P_{mec\text{-}3}$HttQ128::CFP] must be manually selected for CFP expression to prevent silencing of the CFP that we have not been able to easily reverse (high copy number silencing has been documented[84, 85]). PolyQ constructs are quite challenging to generate due to the extent of repeat sequences therein; still in an attempt to make and study a more co-operative polyQ in touch neurons, we constructed a single copy *bzSi39*[$P_{mec\text{-}7}$mNG::HttQ74] allele. The artificial polyQ protein aggregates minimally.

See **Table 1** for strain list.

Plasmid constructions. New allele information is described in **Table 2.** We created single-copy integration using MiniMOS technology using pCFJ1662 hygromycin or pCFJ910 G418-resistance conferring backbones [33]. For extra-chromosomal array transgenesis and selection we used hygromycin or G418 selection by exposing animals to selection plates. To make selection plates, we used 5mg/mL for hygromycin or 32mg/mL for G418 and add 200ul per 6cm OP50-seeded plate. We rear animals harboring extrachromosomal arrays on selection plates.

Human homolog optimization and expression. Both IFD-1 and IFD-2 are most closely related to the named mammalian (taxid : 9606) neurofilament light polypeptide (NP_006149.2) with e-values of 2e-15 and 3e-13 for IFD-1 and IFD-2 respectively, sharing 24% identity. To optimize human genes for *C. elegans* expression based on codon and intron bias and *C. elegans* amino acid to tRNA ratio, we used *C. elegans* Codon Adapter GGA Software [63]. Nucleotide coding regions of mammalian proteins

are provided. NCBI Reference Sequence: NM_006158.5 for *homo sapiens* neurofilament light.

CRISPR-CAS9 genomic *ifd-2* deletion. *ifd-2(bz187)* is a deletion of base pairs 815271-816275. 1004 base pairs, including the start codon. The first 3 exons are affected by the genomic deletion.

crRNA guide 5' GCCGTGTCCACTCTGAAATTTCGCG 3'
Repair oligo: 5' ccgcctccttatcacttatcacgcaggctagctCtcgaatggcaatgtcgtgttgtgaaatgcacccg '

RNAi. We achieved gene inactivation by feeding animals RNAi bacteria from L4-Ad2 or for 2 generations as noted, with RNAi-expressing bacteria, Htt115 with standard methods. We performed RNAi experiments in strains in which neurons are RNAi-enhanced via SID-1 expression [4, 5].

Age synchronization. To synchronize animals, we selected L4 stage hermaphrodites and moved them to test plates. The day after moving was considered adult day 1, ad1. We scored animals on adult day 2 (Ad2) unless otherwise noted. For scoring exophers, we measured animals on plates using a Krammer pseudo-stereo dissecting scope using 20x objective and immobilized using 100ul of 10mM tetramisole; exophers were also visible in live animals without anesthetic. We scored ALMR neurons for exopher events in a binary (yes/no) manner.

Exopher features for scoring. Exophers are readily visible at 400X total magnification with high power dissecting microscopes. Exopher characterization methods performed as described [5].

Microscopy. Most fluorescence micrograph data were captured on Zeiss Axiovert Z1 microscope equipped with X-Light V2 Spinning Disk Confocal Unit (CrestOptics), 7-line LDI Laser Launch (89 North), Photometrics Prime 95B Scientific CMOS camera, using Metamorph 7.7 software. A 100x oil immersion objective, 63x oil immersion, or 40x objective was used.

Fluorescent colocalization analysis. We imaged mechanosensory touch neurons for colocalization experiments. Where needed, we used DIC confirmation to identify touch neurons of interest. We analyzed neurons expressing both fluorophores. For mNG::HttQ74 and HttQ128::CFP colocalization, we used only neurons in which visible mNG-aggregation was observable in the cell (as opposed to dim cytosolic mNG signal) for colocalization calculations. We analyzed thresholded multi-color image channels using ImageJ FIJI with Coloc2 analysis software to calculate Pearson's and Mander's overlap coefficients. We used Pearson's coefficient to quantitate colocalization of organelle tags. Mander's overlap of thresholded double-channel images were calculated by using the channel used to tag IFD over the channel of the other protein tag. We manually analyzed images in each 0.2 - 0.25 um Z-stack for colocalization often observing Z-stacks laterally in 3D projection for 3-dimensional observation.

Soma GFP::IFD-1 focus measurement. We imaged whole touch neurons using 0.1 - 0.2 um z-stacks. We measured the largest diameter of each inclusion by calculating the longest pixel length using ImageJ software. We omitted neurons with the presence of an exopher(s) from GFP::IFD-1 size calculations. We calculated the number of IFD inclusions using a standard threshold.

Drug assays. For proteostasis drug treatments, we dissolved MG132 (Sigma-Aldrich C2211) and Spautin-1 (Sigma-Aldrich SML0440) in DMSO at 10mM concentration and administered by placing 40µL of each solution over the bacterial food lawn. We exposed animals to drug-plates from L4-Ad3. For DHC-1::degron AID-system treatments, we dissolved auxin in ethanol to 0.4M. We added 25µL 0.4M auxin and 175µl distilled water. We pipet 200µl solution, per plate, on top of well-seeded OP50 plates. We exposed both control and experimental animals to auxin plates from L4-Ad2 - only the experimental animals harbored *bzSi6*[$P_{mec\text{-}7}$TIR-1::TagBFP] necessary for auxin-inducible degradation[36].

Osmotic stress. We determined sensitivity to acute osmotic stress by moving L4 stage animals to NGM plates containing 450 mM concentrations of NaCl and scored exophers after an overnight exposure. Animals were scored for exophers using ringed cytology slides on a fluorescent Kramer dissecting microscope.

Oxidative stress experiments. We determined exopher sensitivity of animals to acute oxidative stress using, paraquat (methyl viologen, Sigma). We transferred L4 animals to freshly prepared NGM plates containing paraquat 200 mM and assessed percent survival after an overnight exposure.

Development assay. Post-embryonic development (PED) time was measured by transferring eggs to an NGM plate. We performed a 50-gravid animal egg lay lasting one hour upon a new NGM plate; egg laying adults were removed. After 60 hours from the egg lay, the plates were checked every hour and the percentage of progeny to develop was assessed. Young adults were counted and removed. The time from hatching to the L4-adult transition was measured the time to development. For significance tests we use a standard two-tailed t-test comparing the mean value of three trials.

Fertility. Brood size was measured by placing individual worms at the L4 stage onto NGM plates. We transferred animals to new plates daily for three days. The resulting progeny was allowed to develop to adulthood before paralysis and quantification.

Lifespan. Lifespan was measured on NGM plates. Animals were transferred to fresh plates each day until day 5 of adulthood (Ad5) and after every 4 days thereafter. Viability was assessed every 2 days by gentle prodding with a platinum pick. Animals that either had internal hatching of progeny or expulsion of internal organs were not counted as deaths.

Mechanosensory touch function. Animals were lightly stroked with a fine-hair pick near pharynx 5 times. Percentage of response was recorded. A positive response means the animal responded in the reverse direction. For example if an animal responded 2 out of 5 times, the animals has a 40% response rate. Percentage of response was recorded.

GST-4::GFP reporter assay. GST-4 is a glutathione S-transferase that facilitates the Phase II detoxification process. Its expression is regulated by *daf-16* and *skn-1 and* is a common reporter of cytosolic stress. Animals expressing *dvIs19*[(pAF15)P_{gst-4}GFP::NLS] were mounted on microscope slides for 40x imaging. Maximum intensity per animal was reported in AU.

Electron microscopy. We prepared animals for TEM analysis by high pressure freezing and freeze substitution (HPF/FS), and followed a standard to preserve ultrastructure. After HPF in a Baltec HPM-010, we exposed animals to 1% osmium tetroxide, 0.1% uranyl acetate in acetone with 2% water added, held at −90°C for 4 days before slowly warming back to -60°C, -30°C, and 0°C, over a 2 day period. We rinsed the samples several times in cold acetone and embedded the samples into a plastic resin before curing them at high temperatures for 1–2 days. We collected serial thin sections on plastic-coated slot grids and post-stained them with 2% uranyl acetate and then with 1:10 Reynold's lead citrate, and examined with a JEOL JEM-1400 Plus electron microscope. By observing transverse sections for landmarks such as the 2nd bulb of the pharynx, it was possible to reach the vicinity of the ALM soma before collecting about 1,500 serial thin transverse sections.

We identified 29 ALM somata in serial sections from 23 blocks. We selected 12 candidate cells that were initially identified using light microscopy to contain touch neurons in the bud phase of exophergenesis. We imaged juxtanuclear regions of interest at high-magnification in serial sections, and we took high power electron tomograms (15K or 20K) in those neighborhoods, comparing regions showing either aggresome-like structures, mitochondria, or large lysosomes. We closely examined those regions for evidence of intermediate filaments surrounding and/or lying inside of the organelles. We used IMOD and TrakEM software for 3D analysis of the regions of interest, and for model-making.

Statistical analysis. Each trial is graphed as a percentage of ALMR exopher occurrence (binary); we used Cochran–Mantel–Haenszel analysis for P - value calculation of at least 3 or more biological trials. For IFD measurements, we used two-tailed t-tests. We analyzed the comparison of number of IFD-inclusions by one-way ANOVA (with Dunnets post-test as noted).

Blinding. For exopher measurements, we recorded strain information in a non-visible location. The data were unblinded following completion of the experiment. For blinding microscopy analysis we mounted and imaged all animals on a slide for a given strain. Post-acquisition, the file names were assigned a random number and re-coded. The images were unblinded following analysis of the entire data set.

Optimized hNFL sequence:

aaaaATGTCCTCATTCTCATACGAACCATACTATTCGACCTCTTACAAGCGCCGTTA
CGTTGAGACCCCACGCGTTCACATCTCTTCTGTTCGTTCTGGATACTCTACCGCTC
GTTCTGCCTACTCTTCCTACTCCGCTCCAGTTTCCTCCTCCCTTTCTGTTCGTCGTT
CTTACTCTTCTTCTTCCGGATCCCTTATGCCATCCCTTGAGAACCTTGACCTTTCCC
AAGTCGCTGCTATCTCCAACGATCTTAAGTCTATCCGTACCCAAGAGAAGGCTCAA
CTTCAAGATCTTAACGATCGTTTCGCTTCTTTCATCGAGCGTGTTCACGAACTTGAG
CAACAAAACAAGgtaagtttaaacatatatatactaactaaccctgattatttaaattttcagGTTCTTGAGGC
CGAGCTTCTTGTTCTTCGTCAAAAGCACTCTGAGCCATCTCGTTTCCGTGCTCTTTA
CGAGCAAGAGATCCGTGATCTTCGTCTTGCTGCTGAGGACGCTACCAACGAGAAG
CAAGCTCTTCAAGGAGAGCGTGAGGGACTTGAGGAGACCCTTCGTAACCTTCAAG
CTCGTTACGAGGAGGAGGTTCTTTCCCGTGAGGATGCTGAGGGACGTCTTATGGA
GGCTCGTAAGGGAGCTGACGAGGCTGCCCTTGCCCGTGCTGAGCTTGAGAAGCG
TATCGATTCCCTTATGGATGAGATCTCCTTCCTTAAGAAGGTTCACGAGGAGGAGA
TCGCTGAGCTTCAAGCTCAAATCCAATACGCTCAAATCTCTGTTGAGATGGATGTT
ACCAAGCCAGACCTCTCCGCTGCTCTTAAGGATATCCGTGCTCAATACGAGAAGCT
TGCTGCTAAGgtaagtttaaacagttcggtactaactaaccatacatatttaaattttcagAACATGCAAAACG
CCGAAGAGTGGTTCAAGTCTCGTTTCACCGTTCTTACCGAGTCCGCTGCTAAGAAC
ACCGATGCTGTCCGTGCTGCTAAGGATGAGGTTTCTGAGTCCCGTCGTCTTCTTAA
GGCTAAGACCCTTGAGATCGAGGCTTGCCGCGGAATGAACGAGGCTCTTGAGAAG
CAACTTCAAGAGCTTGAGGATAAGCAAAACGCTGATATCTCCGCCATGCAAGATAC
TATCAACAAGCTTGAGAACGAGCTTCGCACCACCAAGTCTGAGATGGCTCGCTAC
CTTAAGGAGTACCAAGATCTTCTTAACGTCAAGgtaagtttaaacatgattttactaactaactaatctg
atttaaattttcagATGGCCCTTGACATCGAGATCGCTGCCTACCGTAAGCTTCTTGAGGG
AGAGGAGACCCGCCTTTCTTTCACCTCTGTTGGATCTATCACCTCTGGATACTCTC
AATCTTCTCAAGTTTTCGGACGTTCCGCTTACGGAGGACTTCAAACCTCTTCTTACC
TTATGTCTACCCGTTCTTTCCCATCTTACTACACCTCTCACGTTCAAGAAGAACAAA
TCGAGGTTGAGGAGACTATCGAGGCCGCTAAGGCCGAGGAGGCTAAGGACGAAC
CACCATCCGAGGGAGAGGCTGAAGAAGAAGAGAAGGATAAGGAGGAGGCTGAGG
AGGAGGAGGCTGCCGAGGAGGAGGAGGCCGCTAAGGAGGAGTCCGAGGAGGCT
AAGGAGGAGGAGGAGGGAGGAGAGGGAGAGGAGGGAGAGGAGACTAAGGAGGC
CGAGGAAGAAGAGAAGAAGGTCGAGGGAGCCGGAGAGGAGCAAGCTGCCAAGAA
GAAGGAC

Figure legends

Figure 1. Intermediate filaments IFD-1 and IFD-2 act cell autonomously in the exopher pathway.

For most exopher scoring throughout this work we applied the Cochran-Mantel-Haenszel test (CMH), error bars are SEM; * $P < 0.05$, ** $P < 0.005$, *** $P < 0.0005$.

A) A typical exopher is readily visualized by mCherry. In strain ZB4065 *bzIs166*[$P_{mec\text{-}4}$mCherry] mCherry is expressed from an integrated high-copy-number transgene array and induces exophergenesis. Ventral touch neuron, AVM (**A**nteroior **V**entral **M**icrotubule touch neuron) and ALMR(**A**nterior **L**ateral **M**icrotubule, **R**ight side) mechanosensory touch neuron and an ALMR-derived exopher pictured. Scale bar = 2 µm.

B) Formation of exophers. Cartoon depiction of the exophergenesis process. 1) A normal neuronal soma depicted. 2) The neuronal soma swells, cellular contents polarize, a swelling and budding out process occurs resulting in a prominent exopher bud. 3) The exopher bud continues to bud outward; the exopher bud forms into an exopher. The exopher can remain attached by a thin filament or become unattached.

C) Deletion of *ifd-1*, *ifd-2* decreases ALMR exophers and the double mutant has exopher levels similar to single mutants. We scored ALMR exopher production on Ad2 in the *ifd-1(ok2404)* deletion mutant, the *ifd-2(bz187)* deletion mutant, and the double *ifd* deletion mutant *ifd-1(*Δ*);ifd-2(*Δ*)*, all of which harbored the exopher-inducing *bzIs166*[$P_{mec\text{-}4}$mCherry] integrated transgene. The ALMR exopher percentage in the *ifd-1(*Δ*);ifd-2*(Δ*)* double mutant is not significantly different from the single mutant *ifd-1*, (P = 0.351); double mutant to *ifd-2* P = 0.0952. ALMRs scored > 391/strain, 6 trials.

D) Single copy $P_{mec\text{-}7}$GFP::IFD-1 rescues the exopher suppression phenotype of the *ifd-1(ok2404)* mutant. We scored ALMR exophers at Ad2 in *bzIs166*[$P_{mec\text{-}4}$mCherry] compared to *bzIs166*[$P_{mec\text{-}4}$mCherry]; *ifd-1(ok2404)*. $P_{mec\text{-}4}$mCherry compared to $P_{mec\text{-}4}$mCherry; *ifd-1(ok2404);bzSi3*[$P_{mec\text{-}7}$GFP::IFD-1] is not significantly different (P = 0.427). N > 552 ALMR/strain, 10 trials.

E) Single copy $P_{mec\text{-}7}$*mNeonGreen*::IFD-2 rescues the exopher suppression phenotype of the *ifd-2(bz187)* mutant. We measured Ad2 exophers in ALMR. *bzIs166*[$P_{mec\text{-}4}$mCherry] compared to *bzIs166*[$P_{mec\text{-}4}$mCherry];*ifd-2(bz187).* *bzIs166*[$P_{mec\text{-}4}$mCherry] compared to *bzIs166*[$P_{mec\text{-}4}$mCherry];*ifd-2(bz187);bzSi37[*$P_{mec\text{-}7}$mNeonGreen::IFD-2] is not significantly different (P = 0.40). N > 179 ALMR/strain, 5 trials.

Figure 2. In the soma IFD-1 and IFD-2 colocalize to juxtanuclear inclusions that become larger with age and are distinct from other organelles.

For images as indicated, touch cell soma outline is indicated by a continuous line and nucleus is marked by a dotted line.

A) **GFP::IFD-1 concentrates in juxtanuclear inclusions.** Shown is a representative Ad2 ALM touch neuron, DIC-GFP merge, strain ZB4723 *bzIs166*[$P_{mec\text{-}4}$mCherry]; *ifd-1*(*ok2404*)X; *bzSi3*[$P_{mec\text{-}7}$GFP::IFD-1], expressing a rescuing, single-copy GFP::IFD-1 transgene. Solid white lines outline the touch neuron soma. Image is representative of N > 40 for this strain. Scale bar = 2 μm.

B) **mNeonGreen::IFD-2 concentrates in juxtanuclear inclusions.** Shown is a representative Ad2 ALM touch neuron, DIC-GFP merge, strain expressing *bzIs166*[$P_{mec\text{-}4}$mCherry];*bzSi37*[$P_{mec\text{-}7}$mNeonGreen::IFD-2]. Solid white lines outline the touch neuron soma. Image is representative of N > 20 with visible expression for this strain. Scale bar = 2 μm.

C) **IFD-1-positive inclusions become larger with age. Top:** L4 larval stage ALM neuron. **Bottom:** Ad11 ALM neuron. Strain expressing *bzIs166*[$P_{mec\text{-}4}$mCherry]; *bzSi3*[$P_{mec\text{-}7}$GFP::IFD-1]**.** Solid white lines outline the touch neuron soma. Images representative of > 100 observations. Scale bar = 2 μm.

D) **IFD-1 and IFD-2 colocalize to juxtanuclear inclusions.** Representative of adult touch neuron, strain expressing *bzEx279*[$P_{mec\text{-}7}$GFP::IFD-1 $P_{mec\text{-}7}$RFP::IFD-2]. Image is representative of N > 20. Scale bar = 2 μm. Quantitation of colocalization in panel E.

E) **GFP::IFD-1 does not extensively colocalize with a Golgi marker.** Representative of adult touch neuron, strain expressing *bzIs166*[$P_{mec\text{-}4}$mCherry]; *bzEx265*[$P_{mec\text{-}4}$ TagBFP::AMANS-2]; *bzSi3*[$P_{mec\text{-}7}$GFP::IFD-1]. Image is representative of N > 20. Scale bar = 2 μm. Quantitation of colocalization in panel F.

F) **GFP::IFD-1 does not extensively colocalize with the LMP-1::mSc lysosome marker.** Representative of adult touch neuron, strain expressing *bzIs3*[$P_{mec\text{-}7}$GFP::IFD-1]; *pwSi222*[$P_{mec\text{-}7}$LMP-1::mScarlet]. Representative of N > 20. Scale bar = 2 μm. Quantitation of colocalization in panel G.

G) **IFD inclusion does not colocalize with mitoROGFP mitochondria marker.** Representative of adult touch neuron, strain expressing *bzEx253*[$P_{mec\text{-}7}$RFP::IFD-2]; *zhsEx17*[$P_{mec\text{-}4}$mitoLS::ROGFP]. Representative of N > 20. Scale bar = 2 μm. Quantitation of colocalization in panel H.

H) Colocalization correlation of GFP::IFD-1 and RFP::IFD-2 signals (panel D) graphed as Pearson's Coefficient of red and green channel. N = 10, error bars are SEM.

I) Colocalization correlation of GFP::IFD-1 and TagBFP::AMANS-2 signals (panel E) graphed as Pearson's Coefficient of blue and green channel. N = 10, error bars are SEM.

J) Colocalization correlation of GFP::IFD-1 and mSc::LMP-1 signals (panel F) graphed as Pearson's Coefficient of red and green channel. N = 10, error bars are SEM.

K) Colocalization correlation of RFP::IFD-2 and mitoROGFP (panel G) graphed as Pearson's Coefficient of red and green channel. N = 10, error bars are SEM.

Figure 3. Genesis of juxtanuclear IFD inclusions depends on functional microtubules and dynein. Aggregate adapter proteins 14-3-3/FTT-2 and HSP-1 colocalize with IFD-positive organelles.

White dashed line outlines nucleus in panels where indicated.

A) **Mammalian aggregate-adapter complex.** Adapted from paper Xu 2013 [43], created with BioRender.com. 14-3-3 proteins are able to bind directly to dynein components. 14-3-3 binds BAG3 bound Hsc70/(HSP-1). Hsc70/HSP-1 is able to recognize and bind ubiquitinylated aggregates. The complex moves along the microtubule tracks to deliver to the aggresome compartment.

B) **Microtubule inhibition via colchicine treatment from L4 to Ad2 reduces IFD-1-positive inclusion formation.** Strain expressing *bzIs166*[$P_{mec\text{-}4}$mCherry]; *bzSi3*[$P_{mec\text{-}7}$GFP::IFD-1]**. Left:** Control, DMSO added from L4 to Ad2, Ad2 ALM. **Right:** 5 mM colchicine added from L4 to Ad 2, Ad2 ALM. Scale bar = 2 μm. Image representative of N > 90.

C) **Microtubule inhibition via colchicine increases the number of IFD-1 puncta.** Number of IFD-1-positive puncta per Ad2 ALM. Control DMSO, colchicine 5 mM. L4 to Ad2 exposure. $P < 0.0005$, N > 27/strain, 3 trials, two-tailed t-test, error bars are SEM.

D) **Touch neuron-specific dynein knockdown via auxin inducible degradation of DHC-1::degron reduces IFD-positive puncta formation.** Knockdown strain expressing *bzIs166*[P_{mec-4}mCherry]; *bzSi6*[P_{mec-7}TIR-1::TagBFP]; *bzSi3*[P_{mec-7}GFP::IFD-1]; *dhc-1*(*ie28*[DHC-1::degron::GFP]) and control strain lacking the TIR-1 component (*bzSi6*[P_{mec-7}TIR-1::TagBFP]) and therefore not susceptible to degradation. **Left:** Control TIR-1 -/-, Ad2 ALM. **Right:** TIR-1 +/+, Ad2 ALM; 5 mM auxin exposure to the control and the experimental, from L4 to Ad2. Scale bar = 2 μm. Image representative of N > 90.

E) **Touch neuron-specific dynein knockdown increases the number of GFP::IFD-1 puncta:** Number of IFD-1-positive puncta per Ad2 ALM. Auxin exposure to both the control and the experimental from L4 to Ad2. $P < 0.05$, N > 25 / strain, 3 trials, two-tailed t-test, error bars are SEM.

F) **FTT-2::mSc colocalizes with juxtanuclear GFP::IFD-1.** Representative of adult touch neuron expressing *bzSi51*[P_{mec-7}FTT-2::mSc]; *bzIs3*[P_{mec-7}GFP::IFD-1], N > 10. Scale bar = 2*μm*. Quantitation of co-localization of N = 10, graphed as Mander's overlap coefficient of GFP channel over mScarlet channel.

G) **mSc::HSP-1 colocalizes with GFP::IFD-1.** HSP-1/Hsc70 is essential for recognizing ubiquitinated aggregates for aggresomal collection in mammalian biology [43, 86]. Representative of adult touch neuron expressing *bzSi53*[P_{mec-7}mSc::HSP-1]; *bzIs3*[P_{mec-7}GFP::IFD-1]. Representative of N > 10. Scale bar = 2 *μm*. Quantitation of co-localization of N = 10, graphed as Mander's overlap coefficient of GFP channel over mScarlet channel.

Figure 4. Disease-associated human Htt-polyglutamine expansion protein colocalize with IFD-1 in touch neurons.

White dashed line outlines nucleus in all panels.

A) **mNG::UBQ-2 ubiquitin expressed from a single-copy-number transgene colocalizes with mSc::IFD-1.** *ubq-2* includes a canonical ubiquitin fused to the L40 ribosomal large subunit protein; the polypeptide that is cleaved to generate a single ubiquitin that can covalently attach to target proteins [87]. We expressed mNG::UBQ-2 from single copy *bzSi38*[P_{mec-7}mNG::UBQ-2], which expresses in touch neurons. mNG::UBQ-2 concentrates to specific subcellular structures including perinuclear IFD-1 and additional foci that are distinct, which would be

expected for the range of activities/sites in which ubiquitin is engaged, such as on late endosomes. Representative adult touch neuron expressing *bzSi38*[P_{mec-7}mNG::UBQ-2]; *bzSi34*[P_{mec-7}mSc::IFD-1]. Image is representative of N > 10. Scale bar = 2 μm. Quantitation of co-localization of N = 10, graphed as Mander's overlap coefficient of mScarlet channel over mNeonGreen channel.

B) **mNG::UBQ-2 ubiquitin colocalizes with mSc::IFD-2.** Representative adult touch neuron expressing *bzEx422*[P_{mec-7}mNG::UBQ-2]; *bzEx421*[P_{mec-7}mSc::IFD-2]. mNG::UBQ-2 concentrates to specific subcellular structures including perinuclear IFD-2 and additional foci that are distinct, which would be expected for the range of activities/sites in which ubiquitin is engaged, such as on late endosomes. Image is representative of N > 10. Scale bar = 2 μm. Quantitation of co-localization of N = 10, graphed as Mander's overlap coefficient of mScarlet channel over mNeonGreen channel.

Although we cannot rule out that high expression drives the mNG::UBQ-2 to the IFD domain, the compartmentalization to specific subcellular localizations is a pattern reported in other ubiquitin studies [88, 89].

C) **HttQ74::mNG expressed from a single-copy-number transgene colocalizes with mSc::IFD-1.** Representative adult touch neuron expressing *bzSi39*[P_{mec-7}HttQ74::mNG]; *bzSi34*[P_{mec-7}mSc::IFD-1]. Images selected were those in which mNG was visibly aggregated in the cell, as opposed to homogenous dim cytosolic signal. Representative of N > 10 with mNG aggregates. Scale bar = 2 μm. Quantitation of colocalization of N = 10, graphed as Mander's overlap coefficient of mScarlet channel over mNeonGreen channel.

D) **HttQ74::mNG expressed from a single-copy-number transgene colocalizes with mSc::IFD-2.** Representative adult touch neuron expressing b*zSi40*[P_{mec-7}mNG::HttQ74]; *bzEx420*[P_{mec-7}mSc::IFD-2] of animals that display visible mNG aggregation. Image is representative of N > 10. Scale bar = 2 μm. Quantitation of co-localization of N = 10 of animals that display visible mNG aggregation, graphed as Mander's overlap coefficient of mScarlet channel over mNeonGreen channel.

E) **HttQ128::CFP expressed from an integrated high-copy-number array colocalizes with mSc::IFD-1.** Representative adult touch neuron expressing *igIs*1[P_{mec-7} YFP P_{mec-3}HttQ128::CFP]; *bzSi34*[P_{mec-7}mSc::IFD-1]. Representative of N > 10 with an overlapping localization. Scale bar = 2 μm. Quantitation of co-localization of N = 10, graphed as Mander's overlap coefficient of mScarlet

channel over mNeonGreen channel. See Supplementary Figure 14 for additional localization patterns for HttQ128::CFP and mSc::IFD-1.

Figure 5. FTT-2/14-3-3 adapter protein that works in a complex with HSP-1/Hsc70 is required for aggresome formation. FTT-2 and HSP-1 are required for exopher formation.

A) **IFD-1-positive puncta size decreases in *ftt-2(n4426).*** Diameter, in µm, of Ad1 IFD-1-positive puncta in ALM neurons decreases in the *ftt-2* background, in a strain expressing *bzIs166*[P_{mec-4} mCherry]; *bzSi3*[P_{mec-7} GFP::IFD-1]. $P < 0.0001$, $N > 50$, 3 trials, two-tailed t-test, error bars are SEM. Animals measured on Ad1 to reduce animal-bagging occurrence.

B) **IFD-1-positive puncta number per ALM neuron remains the same in control and *ftt-2(n4426).*** Number of IFD-1-positive inclusions in Ad1 ALM somas does not change in mutant *ftt-2(n4426)* versus WT in strains expressing *bzIs166*[P_{mec-4} mCherry]; *bzSi3*[P_{mec-7} GFP::IFD-1]. NS, $P = 0.87$, $N > 50$ / strain, 3 trials, two-tailed t-test, error bars are SEM. Animals measured on Ad1 to reduce animal-bagging occurrence.

C) **14-3-3/FTT-2 is required for efficient exopher production.** There is a significant reduction of percentage of ALMR exopher production on Ad1 in the genomic deletion *ftt-2(n4426*) strain expressing *bzIs166*[P_{mec-4} mCherry]; *bzSi3*[P_{mec-7} GFP::IFD-1]. $P < 0.05$, $N > 275$, 8 trials, Cochran-Mantel-Haenszel test, error bars are SEM. Animals measured on Ad1 to reduce animal-bagging occurrence.

D) **Mammalian aggregate-adapter complex.** Adapted from paper Xu 2013 [43] created using BioRender.com. 14-3-3 proteins are able to bind directly to dynein components. 14-3-3 binds BAG3 bound Hsc70/(HSP-1). Hsc70/HSP-1 is able to recognize and bind ubiquitinylated aggregates. The complex moves along the microtubule tracks to deliver to the aggresome compartment. **Note:** We did not find an impact of *unc-23*/BAG3 mutation or RNAi on exophers (data not shown) and speculate that the HSP-1/14-3-3 complex might be simpler in nematodes as compared to mammals, or another protein may provide the UNC-23 role in the complex.

Note that Pan-neuronal-specific RNAi against *hsp-1* trends to reduce Ad2 ALMR exophergenesis (P = NS, 78% confidence). Upon 2 generations of RNAi exposure in

a pan-neuronally-specific RNAi strain expressing *sqIs71*[P_{rgef-1}GFP; P_{rgef-1}SID-1;pBS]; *sid-1(qt9)*V; *bzIs101*[P_{mec-4}mCherry], P = 0.221. 5 trials, N = 250, Cochran-Mantel-Haenszel test.) Non-significant results could reflect a number of reasons, for example, ability for neuronal *hsp-1* targeting, or can be due to effects on *hsp-1*s multiple ubiquitous roles in neurons. We hypothesize that *hsp-1* works in a complex with FTT-2 for aggresome delivery and that both are important for exophergenesis.

E) HSP-1 is required for efficient exopher production in touch neuron-sensitized RNAi strain. RNAi exposure to *hsp-1*-targeted RNAi clone from L4 to Ad2 in a neuronally-sensitized RNAi strain harboring *bzIs169* [P_{mec-18}*sid-1* P_{sng-1}YFP]; *bzIs101* [P_{mec-4}mCherry] significantly reduces ALM exophergenesis. Ad2 P < 0.0005, N > 130, 4 trials, Cochran-Mantel-Haenszel test, error bars are SEM.

F) 14-3-3/FTT-2 is required for efficient exopher production in touch neuron-sensitized RNAi strain. There is a significant reduction of percentage of ALMR exopher production with *ftt-2*-targetting RNAi clone in a touch neuron sensitized RNAi strain expressing *bzIs169*[P_{mec-18}SID-1 P_{sng-1}YFP]. P < 0.05, N > 85, 3 trials, Cochran-Mantel-Haenszel test, error bars are SEM. Animals measured on Ad1 to reduce animal-bagging occurrence.

G) Pan-neuronal-specific RNAi against *ftt-2* significantly reduces exophergenesis. 2 generations of RNAi exposure to *ftt-2*-targeted RNAi clone in a pan-neuronally-specific RNAi strain expressing *sqIs71*[P_{rgef-1}GFP; P_{rgef-1}SID-1;pBS]; *sid-1(qt9)*V; *bzIs101*[P_{mec-4}mCherry] significantly reduces Ad2 ALMR exophergenesis. P = 0.0025, 5 trials, N = 250, Cochran-Mantel-Haenszel test, error bars are SEM.

H) Additional copy of FTT-2::mSc increases ALMR exophergenesis on Ad2. We scored ALMR exopher production on Ad2 in control animals expressing *bzIs166*[P_{mec-4}mCherry] and *bzIs166*[P_{mec-4}mCherry]; *bzSi47*[P_{mec-7}FTT-2::mSc]. Single-copy integrated FTT-2::mSc increases ALMR Ad2 exophergenesis, N > 95, P = 0.035, 3 trials.

Note that fertility disruption can be a concern for some knockdowns ([12] and our unpublished observations). *ftt-2* is expressed in the somatic tissues [90] and knockdown does not block progeny production; we scored on Ad1 to avoid bagging and retention of progeny that can occur at Ad2. *hsp-1* is a more broadly expressed essential gene that can disrupt fertility; so RNAi knockdown, though anticipated to be enhanced in touch neurons [54] and not blocking all progeny production in our experiment, might still impair exophers by compromising fertility.

Figure 6. IF roles in aggregate collection and neuronal aggregate expulsion may be conserved.

A) **mNG::hNFL localizes to the IFD-1 positive aggresome.** Shown is a representative ALM touch neuron. We optimized the coding sequence of human NFL, NM_006158.5, for *C. elegans* expression based on published codon biases as described in Methods. We added mNeonGreen fluorophore and expressed the construct under the *mec-7* touch neuron promoter. Strain expressing *bzEx269*[$P_{mec\text{-}7}$mNG::hNFL] and *bzSi34*[$P_{mec\text{-}7}$mSc::IFD-1]. Solid white lines outline the touch neuron soma, dotted outline is the nucleus. Image is representative of N > 20. Scale bar = 2 μm. Graphed as Mander's overlap coefficient of mScarlet channel over mNeonGreen channel, N = 10 graphed, error bars are SEM.

B) **mSc::hNFL colocalizes with mNG::UBQ-2 ubiquitin.** Representative adult touch neuron expressing *bzEx313*[$P_{mec\text{-}7}$mNG::UBQ-2]; *bzSi43*[$P_{mec\text{-}7}$mSc::hNFL]. Image is representative of N > 10. Scale bar = 2 μm. Quantitation of co-localization of N = 10, graphed as Mander's overlap coefficient of mScarlet channel over mNeonGreen channel.

C) **mSc::hNFL colocalizes with mNG::HttQ74.** Representative adult touch neuron expressing *bzSi39*[$P_{mec\text{-}7}$mNG::HttQ74]; *bzSi43*[$P_{mec\text{-}7}$mSc::hNFL] of animals that display visible mNG aggregation. Image is representative of N > 10. Scale bar = 2 μm. Quantitation of co-localization of N = 10 of animals that display visible mNG aggregation, graphed as Mander's overlap coefficient of mScarlet channel over mNeonGreen channel.

D) **hNFL-labeled aggresomes can be extruded from touch neurons in exophers.** Representative image (N > 10) of mNG::hNFL extrusion in exophers. Strain expressing *bzEx311*[$P_{mec\text{-}7}$mNG::hNFL] with *bzIs166*[$P_{mec\text{-}4}$mCherry] and *ifd-2(bz187)* background. Image shows ALMR neuron with three exophers. Two exophers are positioned in the middle of the image surrounded by scattered mCherry debris, starry night phenotype (SN) from hypodermal exopher digestion [4]. A mature distant exopher contains a large mNG::hNFL inclusion, shown zoomed in, in different exposure from the right exopher. **Graph on right:** Out of N = 34 Ad2 ALMs with an exopher from strain expressing *bzSi48*[$P_{mec\text{-}7}$ mNG::hNFL]; *bzIs166*[$P_{mec\text{-}4}$mCherry], 16 exophers included mNG::hNFL puncta.

E) **Touch neuron specific hNFL rescues an *ifd-2* deficit in exophers. Single copy P_{mec-7}mNG::hNFL rescues the exopher suppression phenotype of the *ifd-2(bz187)* mutant.** We measured Ad2 exophers in ALMR. *bzIs166*[P_{mec-4}mCherry] compared to *bzIs166*[P_{mec-4}mCherry];*ifd-2(bz187). bzIs166*[P_{mec-4}mCherry];*ifd-2(bz187)* compared to *bzIs166*[P_{mec-4}mCherry];*ifd-2(bz187);bzSi48[*P_{mec-7}mNeonGreen::hNFL], both significantly different, $P < 0.005$, N = 200 ALMR / strain, 4 trials.

Supplementary Figure Legends

Supplementary Videos. Demonstration of the distinctive structural differences between membrane layers and intermediate filament types.

P_{mec-4} mCherry animals were staged as adult day 2 with an exopher bud phenotype.

Video 1: Whorl membrane geometry. Movie 1 shows a focus through series in which individual membranes continue through the full depth of the series without dropping out (unlike members of a filament bundle). Membranes often lie in closely packed layers but may bend sharply to double back on themselves. Scale bar is 50 nm.

Video 2: Intermediate Filaments associated with the circular organelle. Movie 2 shows filaments in a focus-through series demonstrates that (unlike membranes) these filaments do not continue through the full depth of the series, but individually disappear (or appear) at different depths within the series. Some longer filaments run for a distance around the organelle, bending gradually, but these filaments are loosely associated and rarely touch one another. Filaments deeper inside the organelle tend to be short, and run at odd angles to one another, rarely pairing. Scale bar is 50 nm.

Supplementary Figure 1. Ultrastructural analysis reveals the presence of intermediate filament assemblies in distinctive perinuclear structures in proteo-stressed ALM neurons.

We selected P_{mec-4}mCherry animals at adult day 2 that had early exopher buds that had not separated from the neuron of origin (12 ALMs examined in EM). We identified touch neuron somata after extensive transverse thin section series. ALM neuron somata (L/R

pair) lay on opposite sides of the midbody, at similar distances from the head and can be unambiguously identified via their characteristic microtubule-filled dendrite features.

A) Lower power TEM view of an ALM neuron in transverse section, embedded in the hypodermis next to the cuticle. A distinctive circular structure (white arrow) lies close to the nucleus (Nuc) and a small mitochondrion (M). Electron lucent contents are dominated by the presence of single filaments. No ribosomes are detectable here, nor other small organelles, which would be expected if the contents derived from typical cytoplasm. Shorter filaments ~ 10 nm in width lie at random angles within the circular organelle, while a single layer of discontinuous filaments of similar width coats the periphery of the organelle. Filament measures are consistent with their identification as intermediate filaments (9.98 nm; > 150 filaments measured). A bundle of microtubules lies just beneath the cuticle layer (cuticle annotated with black arrowheads). Scale bar 500 nm

B) Higher magnification view of the circular organelle from panel A, showing the filaments in higher resolution (white arrows). Red arrow indicates one of the longer filaments taking position at the outer edge of the organelle. Filaments sometimes adopt a zig-zag pattern of bent filaments as they bundle. Note the thinness of IFs compared to the membrane bilayer surrounding the nearby mitochondrion. Demonstration of how intermediate filaments can be visually distinguished from membrane are included in Supplementary Video 1 and Supplementary Video 2. Scale bar 200 nm.

C) Closeup view of a similar rounded organelle (soma of a different animal) in which most intermediate filaments (red arrows) have assembled into a loose bundle that curves as the bundle envelopes most of the periphery. A small number of shorter filaments lie deeper inside the organelle. Scale bar is 200 nm.

D) Thinner view from an electron tomogram shows curving individual filaments bordering the circular structure, but with a denser, tighter accumulation of filaments (between red arrows), at the edge of the organelle. Note also the bundle of microtubules (blue arrows) lying just outside the indicated organelle. Some very dark ribosomes are now seen within the structure, as well as granular matrix material of moderate electron density that likely represents proteinaceous aggregates. Scale bar is 200 nm.

Discussion. Although successive sequencing is not possible for individual samples, we speculate that the juxtanuclear structures might mature by increasing and expanding the proteinaceous center and adding more intermediate filaments to the periphery.

Ultrastructure of mammalian aggresomes has been reported in cultured HEK cells, with aggresomes described as electron dense cores of (CFTR)-aggregated protein deposits devoid of membrane surroundings, deposited likely intimate to the nuclear membrane, and surrounded by 8 - 10 nm sized filaments that form loosely parallel bundles [8]. Distorted ‘tangles’ of IFs within the dense aggresome core have been noted; organelles

can be positioned nearby the aggresome similar to our EM observations (mitochondria in Supplementary Figure 1A) and microscopy observations (Figure 2G).

Overall, we note that limited low resolution EM data exist on aggresome-focused EM [14, 15, 91]). Although the initial description described IF "cages" was based on fluorescent microscopy [8], available EM data suggest at best loose and somewhat disorganized IF networks in aggresome structure, similar to what we report here.

Supplementary Figure 2. Intermediate filament RNAi knockdown decreases exopher production.

A) **Intermediate filament RNAi knockdown in a neuronally-sensitized RNAi strain decreases exopher production.** We performed RNAi knockdown of each of the 11 *C. elegans* intermediate filament genes, beginning at the L4 larval stage and assaying ALMR exophers on Ad2, screen strain ZB4071 *bzIs169*[P_{mec-18} *sid-1* P_{sng-1}YFP]; *bzIs101*[P_{mec-4}mCherry; P*unc-119*+]. Note that in this strain RNAi should be effective in all cells but neurons; except for in touch neurons which express the *sid-1* dsRNA transporter. Sequence-confirmed RNAi clones were empty vector negative control (EV), *ifa-1*, *ifa-2*, *ifa-3*, *ifa-4*, *ifb-1*, *ifb-2*, *ifc-1*, *ifc-2*, *ifp-1*, *ifd-1*, and *ifd-2.* RNAi knockdown > 292 ALMR scored/clone, 4 trials. * P < 0.05, ** P < 0.005, *** P < 0.0005.

B) **Intermediate filament RNAi knockdown in a neuron-specific RNAi strain decreases exopher percentage**. We performed RNAi knockdown of each of 9 *C. elegans* intermediate filament genes, exposing animals to RNAi clones for 2 generations, and assaying ALMR exophers on Ad2, screen strain ZB5184 *bzIs166* [P*mec-4*mCherry1] II; *sid-1(qt9)* V; *sqIs71* [P*rgef-1*GFP; P*rgef-1sid-1*;pBS]. Note that in this strain, RNAi should be effective only in all neurons. Sequence-confirmed RNAi clones were empty vector negative control (EV), *ifa-1*, *ifa-2*, *ifa-3*, *ifb-1*, *ifb-2*, *ifc-1*, *ifc-2*, *ifd*-1, and *ifd-2.* RNAi knockdown N = 250 ALMR/clone, 5 trials. * P < 0.05, ** P < 0.005, *** P < 0.0005.

C) **Intermediate filament RNAi knockdown in the *ifd-1(Δ); ifd-2(Δ)* double mutant background can exacerbate decreases in exopher percentage to less than 5%.** We performed RNAi knockdown of 10 *C. elegans* intermediate filament genes, exposing animals to RNAi clones from L4-Ad2, and assaying ALMR exophers on Ad2, screen strain ZB5247*: ifd-1(ok2404)*; *ifd-2(bz187)*; *bzIs166*[P_{mec-4} mCherry]; *uIs71*[(pCFJ90) P_{myo-2}mCherry + P_{mec-18}SID-1]. Note that in this strain, all cells but neurons are amenable to RNAi but transcripts in touch neurons should be targeted by RNAi as touch neurons express the

neuronal dsRNA transporter *sid-1;* disruptions might not act cell autonomously. Sequence-confirmed RNAi clones were empty vector negative control (EV), *ifa-1*, *ifa-2*, *ifa-3*, *ifb-1*, *ifb-2*, ifp-1, *ifc-1*, *ifc-2*, and control clones - *ifd-1*, and *ifd-2.* RNAi knockdown was performed in the *ifd-1(ok2404)*; *ifd-2(bz187)* double mutant background, congruently, RNAi targeting to either *ifd-1* or *ifd-2* does not change exopher levels compared to the EV control, suggesting that off-target effects are not potent in this study. RNAi knockdowns were 200 ALMR/clone, 4 trials. Note that some experimental RNAi clones were assayed on the same day and therefore used the same empty vector control. Each clone has been graphed separately with day-matched EV controls, for simplicity. Also note that very low baseline exopher levels are present for the *ifd-1(Δ)*; *ifd-2(Δ)* starting strain so that any role implied by these RNAi data would have to be confirmed by independent genetic perturbation and cell autonomy analysis to confirm. Candidates for further study highlighted by this screen are: *ifa-2, ifb-2, ifc-2, ifa-3* and *ifp-1*. * $P < 0.05$, ** $P < 0.005$, *** $P < 0.0005$.

Supplementary Figure 3 Health, development, lifespan and stress response measures of the *ifd* mutants.

Strains ZB4065 *bzIs166*[P_{mec-}4mCherry], ZB4722 *ifd-1(ok2404);bzIs166*[P_{mec-}4mCherry], and ZB4655 *ifd-2(bz187); bzIs166*[P_{mec-}4mCherry].

A) **Body length** in μM as measured from 10x images taken from dissection microscope. Synchronized Ad2 animals. N > 30, NS, 3 trials, One-way *anova.*

B) **Body width** as measured from 10x images taken from dissection microscope. Synchronized Ad2 animals. N > 30, NS, 3 trials, One-way *anova.*

C) **Brood size**. Progeny per adult. Larval animals were placed onto individual plates. Progeny of these animals were counted during their entire life span and is given as an average number per individual. N = 9, P = NS, 3 trials, One-way *anova.*

D) **Development for *ifd-1(ok2404)*.** Hours from egg to develop into young adult stage. Isolated embryos (synchronized by an hour egg lay using 50 animals) were placed onto each plate. Individual larvae were monitored every day for animals becoming L4 stage. Time of development was calculated by the average number of days animals needed to reach adulthood. N > 150, P = 0.72, 3 trials. Statistical significance was calculated using an unpaired two-tailed t-test where mean values of 3 trials were considered using GraphPad Prism.

E) Development for *ifd-2(bz187)*. Hours from egg to develop into young adult stage. Isolated embryos (synchronized by an hour egg lay using 50 animals) were placed onto each plate. Individual larvae were monitored every day for animals becoming L4 stage. Time of development was calculated by the average number of days, animals needed to reach adulthood. N > 150, P = 0.38, 3 trials. Statistical significance was calculated using an unpaired two-tailed t-test where mean values of 3 trials were considered using GraphPad Prism [92].

F) Lifespan. *ifd-1(ok2404); bzIs166*[P_{mec}-4mCherry].

G) Lifespan. *ifd-1(ok2404); bzIs166*[P_{mec}-4mCherry].

Graphed as days until death. Embryos were isolated; subsequently hatched animals where scored for viability every day using a platinum wire for mechanical stimulation. Animals moving upon stimulation were judged to be alive. Animals that could not be located on the plate throughout the experiments were excluded. Animals were transferred at least every two days to prevent mix-up with their hatched progeny. N > 150, *ifd-1* P = 0.9442; *ifd-2* P = 0.1152, 3 trials, Statistical analysis was performed using the survival function and the Gehan-Breslow-Wilcoxon Test of GraphPad Prism [92].

H) Oxidative stress. Hours on paraquat graphed over survival. Strains *ifd-1(ok2404);bzIs166*[P_{mec}-4mCherry] and *ifd-2(bz187); bzIs166*[P_{mec}-4mCherry]. For oxidative stress we used 200 mM paraquat in NGM agar. Plates were stored overnight at room temperature and subsequently inoculated with concentrated OP50 overnight culture. Following overnight incubation at room temperature plates were ready to use. We started oxidative stress experiments by transferring L4 larvae onto the bacterial lawn. We scored animals hourly for viability using mechanical stimulation with a platinum wire. No response animals were scored dead. Plates without paraquat were used as controls. N > 150*, ifd-1* P = 0.0004, *ifd-2* P = 0.076, 3 trials. Statistical analysis was done using the survival function and the Gehan-Breslow-Wilcoxon Test of GraphPad Prism [92].

I) Osmotic stress. Percent survival after 24 hours of exposure to 450 mM NaCl concentrated plates. Strains *ifd-1(ok2404);bzIs166*[P_{mec}-4mCherry] and *ifd-2(bz187); bzIs166*[P_{mec}-4mCherry]. For osmotic stress we used NGM agar with 450 mM NaCl. Plates were stored overnight at room temperature and subsequently inoculated with concentrated OP50 overnight culture. Following

overnight incubation at room temperature plates were ready to use. We started osmotic stress experiments by transferring L4 larvae onto the bacterial lawn followed by an overnight incubation. Subsequently, animals were washed in recovery buffer (M9 buffer with 150 mM NaCl) and transferred to normal NGM plates. The viability of each animal was scored after an additional overnight incubation using mechanical stimulation through a platinum wire. N > 150, *ifd-1* P = 0.329 , *ifd-2* P = 0.76, 3 trials, two-tailed t-test was used for significance calculation. [92].

J) GST-4 expression in *ifd-1(ok2404).* GST-4 is a glutathione S-transferase that facilitates the Phase II detoxification process. Its expression is regulated by *daf-16* and *skn-1* and is a common reporter of cytosolic stress. Maximum intensity per animal reported in AU. GST-4::GFP expression is NS (P = 0.16) in *ifd-1* mutants. N > 30, 3 trials. Two-tailed t-test. Strains: *dvIs19*[(pAF15)P_{gst-4}GFP::NLS] and *dvIs19*[(pAF15) P_{gst-4}GFP::NLS]; *ifd-1(ok2404).*

K) GST-4 expression in *ifd-2(bz187).* Maximum intensity per animal reported in AU. GST-4::GFP expression is significantly reduced in *ifd-2* animals (P = 0.0256). N > 30, 3 trials. Two-tailed t-test. Strains: dvIs19[(pAF15)P_{gst-4}GFP::NLS] and dvIs19[(pAF15)P_{gst-4}GFP::NLS]; *ifd-2(bz187).*

Previously published studies suggest that baseline exopher levels in mCherry expressing animals, *bzIs166,* are not markedly changed by deletion of *daf-16, hsf-1, hif-1, hlh-30*, or *skn-1* [11]; the interpretation is that there is redundancy for baseline pathways, or these stress responses are not critical for baseline exopher production.

Supplementary Figure 4. Neuronal ALM morphology and mechanosensory touch function remain preserved in *ifd* mutants.

A) ALM morphology of strains *ifd-1(ok2404);bzIs166*[P_{mec}-4mCherry] and *ifd-2(bz187); bzIs166*[P_{mec}-4mCherry]. Axonal beading and soma outgrowth percentage observed scored on Ad2 (the peak of exophergenesis[4]) and are graphed per trial. Beading and outgrowths are associated with age, stress, and neurodegeneration [93]. NS, One-way *anova*. N > 30, 3 trials.

B) Mechanosensory touch function on Ad1, Ad5, Ad10 for *ifd-1(ok2404);bzIs166*[P_{mec}-4mCherry] and *ifd-2(bz187); bzIs166*[P_{mec}-4mCherry]. Animals were lightly stroked with a fine-hair pick near pharynx five times. Percentage of response was recorded. A positive response means the animal responded in the reverse direction. For example if an animal responded 2 out of

5 times, the animals has a 40% response rate. Percentage of response was recorded on respective days. NS, One-way *anova.* Ad1 - 3 trials, N > 90, Ad5 - 1 trial N > 30, Ad10 - 3 trials, N > 90.

New Supplementary Figure 5. *ifd-1* and *ifd-2* deletions decrease ALMR exophers as reported by a highly expressed cytosolic GFP reporter.

A) We scored ALMR exopher production on Ad2 in the *ifd-1(ok2404)* deletion mutant and the *ifd-2(bz187)* deletion mutant, each of which also harbored *uIs31*[P_{mec-17}GFP] integrated transgene. N > 331, 6 trials. *ifd-1*(P < 0.0005); *ifd-2* (P < 0.0005). Data support that *ifd* disruptions modulate exopher levels independent of the fluorescent reporter used for exopher detection. * P < 0.05, ** P < 0.005, *** P < 0.0005.

B) Representative Ad2 exopher from *uIs31*[P_{mec-17}GFP].

New Supplementary Figure 6. Touch neuron specific tagged IFD transgenes can rescue IF exopher deficit.

A) We scored ALMR exophers at Ad2 in *bzIs166*[P_{mec-4}mCherry] compared to *bzIs166*[P_{mec-4}mCherry]; *ifd-1(ok2404)* (P < 0.0178). *bzIs166*[P_{mec-4}mCherry] compared to *bzIs166*[P_{mec-4}mCherry]; *ifd-1(ok2404); bzEx253*[P_{mec-7}GFP::IFD-2 OE] is NS, P = 0.0642. N > 425, 11 trials.

B) We scored ALMR exophers at Ad2 in *bzIs166*[P_{mec-4}mCherry] compared to *bzIs166*[P_{mec-4}mCherry]; *ifd-2(bz187)* (P < 0.05). *bzIs166*[P_{mec-4}mCherry] compared to *bzIs166*[P_{mec-4}mCherry]; *ifd-2(bz187); bzEx253*[P_{mec-7}RFP::IFD-2] is NS. N > 240, 7 trials.

C) We scored ALMR exophers at Ad2 in *bzIs166*[P_{mec-4}mCherry] compared to *bzIs166*[P_{mec-4}mCherry]; *ifd-1(ok2404); ifd-2(bz187)* (P < 0.054). *bzIs166*[P_{mec-4}mCherry] compared to *bzIs166*[P_{mec-4}mCherry]; *ifd-1(ok2404); ifd-2(bz187); bzEx270*[P_{mec-7}GFP::IFD-1 OE] is NS. N >128, 4 trials.

New Supplementary Figure 7. IFD-1-puncta form the same without *ifd-2*.

A) **IFD-1-positive puncta size remains the same in *ifd-2(bz187)*.** Diameter, in µm, of Ad2 IFD-1-positive puncta in ALM neurons remains the same in the *ifd-2* background, in a strain expressing *bzIs166*[P_{mec-4} mCherry]; *bzSi3*[P_{mec-7} GFP::IFD-1]. P = NS, N > 55, 3 trials, two-tailed t-test, error bars are SEM.

B) **IFD-1-positive puncta form juxtanuclearly with or without *ifd-2(bz187).*** Percentage of juxtanuclear IFD-1-positve puncta per ALM do not significantly differ in strains expressing *bzIs166*[P_{mec-4} mCherry]; *bzSi3*[P_{mec-7} GFP::IFD-1], with or without *ifd-2(bz187)*. P = NS, N > 37, 3 trials, two-tailed t-test, error bars are SEM. Juxtanuclear location assessed in a binary manner.

C) **IFD-1-positive puncta number per ALM neuron remains the same in control and *ifd-2(bz187).*** Number of IFD-1-positive inclusions in Ad2 ALM somas does not change in mutant *ifd-2(bz187)* versus WT in strains expressing *bzIs166*[P_{mec-4} mCherry]; *bzSi3*[P_{mec-7} GFP::IFD-1]. NS, N > 39, 3 trials, two-tailed t-test, error bars are SEM.

New Supplementary Figure 8. Expression of GFP-tagged *ifd-1* and *ifd-2* from their native promoters and with in-line endogenous tags show visibly express in *C. elegans* gut.

Transgenic tag IFDs expressed from the native promoter show visible expression in *C. elegans* gut.

A) *bzEx419*[P_{ifd-1}GFP::IFD-1] is not visible in ALM touch neurons. Merge of GFP, mCherry, and DIC channel - same image view as in left, but different stack of the animal. mCherry-tagged neuron is out of the focal plane. Images are representative of N > 10. Scale bar = 2 µm.

B) *bzEx418*[P_{ifd-2}GFP::IFD-2] is not visible in ALM touch neurons. Merge of GFP, mCherry, and DIC channel - same image view as in left, but different stack of the animal. mCherry-tagged neuron is out of the focal plane. Images are representative of N > 10. Scale bar = 2 µm.

In-line endogenous tag of IFDs show visible expression in *C. elegans* gut.

C) N-terminal endogenous GFP tag (*syb5616*) on *ifd-1* crossed with touch neuron marker, *bzIs166*[P_{mec-4}mCherry]. Merge of GFP, mCherry, and DIC channel – same animal, different z-stack. mCherry-tagged neuron is out of the focal plane. GFP is not visible in ALM touch neurons. Images are representative of N > 10. Scale bar = 2 µm.

D) N-terminal endogenous GFP tag (*bz477*) on *ifd-1* crossed with touch neuron marker, *bzIs166*[P_{mec-4}mCherry]. Merge of GFP, mCherry, and DIC channel – same animal, different z-stack. mCherry-tagged neuron is out of the focal plane. GFP is not visible in ALM touch neurons. Images are representative of N > 10. Scale bar = 2 µm.

New Supplementary Figure 9. Intestine-specific *ifd-2* expression does not rescue *ifd-2(Δ)* defects in exopher production. *ifd-2* is expressed in intestine and can influence intestinal morphology[92], raising the question as to whether the intestine might signal non-autonomously to impact exopher production. We therefore expressed *ifd-2* from the *vha-6* intestine-specific promoter in the *ifd-2(Δ)*; mCherry background and scored exopher levels. We compared ALMR exophers at Ad2 in *bzIs166*[P_{mec-4}mCherry] compared to *bzIs166*[P_{mec-4}mCherry]; *ifd-2(bz187)* (P=0.0053); *bzIs166*[P_{mec-4}mCherry] compared to *bzIs166*[P_{mec-4}mCherry]; *ifd-2(bz187); bzSi45*[P_{vha-6}mSc::IFD-2] (P = 0.29). *bzIs166*[P_{mec-4}mCherry]; *ifd-2(bz187)* compared to *bzIs166*[P_{mec-4}mCherry]; *ifd-2(bz187); bzSi45*[P_{vha-6}mSc::IFD-2] is P = 0.07, N > 130, 5 trials.

New Supplementary Figure 10. IFD-1 compartments are enlarged under neuronal stress conditions

Our previous work showed that exopher levels are high in early adult life (Ad1-Ad3) and then reach a low baseline for much of adult life that follows. Disruption of autophagy genes *bec-1, atg-7, lgg-1/-2* or exposure to autophagy inhibitor Spautin and/or proteasome inhibitor MG132 elevates exophers, consistent with the idea that exophers are generated under enhanced neuronal proteostress [4], unpublished observations on MG132 single agent.

A) Number of IFD-1 inclusions per ALM neuron with increasing age. Strain: ZB4632 *bzIs166*[P_{mec-4}mCherry]; *bzSi3*[P_{mec-7}GFP::IFD-1]. Life-stage points assayed: L4, Ad1, Ad2, Ad3, Ad4, Ad6, Ad10, Ad11, Ad12, Ad14. N = 25, 19, 34, 28, 30, 25, 9, 13, 12 for lifestages respectively. One-way *anova*, Dunnet's post-test, error bars are SEM. Note that the period of highest IFD-1 inclusion load coincides with that of the early adult peak in exophergenesis we previously reported[4].

B) IFD-1-positive inclusions increase in size with age. GFP::IFD-1 diameter in ALM neurons in µm. Strain: ZB4632 *bzIs166*[P_{mec-4}mCherry];*bzSi3*[P_{mec-7}GFP::IFD-1]**.** Life-stage points assayed: L4, Ad1, Ad2, Ad3, Ad4, Ad6, Ad10, Ad11, Ad12, Ad14. N = 25, 19, 34, 28, 30, 25, 9, 13, 12 for life stages, respectively. Error bars are SEM. Note that exopher levels are high during early adult life but then return to baseline for much of adult life; we observe a second peak in exopher production later in life that is much more variable in occurrence and specific time of onset [4]. The size of the IF foci does not always correlate to extrusion level, especially later in life.

C) IFD-1-positive inclusions increase in average size under enhanced proteostress induced by mCherry expression. GFP::IFD-1 diameter in ALM neurons in µm on Ad2. Strain ZB4998 *bzSi3*[P_{mec-7}GFP::IFD-1], ZB4632 *bzIs166*[P_{mec-4}mCherry]; *bzSi3*[P_{mec-7}GFP::IFD-1]**.** $P > 0.005$, N > 50/strain, 3 trials, two-tailed t-test, error bars are SEM. *bzIs166*[P_{mec-4}mCherry] produces a high level of mCherry in touch neurons and elevates exopher production and thus is considered a proteostress.

D) IFD-1-positive inclusions increase in size under enhanced proteostress induced by proteasome and autophagy inhibitors. We treated strain ZB4632 *bzIs166*[P_{mec-4}mCherry]; *bzSi3*[P_{mec-7}GFP::IFD-1] with both 10 mM proteasome inhibitor MG132 and 10 mM autophagy inhibitor Spautin-1, proteostresses that are known to enhance exopher production, from L4 to Ad3 and measured GFP::IFD-1 inclusion size at Ad3. GFP::IFD-1 diameter in ALM neurons in µm. $P < 0.05$, N > 50/strain, 3 trials, two-tailed t-test, error bars are SEM. $P < 0.05$, *. $P < 0.005$, **. $P < 0.0005$, ***.

E) *epg-9/ATG101* mutant significantly increases percentage of ALMR exopher production on Ad2. EPG-9 works with the UNC-51 complex to regulate induction of autophagy and is essential for autophagy function [94]. Strain: ZB4993 *epg-9(bp320)III*; *bzIs166*[P_{mec-4}mCherry]; *bzSi3*[P_{mec-7}GFP::IFD-1], ZB4632 *bzIs166*[P_{mec-4}mCherry]; *bzSi3*[P_{mec-7}GFP::IFD-1]. $P < 0.0005$, N > 83 / strain, 3 trials, error bars are SEM. Cochran-Mantel-Haenszel test, error bars are SEM.

F) IFD-1-positive puncta number per cell increases in *epg-9/ATG101* mutant. Strain: ZB4993 *epg-9(bp320)*III; *bzIs166*[P_{mec-4}mCherry]; *bzSi3*[P_{mec-7}GFP::IFD-1], ZB4632 *bzIs166*[P_{mec-4}mCherry]; *bzSi3*[P_{mec-7}GFP::IFD-1]. $P = 0.07$, N > 30/strain, 3 trials, two-tailed t-test, error bars are SEM.

G) Maximum IFD-1-positive puncta size increases in *epg-9/ATG101* mutant. Strain: ZB4993 *epg-9(bp320)III*; *bzIs166*[P_{mec-4}mCherry]; *bzSi3*[P_{mec-7}GFP::IFD-1], ZB4632 *bzIs166*[P_{mec-4}mCherry]; *bzSi3*[P_{mec-7}GFP::IFD-1]. Maximum GFP::IFD-1 punctae diameter per ALM, in µm. $P < 0.005$, $N > 30$/strain, 3 trials, two-tailed t-test, error bars are SEM.

Supplementary Figure 11. Multiple IFD-1 and IFD-2 fluorescently-tagged reporter proteins display similar localization

Adult ALM soma outlined with continuous line, nucleus outlined with dotted-line. Scale bar = 2 µm. Images representative of $N > 10$.

A) ZB5021 *bzSi34*[P_{mec-7}mSc::IFD-1]
B) ZB4998 *bzSi3*[P_{mec-7}GFP::IFD-1]
C) ZB5091 *bzSi37*[P_{mec-7}mNG::IFD-2]; *bzIs166*[P_{mec-4}mCherry]
D) ZB4866 *bzEx253*[P_{mec-7}RFP::IFD-2]; *zdIs5*[P_{mec-4}GFP]

Supplementary Figure 12. Transgenic IF tags are neither dominant negative for exopher production nor exopher-elevating on their own.

A) Single copy *bzIs3*[P_{mec-7}GFP::IFD-1] does not affect Ad2 ALMR exopher levels. $P = 0.92$, $N > 571$/strain, 10 trials, Cochran-Mantel-Haenszel test, error bars are SEM. Strains: control ZB4065 *bzIs166*[P_{mec-4}mCherry] and ZB4632 *bzIs166*[P_{mec-4}mCherry];*bzSi3*[P_{mec-7}GFP::IFD-1].

B) Single copy *bzIs37*[P_{mec-7}mNG::IFD-2] does not affect Ad2 ALMR exopher percentage. $P = 0.75$, $N > 100$, 3 trials, Cochran-Mantel-Haenszel test, error bars are SEM. Strains: control ZB4065 *bzIs166*[P_{mec-4}mCherry] and ZB5091 *bzIs166*[P_{mec-4}mCherry];*bzSi37*[P_{mec-7}mNeonGreen::IFD-2].

C) Over expressed GFP::IFD-1 array does not affect Ad2 ALMR exopher percentage. $P = 0.0904$, $N > 208$, 7 trials, Cochran-Mantel-Haenszel test, error bars are SEM. Strains: control ZB4065 *bzIs166*[P_{mec-4}mCherry] and ZB4501 *bzIs166*[P_{mec-4}mCherry];*bzEx270*[P_{mec-7}GFP::IFD-1].

D) Over expressed RFP::IFD-2 array does not affect Ad2 ALMR exopher percentage. $P = 0.987$, $N > 425$, 11 trials, Cochran-Mantel-Haenszel test, error

bars are SEM. Strains: control ZB4065 *bzIs166*[P_{mec-4}mCherry] and ZB4792 *bzIs166*[P_{mec-4}mCherry];*bzEx253*[P_{mec-7}RFP::IFD-2].

Supplementary Figure 13. IFD puncta measures under conditions of microtubules or dynein-mediated transport disruption.

A) **Microtubule inhibition via colchicine treatment from L4 to Ad2 reduces ALM IFD-1 puncta size**. Strain is ZB4632 *bzIs166*[P_{mec-4}mCherry]; *bzSi3*[P_{mec-7}GFP::IFD-1]; diameter of IFD-1-positive organelle in ALM Ad2 in µm. Control DMSO, colchicine 5 mM L4 to Ad2 exposure. $P < 0.0005$, $N > 99$/strain, 3 trials, two-tailed t-test, error bars are SEM.

B) **Microtubule inhibition via colchicine treatment from L4 to Ad2 reduces the juxtanuclear location IFD-1 puncta.** Strain is ZB4632 *bzIs166*[P_{mec-4}mCherry]; *bzSi3*[P_{mec-7}GFP::IFD-1]; control DMSO, colchicine 5 mM L4 to Ad2 exposure. $P < 0.0005$, $N > 99$ / strain, 3 trials, two-tailed t-test, error bars are SEM.

C) **Cell-specific DHC-1 dynein knockdown via AID reduces ALM Ad2 IFD-1 puncta size.** Strains are ZB4871 *bzIs166*[P_{mec-4}mCherry]; *bzSi6*[P_{mec-7}TIR-1::TagBFP]; *bzSi3*[P_{mec-7}GFP::IFD-1]; *dhc-1*(*ie28*[DHC-1::degron::GFP]) and ZB4872 *bzIs166*[P_{mec-4}mCherry]; *bzSi3*[P_{mec-7}GFP::IFD-1]; *dhc-1*(*ie28*[DHC-1::degron::GFP]). Diameter of IFD-1-positive organelle in ALM Ad2 is measured in µm. Control is -/- for P_{mec-7}TIR-1, *dhc-1* knockdown strain is +/+ for P_{mec-7}TIR-1. Both strains were exposed to 5 mM auxin from L4 to Ad2. $P < 0.005$, $N > 86$ / strain, 3 trials, two-tailed t-test, error bars are SEM.

D) **Cell-specific DHC-1 dynein knockdown via AID reduces the juxtanuclear location of Ad2 ALM IFD-1 puncta.** Strains are ZB4871 *bzIs166*[P_{mec-4}mCherry]; *bzSi6*[P_{mec-7}TIR-1::TagBFP]; *bzSi3*[P_{mec-7}GFP::IFD-1]; *dhc-1*(*ie28*[DHC-1::degron::GFP]) and ZB4872 *bzIs166*[P_{mec-4}mCherry]; *bzSi3*[P_{mec-7}GFP::IFD-1]; *dhc-1*(*ie28*[DHC-1::degron::GFP]). Control strains is -/- for P_{mec-7}TIR-1, *dhc-1* knockdown strain is +/+ for P_{mec-7}TIR-1. Both strains were exposed to 5 mM auxin from L4 to Ad2. $P < 0.005$, $N > 30$ / strain, 3 trials, two-tailed t-test, error bars are SEM.

Supplementary Figure 14: Highly expressed HttQ128::CFP and mScarlet::IFD-1 can present variable colocalization.

Localization patterns of HttQ128::CFP and IFD-1 interaction.
In this strain, HttQ128::CFP is expressed from a high-copy-number integrated transgene array. Expression is higher than in the single-copyHttQ74 strain. In this case, we note that the IFD compartment often does not appear to fully surround the HttQ128 signal. Biophysical analyses support heterogeneity in aggregate properties *in vivo* in polyQ touch neurons [49]. **Top row**: Adult touch neuron soma displaying the three main patterns of interaction shown when expressing mScarlet::IFD-1 and HttQ128::CFP. 1) HttQ128::CFP signal fully encompasses IFD signal, with globular expansion from the IFD core. 2) HttQ128 and IFD display a bi-lobed globular interaction, where part of the bi-lobed structure has overlap. 3) HttQ128 and IFD overlap entirely (white arrows). Scale bar = 2 µm. **Bottom row:** side view z-stack (0.2 µm) for images in the top row. Scale bar = 2 µm. Strain: ZB5104 *igIs1*[P_{mec-7} YFP, P_{mec-3} htt57Q128::CFP, *lin-15(+)*]; *bzSi34*[P_{mec-7} mScarlet::IFD-1].

Supplementary Figure 15. Overexpressed mCherry is predominantly housed in LMP-1-bound lysosomal-organelles, which are distinct from the IF-compartment.

A) **IFD-positive organelles are often localized next to, but not overlapped with, a subset of mCherry concentrations when tagged IFD is expressed from a single copy transgene**. Representative Ad2 touch neuron, representative of N > 50. Strain ZB4632 *bzIs166[*P_{mec-4}mCherry]*; bzSi3*[P_{mec-7}GFP::IFD-1]. Scale bar = 2 µm

B) **mCherry is mostly in LMP-1-bound structures.** A representative adult ALM neuron (white solid outline) expressing the LMP-1::GFP lysosome marker. Representative of N > 250. LMP-1::GFP signal is enriched in the lysosome membrane forming a GFP ring (pseudo-colored blue) around the mCherry collection. mCherry degradation appears minimal within the LMP-1::GFP compartment as signal persists. GFP channel is pseudo-colored to blue to emphasize reporter difference in panel A. Strain ZB4509 *bzIs166[*P_{mec-4}mCherry]*; bzIs168*[P_{mec-7}LMP-1::GFP].

White dashed line outlines the nucleus. Scale bar = 2 µm.

Supplementary Figure 16. IFD-HttQ74-positive organelles can be exopher cargo. HttQ74 aggregates frequently exit the cell, with concentrated HttQ74 foci colocalized with the IFD+ structure ~ 50% of the time.

A) **IFD-1-positive puncta extruded in an HttQ74-enriched exopher.** Shown is an adult touch neuron from strain ZB5171 *bzSi39*[P_{mec7} HttQ74::mNG]; *bzSi34*[P_{mec-7}mScarlet::IFD-1] on Ad1 after a 6 hour fast. Soma outline white, nucleus white dash; arrowhead points to the concentrated HttQ74 punctum that co-localizes to the IFD-1 domain or HttQ74::mNG-mSc::IFD-1 puncta. Scale bar = 2 µm, N > 10. Note that in this image much of the cytosolic mNG::HttQ74 gets extruded into the exopher, but is concentrated in mSc::IFD-1-compartment.

B) **Top: IFD-1-positive organelles are included in 14/30 ALM exopher events.** We examined strain ZB5171 *bzSi39*[P_{mec7}HttQ74::mNG]; *bzSi34*[P_{mec-7}mScarlet::IFD-1] on Ad1, after a 6 hour fast to increase exopher yields, and determined how often mScarlet::IFD-1 was extruded in exophers. We observed 30 ALM exopher events, with 14 having mSc::IFD-1 included in the exopher. **Bottom: Exophers that contain an IFD aggresome frequently colocalize with mNG::HttQ74 aggregates.** We determined how often the 14 mScarlet::IFD-1-positive exopher events also included at least one event of concentrated HttQ74 puncta overlapping with mSc::IFD-1. In 11 ALM IFD-1-positive exophers there was at least mNG::HttQ74 punctum colocalized with mSc::IFD-1.

C) **Top: HttQ74-aggregates are included in 22/30 ALM exopher events.** We examined the same strain and the same exopher events as in A. ZB5171 *bzSi39*[P_{mec7}HttQ74::mNG]; *bzSi34*[P_{mec-7}mScarlet::IFD-1] on Ad1, after a 6 hour fast to increase exopher yields. We determined how often HttQ74 aggregates were extruded in exophers. Out of N = 30 ALM exopher events, 22 exopher events had at least one HttQ74 aggregate included in the exopher. **Bottom: Ejected HttQ74 aggregates can colocalize with IFD.** We determined how often mNG::HttQ74 positive exopher events (N = 22) included species where HttQ74 is a cargo of the mSc-aggresome. 50% of ALM HttQ74-positive exophers had at least one incidence of HttQ74 including mSc::IFD-1.

Supplementary Figure 17. Assessing *hda-6* and *sqst-1* impact on IFD compartments and exopher production

A) ***hda-6(ok3203)* does not significantly affect IFD-1 puncta number per cell in the *bzIs166*[P_{mec-4}mCherry] background.** Strain is ZB4801 *bzIs166*[P_{mec-}

$_{4}$mCherry]; *hda-6(ok3203); bzSi3*[P$_{mec-7}$GFP::IFD-1], ZB4632 *bzIs166*[P$_{mec-4}$mCherry]; *bzSi3*[P$_{mec-7}$GFP::IFD-1]. HDA-6 is an ortholog of human HDAC6, a cytoplasmic deacetylase with conserved function as an adapter, microtubule modulator, and autophagy regulator. Number of IFD-1 puncta in ALM Ad2, N > 60, 4 trials, two-tailed t-test, NS, error bars are SEM.

B) *hda-6(ok3203)* does not affect IFD-1 puncta size in *bzIs166*[P$_{mec-4}$mCherry] background. Strains are ZB4801 *bzIs166*[P$_{mec-4}$mCherry]; *hda-6(ok3203), bzSi3*[P$_{mec-7}$GFP::IFD-1], ZB4632 *bzIs166*[P$_{mec-4}$mCherry]; *bzSi3*[P$_{mec-7}$GFP::IFD-1]. Diameter of IFD-1 puncta measured in ALM Ad2 in µm. N > 60, 4 trials, two-tailed t-test, error bars are SEM.

C) *hda-6(ok3203)* increases exophergenesis in the *bzIs166*[P$_{mec-4}$mCherry] background on Ad2. Strains are ZB4801 *bzIs166*[P$_{mec-4}$mCherry]; *hda-6(ok3203), bzSi3*[P$_{mec-7}$GFP::IFD-1], ZB4632 *bzIs166*[P$_{mec-4}$mCherry]; *bzSi3*[P$_{mec-7}$GFP::IFD-1]. P > 0.0005, N > 150, 8 trials. Cochran-Mantel-Haenszel test, error bars are SEM.

D) IFD-1 puncta size decreases in *sqst-1*(*ok2892*). *sqst-1* encodes the ortholog of human SQSM1, an aggregate adapter protein implicated in mammalian aggresome formation and autophagy. Strains are ZB4632 *bzIs166*[P$_{mec-4}$mCherry]; *bzSi3*[P$_{mec-7}$GFP::IFD-1], ZB4838 *bzIs166*[P$_{mec-4}$mCherry]; *T12G3.1*(*ok2892*) IV; *bzSi3*[P$_{mec-7}$GFP::IFD-1]. Diameter of IFD-1 puncta in ALM Ad2 in µm. P < 0.05, N > 25, 3 trials, two-tailed t-test, error bars are SEM.

E) IFD-1 puncta number per ALM increases in *sqst-1*(*ok2892*). Strains are ZB4632 *bzIs166*[P$_{mec-4}$mCherry];*bzSi3*[P$_{mec-7}$GFP::IFD-1], ZB4838 *bzIs166*[P$_{mec-4}$mCherry]; *T12G3.1(ok2892)IV*; *bzSi3*[P$_{mec-7}$GFP::IFD-1]. Number of IFD-1 puncta per Ad2 ALM indicated. P < 0.005, N > 25, 3 trials, two-tailed t-test, error bars are SEM.

F) *sqst-1*(*ok2892*) impacts variation in exophergenesis without significantly changing outcome in the *bzIs166*[P$_{mec-4}$mCherry] background. Strains are ZB4065 *bzIs166*[P$_{mec-4}$mCherry], ZB4991 *bzIs166*[P$_{mec-4}$mCherry]; *sqst-1*(*ok2892*). We scored ALMR exophers at Ad2 in *bzIs101*[P$_{mec-4}$mCherry] compared to *bzIs101*[P$_{mec-4}$mCherry]; *sqst-1(ok2892)*. NS, N > 250, 9 trials. Cochran-Mantel-Haenszel, error bars are SEM.

G) SQST-1 localizes to the IFD-1 puncta. Representative of adult touch neuron expressing *bpIs151*[P_{sqst-1}SQST-1::GFP + *unc-76*(+)]; *bzEx261*[P_{mec-7}RFP::IFD-2]. Representative of N > 10. Scale bar = 2 µm.

Supplementary Figure 18. Human homolog Neurofilament Light Chain (hNFL) can adopt multiple localization patterns in *C. elegans* touch neurons, but prominently localizes to 1 or 2 juxtanuclear inclusions.

A-D) Human hNFL can adopt multiple localization patterns when expressed in the *C. elegans* touch neurons – A) filamentous/cytoplasmic (Strain: ZB5345 *bzEx311*[P_{mec-7}mNG::hNFL];*bzIs166*[P_{mec-4}mCherry]; *ifd-2(bz187)* **B)** axonal (and punctate featured.) **C)** nuclear (and punctate featured) and D) most commonly, juxtanuclear and punctate. Scale bar = 2 µm. **B-D:** Strain: ZB5175 *bzEx269*[P_{mec-7}mNG::hNFL];*bzSi34*[P_{mec-7}mSc::IFD-1].

E-K) Human mNG::hNFL forms juxtanuclear inclusions in either single copy or high copy array lines. E- Top - filamentous/ cytosolic localization (rare). Bottom – punctate/collected localization. Strain: ZB5593 *bzIs166*[P_{mec-4}mCherry];*bzEx311*[P_{mec-7}mNG::hNFL].

Top quantification **(F, G, H) –** of integrated single copy strain ZB5332 *bzSi48*[P_{mec-7} mNG::hNFL]; *bzIs166*[P_{mec-4}mCherry]. Bottom quantification **(I, J, K)** of high copy array quantification of strain ZB5593 *bzIs166*[P_{mec-4}mCherry];*bzEx311*[P_{mec-7}mNG::hNFL].Collected or cytosolic localization phenotype quantified in **F** and **I**. Juxtanuclear location quantified in **G** and **J**. Number of collected punctate quantified in **H** and **K**. Scale bar = 2 *µm*. Representative of N > 10.

Supplementary Figure 19. Transgenic hNFL tags are neither dominant negative for exopher production nor exopher-elevating on their own.

A) Single copy mNG::hNFL does not affect Ad2 ALMR exopher percentage. P = 0.442, N > 94, 3 trials, Cochran-Mantel-Haenszel test, error bars are SEM. Strains: control ZB4065 *bzIs166*[P_{mec-4}mCherry] and ZB5332 *bzIs166*[P_{mec-4}mCherry];*bzSi48*[P_{mec-7}mNG::hNFL].

B) Over expressed mNG::hNFL array does not affect Ad2 ALMR exopher percentage. P = 0.052, N > 60, 3 trials, Cochran-Mantel-Haenszel test, error bars are SEM. Strains: control ZB4065 *bzIs166*[P_{mec-4}mCherry] and ZB5593 *bzIs166*[P_{mec-4}mCherry];*bzEx311*[P_{mec-7}mNG::hNFL].

1. López-Otín, C., et al., *The hallmarks of aging.* Cell, 2013. **153**(6): p. 1194-217.
2. Davis, A.A., C.E.G. Leyns, and D.M. Holtzman, *Intercellular Spread of Protein Aggregates in Neurodegenerative Disease.* Annu Rev Cell Dev Biol, 2018. **34**: p. 545-568.
3. Hipp, M.S., P. Kasturi, and F.U. Hartl, *The proteostasis network and its decline in ageing.* Nat Rev Mol Cell Biol, 2019. **20**(7): p. 421-435.

4. Melentijevic, I., et al., *C. elegans neurons jettison protein aggregates and mitochondria under neurotoxic stress.* Nature, 2017. **542**(7641): p. 367-371.
5. Arnold, M.L., et al., *Quantitative Approaches for Scoring in vivo Neuronal Aggregate and Organelle Extrusion in Large Exopher Vesicles in C. elegans.* J Vis Exp, 2020(163).
6. Donnelly, K.M., et al., *Phagocytic glia are obligatory intermediates in transmission of mutant huntingtin aggregates across neuronal synapses.* Elife, 2020. **9**.
7. Ray, A., S.D. Speese, and M.A. Logan, *Glial Draper Rescues Aβ Toxicity in a Drosophila Model of Alzheimer's Disease.* J Neurosci, 2017. **37**(49): p. 11881-11893.
8. Johnston, J.A., C.L. Ward, and R.R. Kopito, *Aggresomes: a cellular response to misfolded proteins.* J Cell Biol, 1998. **143**(7): p. 1883-98.
9. Garcia-Mata, R., Y.S. Gao, and E. Sztul, *Hassles with taking out the garbage: aggravating aggresomes.* Traffic, 2002. **3**(6): p. 388-96.
10. Kopito, R.R., *Aggresomes, inclusion bodies and protein aggregation.* Trends Cell Biol, 2000. **10**(12): p. 524-30.
11. Cooper, J.F., et al., *Stress increases in exopher-mediated neuronal extrusion require lipid biosynthesis, FGF, and EGF RAS/MAPK signaling.* Proc Natl Acad Sci U S A, 2021. **118**(36).
12. Turek, M., et al., *Muscle-derived exophers promote reproductive fitness.* EMBO Rep, 2021. **22**(8): p. e52071.
13. Gamerdinger, M., et al., *BAG3 mediates chaperone-based aggresome-targeting and selective autophagy of misfolded proteins.* EMBO Rep, 2011. **12**(2): p. 149-56.
14. García-Mata, R., et al., *Characterization and dynamics of aggresome formation by a cytosolic GFP-chimera.* J Cell Biol, 1999. **146**(6): p. 1239-54.
15. Gautreau, A., et al., *Isolation and characterization of an aggresome determinant in the NF2 tumor suppressor.* J Biol Chem, 2003. **278**(8): p. 6235-42.
16. Herrmann, H. and U. Aebi, *Intermediate filaments: molecular structure, assembly mechanism, and integration into functionally distinct intracellular Scaffolds.* Annu Rev Biochem, 2004. **73**: p. 749-89.
17. Herrmann, H. and U. Aebi, *Intermediate Filaments: Structure and Assembly.* Cold Spring Harb Perspect Biol, 2016. **8**(11).
18. Helfand, B.T., et al., *A role for intermediate filaments in determining and maintaining the shape of nerve cells.* Mol Biol Cell, 2003. **14**(12): p. 5069-81.
19. Julien, J.P., *A role for neurofilaments in the pathogenesis of amyotrophic lateral sclerosis.* Biochem Cell Biol, 1995. **73**(9-10): p. 593-7.
20. Perrot, R. and J. Eyer, *Neuronal intermediate filaments and neurodegenerative disorders.* Brain Res Bull, 2009. **80**(4-5): p. 282-95.
21. Taylor, J.P., et al., *Aggresomes protect cells by enhancing the degradation of toxic polyglutamine-containing protein.* Hum Mol Genet, 2003. **12**(7): p. 749-57.
22. Spillantini, M.G., et al., *alpha-Synuclein in filamentous inclusions of Lewy bodies from Parkinson's disease and dementia with lewy bodies.* Proc Natl Acad Sci U S A, 1998. **95**(11): p. 6469-73.
23. Loeffler, T., et al., *Neurofilament-Light Chain as Biomarker of Neurodegenerative and Rare Diseases With High Translational Value.* Front Neurosci, 2020. **14**: p. 579.
24. Lockhead, D., et al., *The tubulin repertoire of C. elegans sensory neurons and its context-dependent role in process outgrowth.* Mol Biol Cell, 2016. **27**(23): p. 3717-28.

25. Kaletsky, R., et al., *The C. elegans adult neuronal IIS/FOXO transcriptome reveals adult phenotype regulators.* Nature, 2016. **529**(7584): p. 92-6.
26. Hammarlund, M., et al., *The CeNGEN Project: The Complete Gene Expression Map of an Entire Nervous System.* Neuron, 2018. **99**(3): p. 430-433.
27. Karabinos, A., *Intermediate filament (IF) proteins IFA-1 and IFB-1 represent a basic heteropolymeric IF cytoskeleton of nematodes: A molecular phylogeny of nematode IFs.* Gene, 2019. **692**: p. 44-53.
28. Kurup, N., et al., *Intermediate filament accumulation can stabilize microtubules in Caenorhabditis elegans motor neurons.* Proc Natl Acad Sci U S A, 2018. **115**(12): p. 3114-3119.
29. Carberry, K., et al., *Intermediate filaments in Caenorhabditis elegans.* Cell Motil Cytoskeleton, 2009. **66**(10): p. 852-64.
30. Geisler, F., et al., *Intestinal intermediate filament polypeptides in C. elegans: Common and isotype-specific contributions to intestinal ultrastructure and function.* Sci Rep, 2020. **10**(1): p. 3142.
31. Geisler, F., et al., *The intestinal intermediate filament network responds to and protects against microbial insults and toxins.* Development, 2019. **146**(2).
32. Leiers, B., et al., *A stress-responsive glutathione S-transferase confers resistance to oxidative stress in Caenorhabditis elegans.* Free Radic Biol Med, 2003. **34**(11): p. 1405-15.
33. Frøkjær-Jensen, C., et al., *Improved Mos1-mediated transgenesis in C. elegans.* Nat Methods, 2012. **9**(2): p. 117-8.
34. Sarov, M., et al., *A genome-scale resource for in vivo tag-based protein function exploration in C. elegans.* Cell, 2012. **150**(4): p. 855-66.
35. Lai, C.C., et al., *Sequence and transmembrane topology of MEC-4, an ion channel subunit required for mechanotransduction in Caenorhabditis elegans.* J Cell Biol, 1996. **133**(5): p. 1071-81.
36. Zhang, L., et al., *The auxin-inducible degradation (AID) system enables versatile conditional protein depletion in C. elegans.* Development, 2015. **142**(24): p. 4374-84.
37. Jia, B., Y. Wu, and Y. Zhou, *14-3-3 and aggresome formation: implications in neurodegenerative diseases.* Prion, 2014. **8**(2): p. 173-7.
38. Kawaguchi, Y., et al., *The deacetylase HDAC6 regulates aggresome formation and cell viability in response to misfolded protein stress.* Cell, 2003. **115**(6): p. 727-38.
39. Zhou, L., et al., *p62/sequestosome 1 regulates aggresome formation of pathogenic ataxin-3 with expanded polyglutamine.* Int J Mol Sci, 2014. **15**(9): p. 14997-5010.
40. Chalfie, M. and J.N. Thomson, *Structural and functional diversity in the neuronal microtubules of Caenorhabditis elegans.* J Cell Biol, 1982. **93**(1): p. 15-23.
41. Bounoutas, A., R. O'Hagan, and M. Chalfie, *The multipurpose 15-protofilament microtubules in C. elegans have specific roles in mechanosensation.* Curr Biol, 2009. **19**(16): p. 1362-7.
42. Matsumoto, G., et al., *N-Acyldopamine induces aggresome formation without proteasome inhibition and enhances protein aggregation via p62/SQSTM1 expression.* Sci Rep, 2018. **8**(1): p. 9585.
43. Xu, Z., et al., *14-3-3 protein targets misfolded chaperone-associated proteins to aggresomes.* J Cell Sci, 2013. **126**(Pt 18): p. 4173-86.

44. Kolodziejska, K.E., et al., *Regulation of inducible nitric oxide synthase by aggresome formation.* Proc Natl Acad Sci U S A, 2005. **102**(13): p. 4854-9.
45. Zaarur, N., et al., *Proteasome failure promotes positioning of lysosomes around the aggresome via local block of microtubule-dependent transport.* Mol Cell Biol, 2014. **34**(7): p. 1336-48.
46. Brignull, H.R., et al., *Polyglutamine proteins at the pathogenic threshold display neuron-specific aggregation in a pan-neuronal Caenorhabditis elegans model.* J Neurosci, 2006. **26**(29): p. 7597-606.
47. Parker, J.A., et al., *Expanded polyglutamines in Caenorhabditis elegans cause axonal abnormalities and severe dysfunction of PLM mechanosensory neurons without cell death.* Proc Natl Acad Sci U S A, 2001. **98**(23): p. 13318-23.
48. Narain, Y., et al., *A molecular investigation of true dominance in Huntington's disease.* J Med Genet, 1999. **36**(10): p. 739-46.
49. Fisher, R.S., et al., *An apparent core/shell architecture of polyQ aggregates in the aging Caenorhabditis elegans neuron.* Protein Sci, 2021. **30**(7): p. 1482-1486.
50. Lu, M., et al., *Live-cell super-resolution microscopy reveals a primary role for diffusion in polyglutamine-driven aggresome assembly.* J Biol Chem, 2019. **294**(1): p. 257-268.
51. Kostich, M., A. Fire, and D.M. Fambrough, *Identification and molecular-genetic characterization of a LAMP/CD68-like protein from Caenorhabditis elegans.* J Cell Sci, 2000. **113 (Pt 14)**: p. 2595-606.
52. Katayama, H., et al., *GFP-like proteins stably accumulate in lysosomes.* Cell Struct Funct, 2008. **33**(1): p. 1-12.
53. Yan, J., et al., *SQSTM1/p62 interacts with HDAC6 and regulates deacetylase activity.* PLoS One, 2013. **8**(9): p. e76016.
54. Calixto, A., et al., *Enhanced neuronal RNAi in C. elegans using SID-1.* Nat Methods, 2010. **7**(7): p. 554-9.
55. Mignot, C., et al., *Dynamics of mutated GFAP aggregates revealed by real-time imaging of an astrocyte model of Alexander disease.* Exp Cell Res, 2007. **313**(13): p. 2766-79.
56. Mayer, R.J., et al., *Intermediate filament-ubiquitin diseases: implications for cell sanitization.* Biochem Soc Symp, 1989. **55**: p. 193-201.
57. Nicolás-Ávila, J.A., et al., *A Network of Macrophages Supports Mitochondrial Homeostasis in the Heart.* Cell, 2020. **183**(1): p. 94-109.e23.
58. Nicolás-Ávila, J., M. Sánchez-Diaz, and A. Hidalgo, *Isolation of exophers from cardiomyocyte-reporter mouse strains by fluorescence-activated cell sorting.* STAR Protoc, 2021. **2**(1): p. 100286.
59. Siddique, I., et al., *Exophers are components of mammalian cell neurobiology in health and disease.* bioRxiv, 2021: p. 2021.12.06.471479.
60. Hengartner, M.O. and H.R. Horvitz, *C. elegans cell survival gene ced-9 encodes a functional homolog of the mammalian proto-oncogene bcl-2.* Cell, 1994. **76**(4): p. 665-76.
61. Lewczuk, P., et al., *Plasma neurofilament light as a potential biomarker of neurodegeneration in Alzheimer's disease.* Alzheimers Res Ther, 2018. **10**(1): p. 71.
62. Ashton, N.J., et al., *A multicentre validation study of the diagnostic value of plasma neurofilament light.* Nat Commun, 2021. **12**(1): p. 3400.
63. Redemann, S., et al., *Codon adaptation-based control of protein expression in C. elegans.* Nat Methods, 2011. **8**(3): p. 250-2.

64. Nicolás-Ávila, J.Á., M. Sánchez-Diaz, and A. Hidalgo *Isolation of exophers from cardiomyocyte-reporter mouse strains by fluorescence-activated cell sorting*. STAR protocols, 2021. **2**, 100286 DOI: 10.1016/j.xpro.2020.100286.
65. Choong, C.J., et al., *Alternative mitochondrial quality control mediated by extracellular release.* Autophagy, 2020: p. 1-13.
66. Davis, C.H., et al., *Transcellular degradation of axonal mitochondria.* Proc Natl Acad Sci U S A, 2014. **111**(26): p. 9633-8.
67. Nicolás-Ávila, J.A., et al., *Macrophages, Metabolism and Heterophagy in the Heart.* Circ Res, 2022. **130**(3): p. 418-431.
68. Johnston, H.E. and R.S. Samant, *Alternative systems for misfolded protein clearance: life beyond the proteasome.* Febs j, 2020.
69. Guthrie, C.R., G.D. Schellenberg, and B.C. Kraemer, *SUT-2 potentiates tau-induced neurotoxicity in Caenorhabditis elegans.* Hum Mol Genet, 2009. **18**(10): p. 1825-38.
70. Guthrie, C.R., et al., *MSUT2 is a determinant of susceptibility to tau neurotoxicity.* Hum Mol Genet, 2011. **20**(10): p. 1989-99.
71. Civelek, M., et al., *The polyphenol quercetin protects from glucotoxicity depending on the aggresome in Caenorhabditis elegans.* Eur J Nutr, 2020. **59**(2): p. 485-491.
72. Arnold, M.L., et al., *Q&A: Trash talk: disposal and remote degradation of neuronal garbage.* BMC Biol, 2018. **16**(1): p. 17.
73. Lemos, M. and N. Stefanova, *Histone Deacetylase 6 and the Disease Mechanisms of α-Synucleinopathies.* Front Synaptic Neurosci, 2020. **12**: p. 586453.
74. Lu, M., et al., *Expression-level dependent perturbation of cell proteostasis and nuclear morphology by aggregation-prone polyglutamine proteins.* Biotechnol Bioeng, 2015. **112**(9): p. 1883-92.
75. Erpapazoglou, Z., O. Walker, and R. Haguenauer-Tsapis, *Versatile roles of k63-linked ubiquitin chains in trafficking.* Cells, 2014. **3**(4): p. 1027-88.
76. Hao, R., et al., *Proteasomes activate aggresome disassembly and clearance by producing unanchored ubiquitin chains.* Mol Cell, 2013. **51**(6): p. 819-28.
77. Morrow, C.S., et al., *Vimentin Coordinates Protein Turnover at the Aggresome during Neural Stem Cell Quiescence Exit.* Cell Stem Cell, 2020. **26**(4): p. 558-568.e9.
78. Lee, Y., et al., *Neurofilament Proteins as Prognostic Biomarkers in Neurological Disorders.* Curr Pharm Des, 2020. **25**(43): p. 4560-4569.
79. Bacioglu, M., et al., *Neurofilament Light Chain in Blood and CSF as Marker of Disease Progression in Mouse Models and in Neurodegenerative Diseases.* Neuron, 2016. **91**(1): p. 56-66.
80. Gordon, B.A., *Neurofilaments in disease: what do we know?* Curr Opin Neurobiol, 2020. **61**: p. 105-115.
81. Gentil, B.J., M. Tibshirani, and H.D. Durham, *Neurofilament dynamics and involvement in neurological disorders.* Cell Tissue Res, 2015. **360**(3): p. 609-20.
82. Lépinoux-Chambaud, C. and J. Eyer, *Review on intermediate filaments of the nervous system and their pathological alterations.* Histochem Cell Biol, 2013. **140**(1): p. 13-22.
83. Goldman, J.E., et al., *Lewy bodies of Parkinson's disease contain neurofilament antigens.* Science, 1983. **221**(4615): p. 1082-4.
84. Aljohani, M.D., et al., *Engineering rules that minimize germline silencing of transgenes in simple extrachromosomal arrays in C. elegans.* Nat Commun, 2020. **11**(1): p. 6300.

85. Grishok, A., J.L. Sinskey, and P.A. Sharp, *Transcriptional silencing of a transgene by RNAi in the soma of C. elegans.* Genes Dev, 2005. **19**(6): p. 683-96.
86. Meriin, A.B., et al., *Hsp70-Bag3 complex is a hub for proteotoxicity-induced signaling that controls protein aggregation.* Proc Natl Acad Sci U S A, 2018. **115**(30): p. E7043-e7052.
87. Jones, D., et al., *A portable regulatory element directs specific expression of the Caenorhabditis elegans ubiquitin gene ubq-2 in the somatic gonad.* Dev Biol, 1995. **171**(1): p. 60-72.
88. Sampuda, K.M., M. Riley, and L. Boyd, *Stress induced nuclear granules form in response to accumulation of misfolded proteins in Caenorhabditis elegans.* BMC Cell Biol, 2017. **18**(1): p. 18.
89. Bakowski, M.A., et al., *Ubiquitin-mediated response to microsporidia and virus infection in C. elegans.* PLoS Pathog, 2014. **10**(6): p. e1004200.
90. Aristizábal-Corrales, D., et al., *The 14-3-3 gene par-5 is required for germline development and DNA damage response in Caenorhabditis elegans.* J Cell Sci, 2012. **125**(Pt 7): p. 1716-26.
91. Gamerdinger, M., S. Carra, and C. Behl, *Emerging roles of molecular chaperones and co-chaperones in selective autophagy: focus on BAG proteins.* J Mol Med (Berl), 2011. **89**(12): p. 1175-82.
92. Geisler, F., et al., *Intestinal intermediate filament polypeptides in C. elegans: Common and isotype-specific contributions to intestinal ultrastructure and function.* Scientific Reports, 2020. **10**(1): p. 3142.
93. Toth, M.L., et al., *Neurite sprouting and synapse deterioration in the aging Caenorhabditis elegans nervous system.* J Neurosci, 2012. **32**(26): p. 8778-90.
94. Liang, Q., et al., *The C. elegans ATG101 homolog EPG-9 directly interacts with EPG-1/Atg13 and is essential for autophagy.* Autophagy, 2012. **8**(10): p. 1426-33.
95. Lu, Q., et al., *The WD40 repeat PtdIns(3)P-binding protein EPG-6 regulates progression of omegasomes to autophagosomes.* Dev Cell, 2011. **21**(2): p. 343-57.

Intermediate Filaments Associate with Aggresome-like Structures and Influence Rate of Cellular Expulsion of Neuronal Disease Aggregates

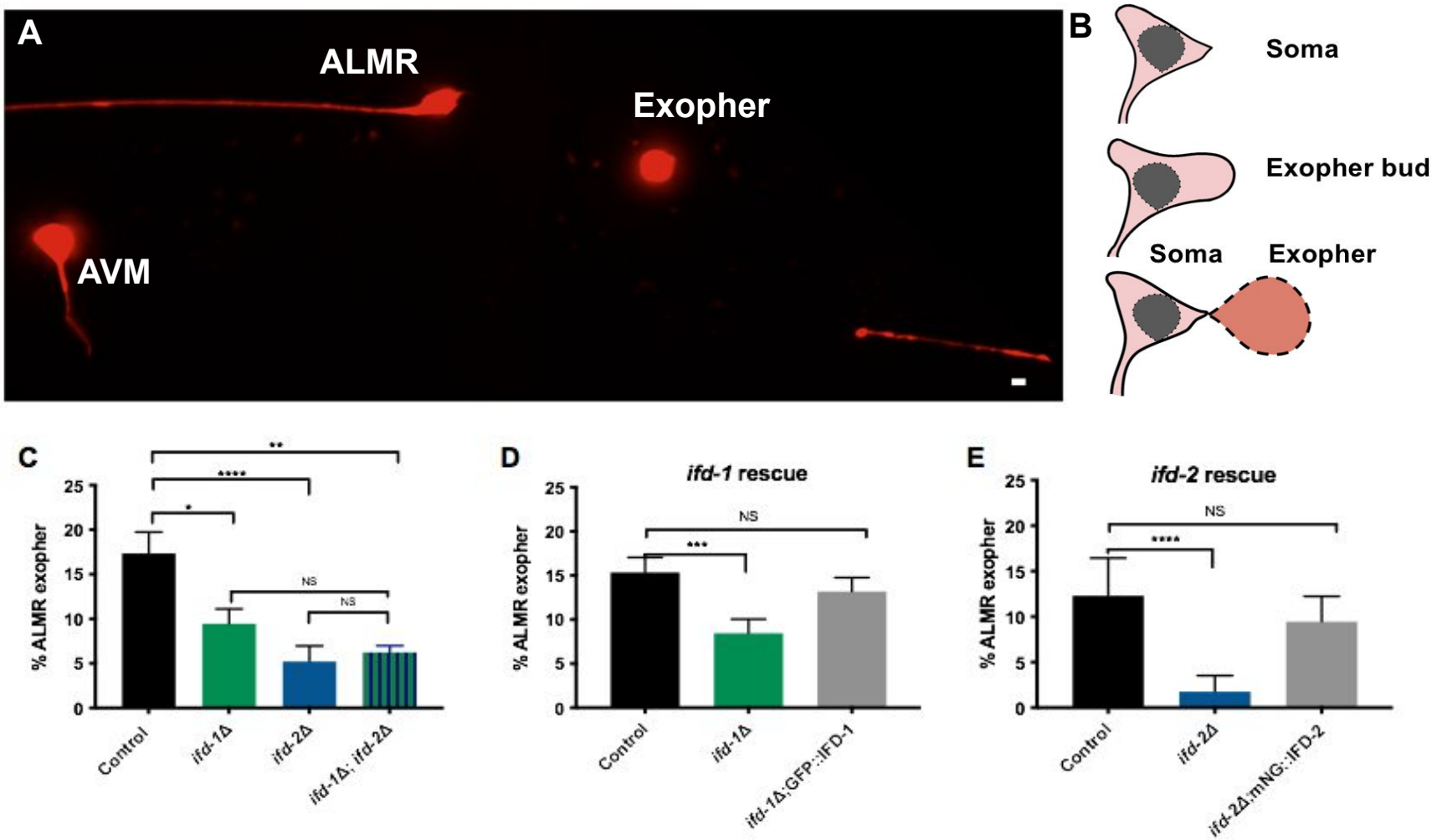

Arnold *et al.*, Figure 1

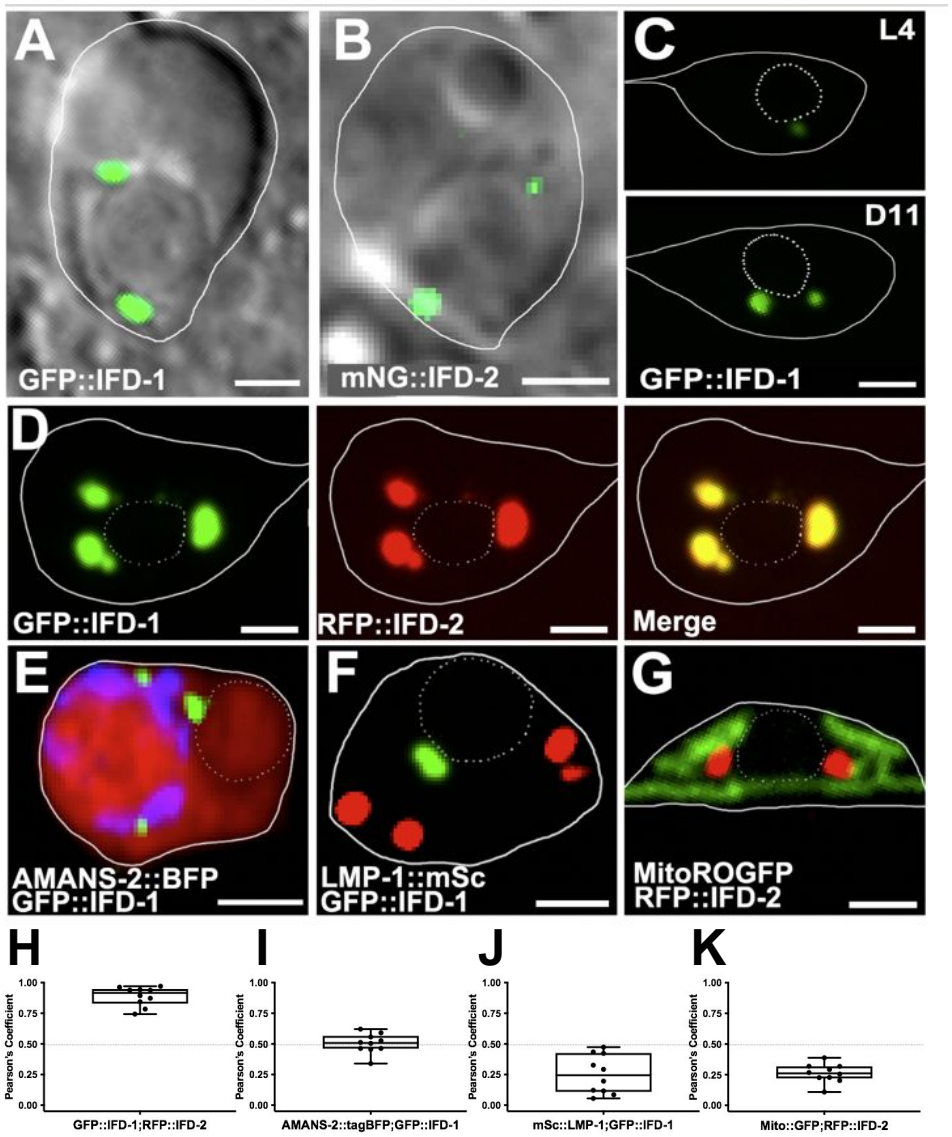

Arnold *et al.*, Figure 2

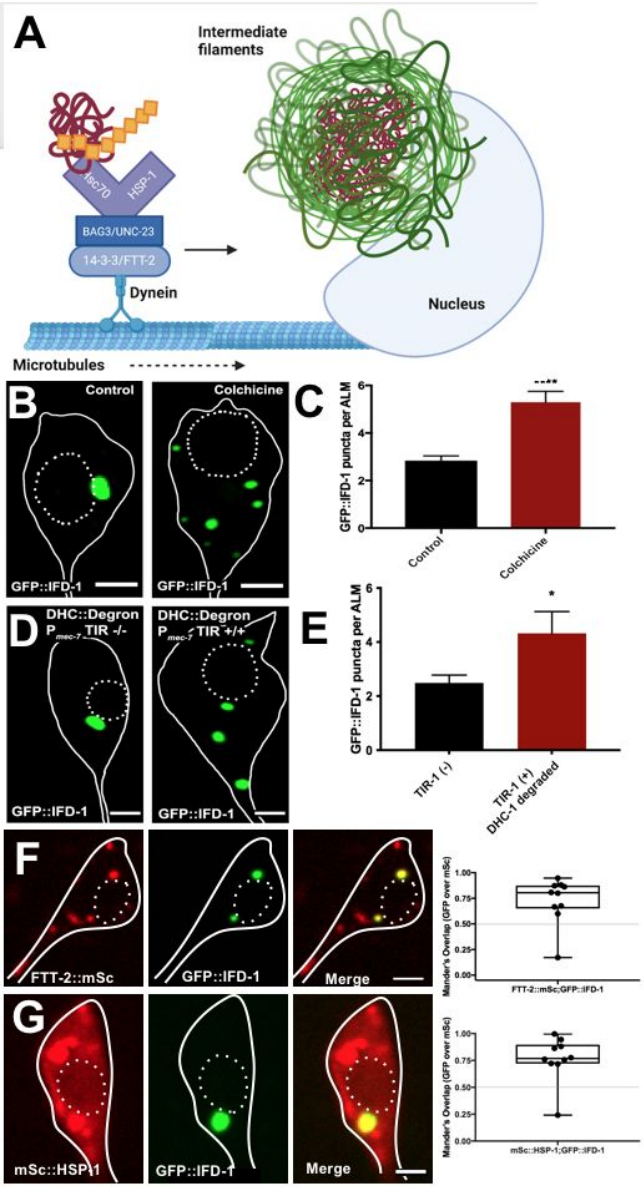

Arnold *et al.*, Figure 3

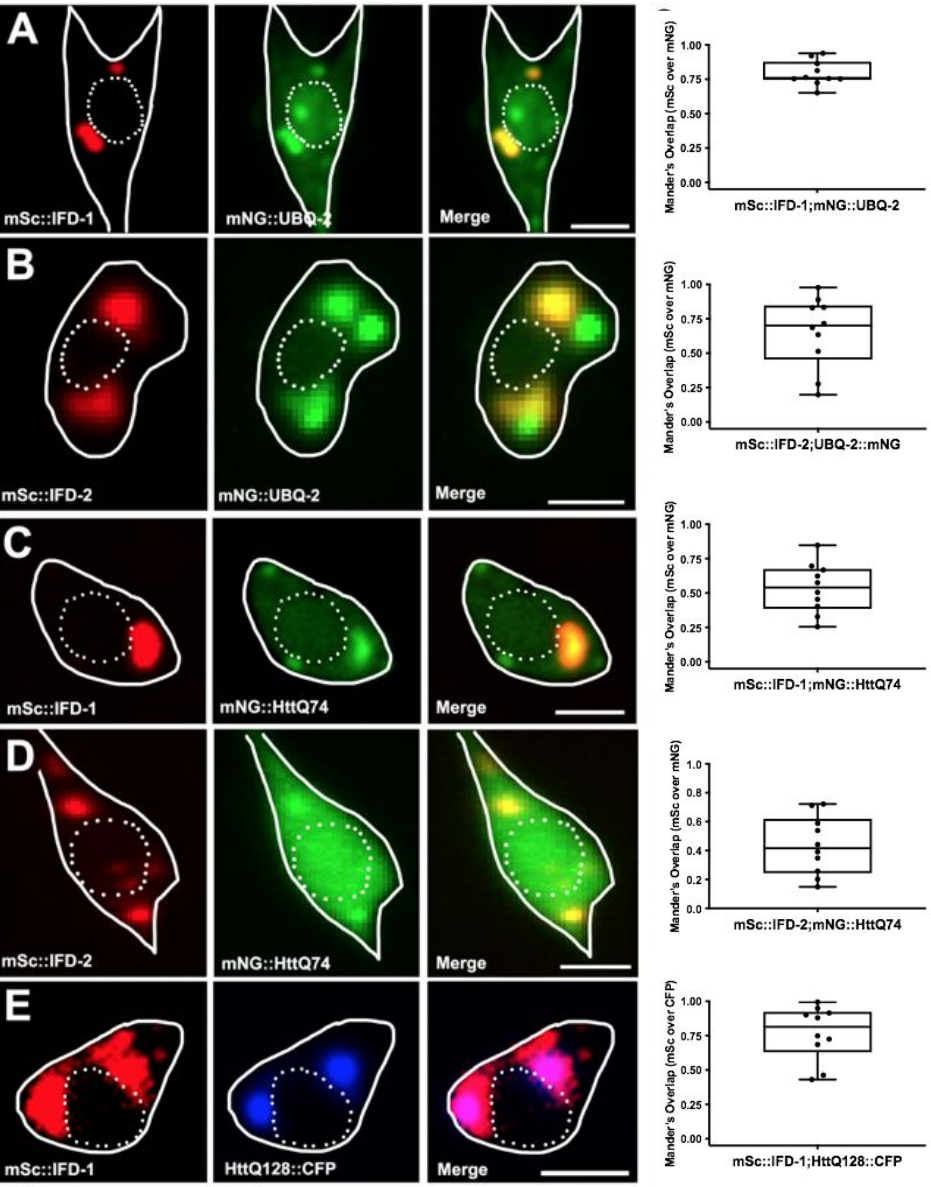

Arnold *et al.*, Figure 4

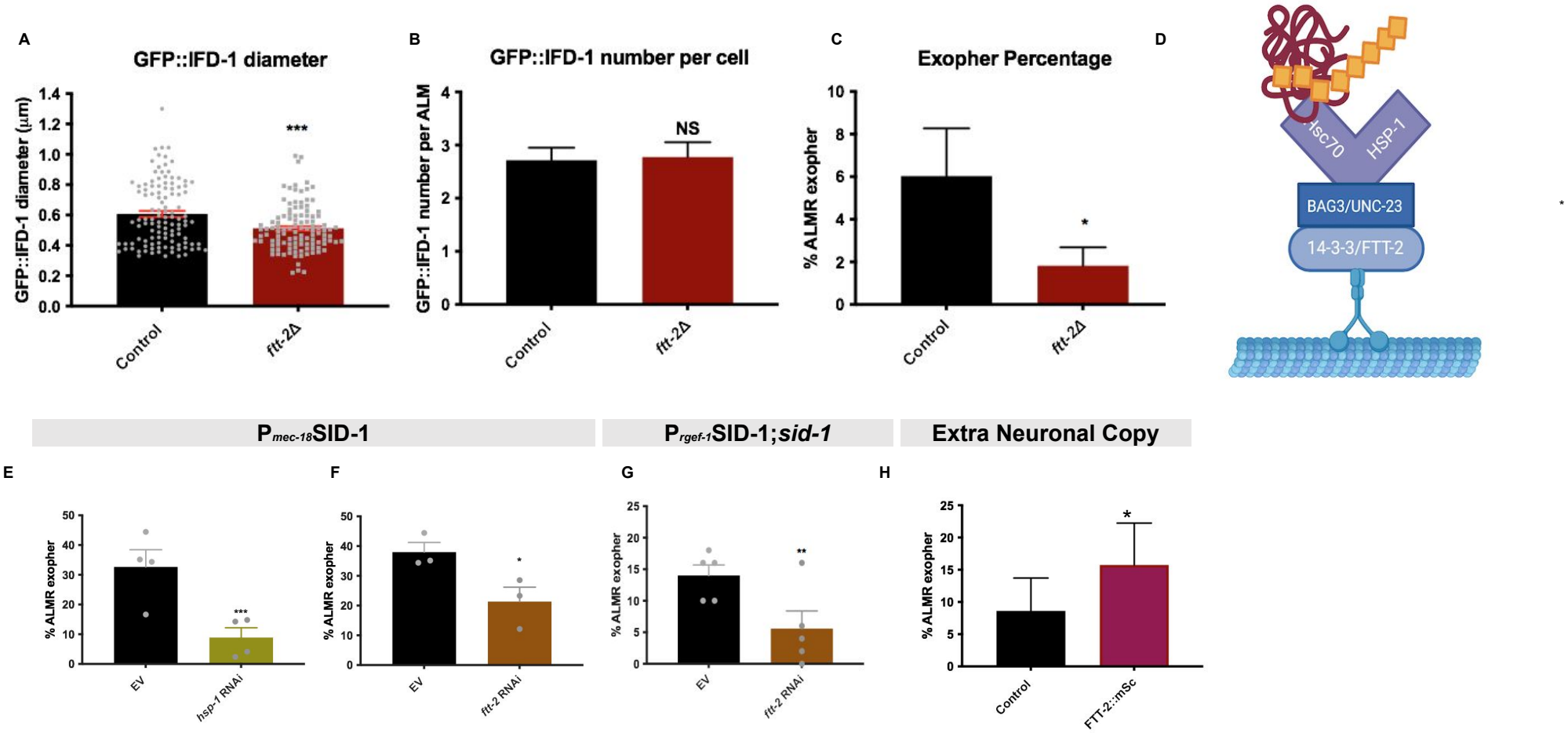

Arnold *et al.*, Figure 5

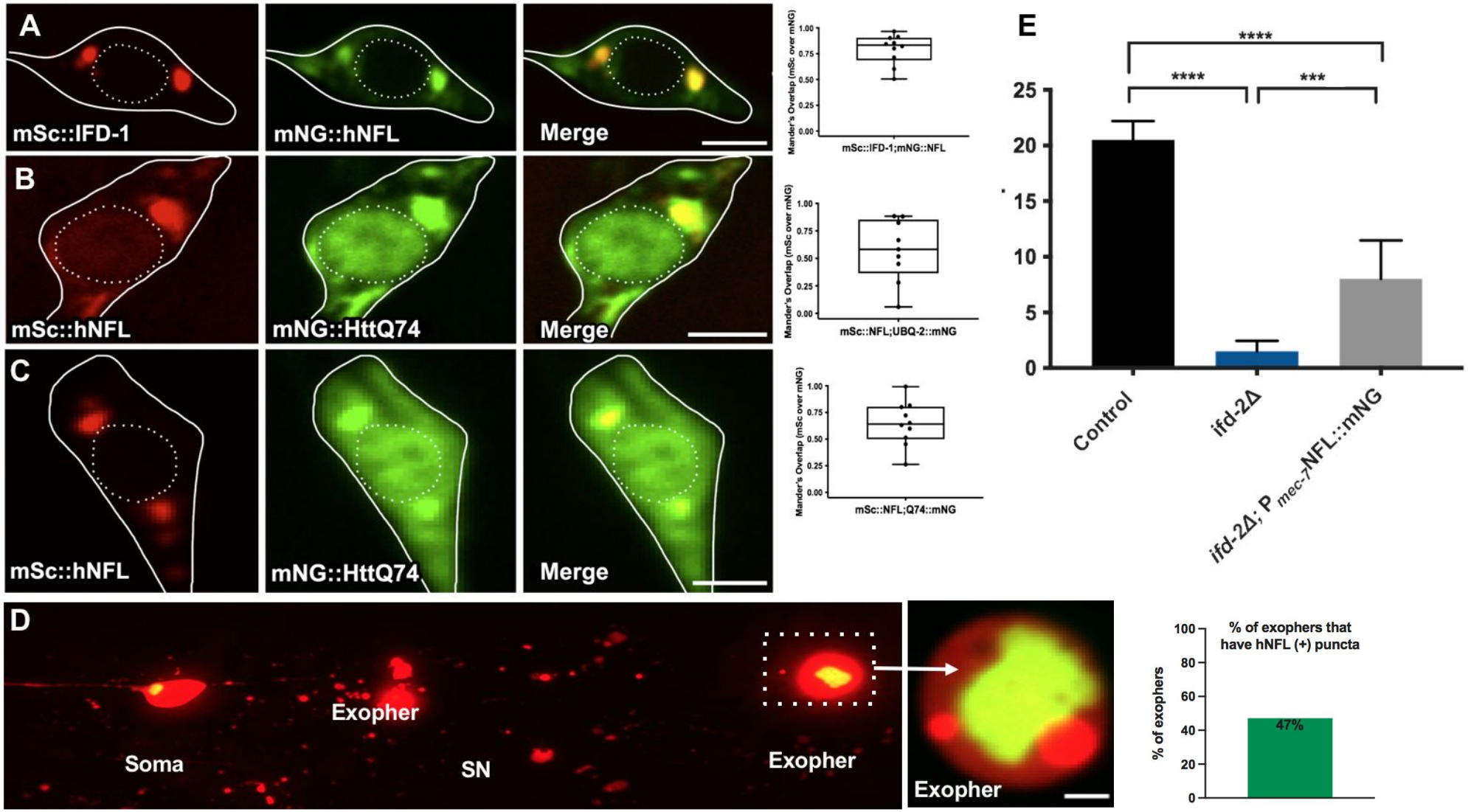

Arnold *et al.*, Figure 6

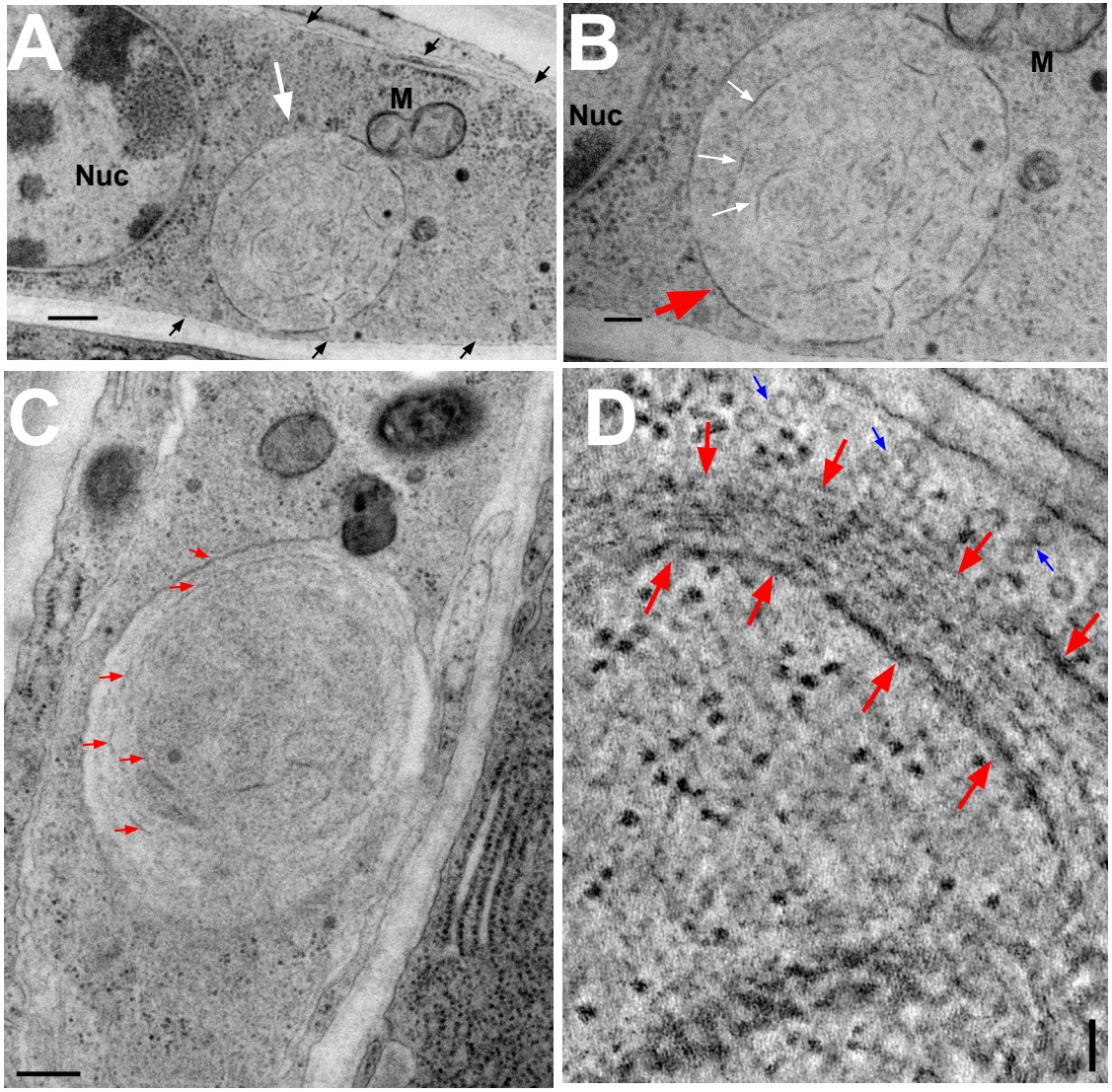

Arnold *et al.*,
Supplementary Figure 1

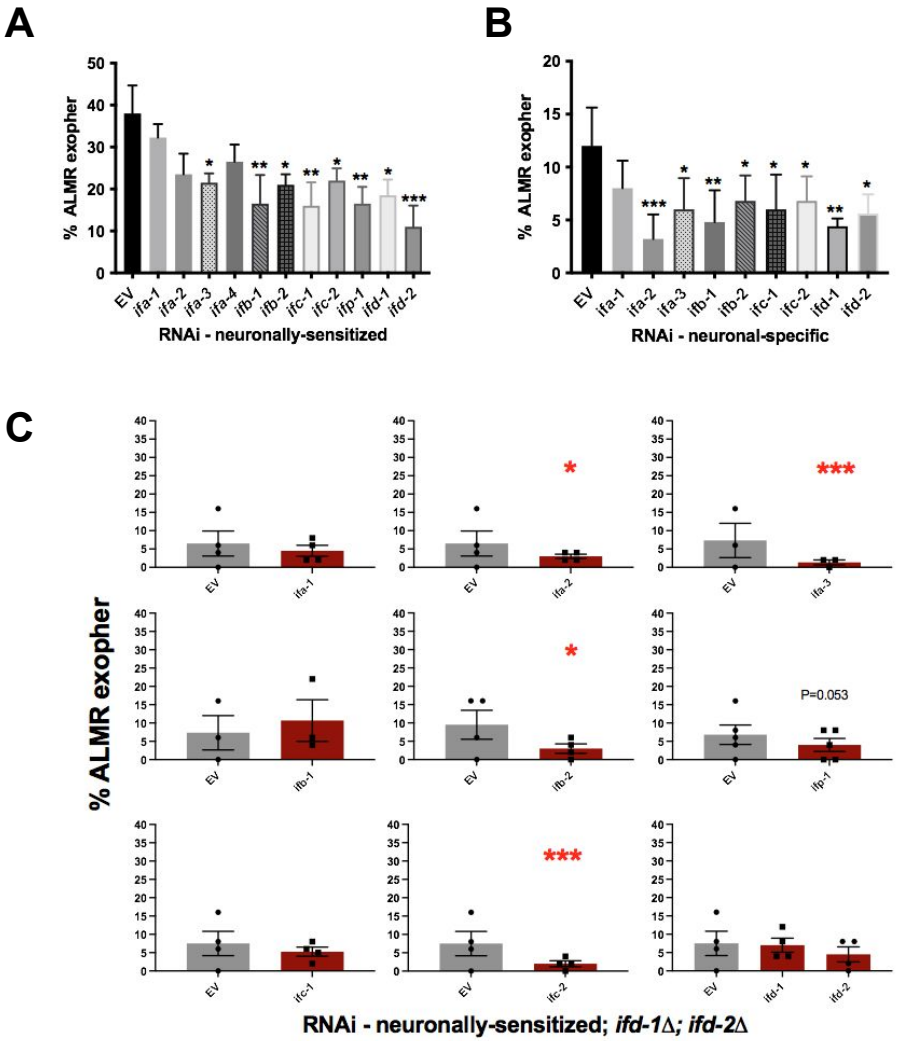

Arnold *et al.*,
Supplementary Figure 2

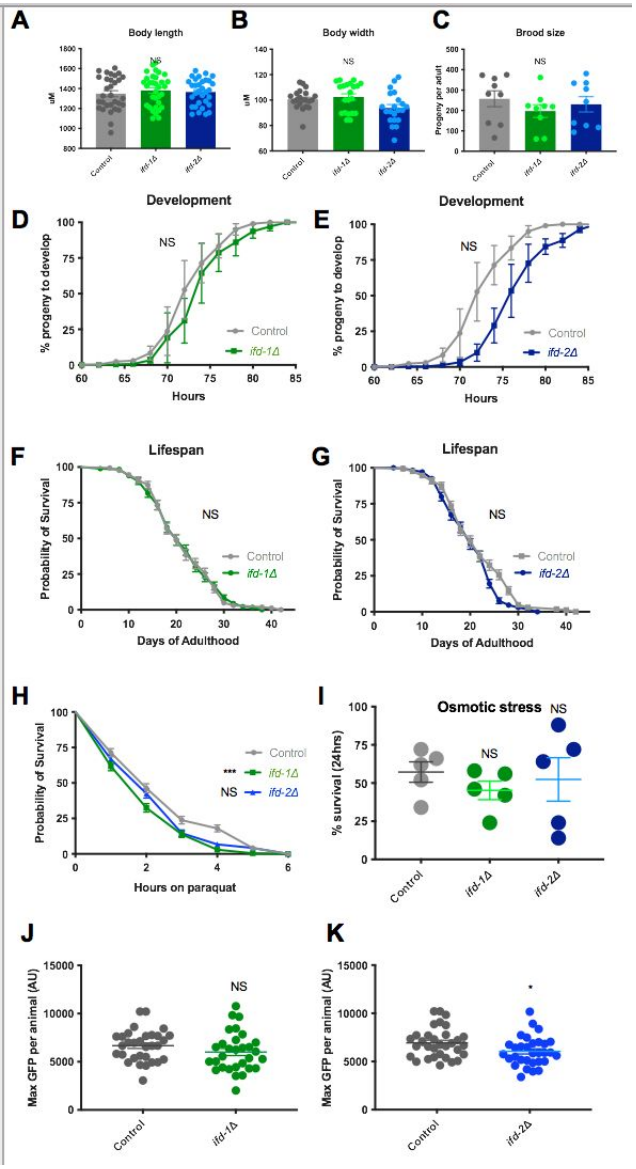

Arnold *et al.*,
Supplementary Figure 3

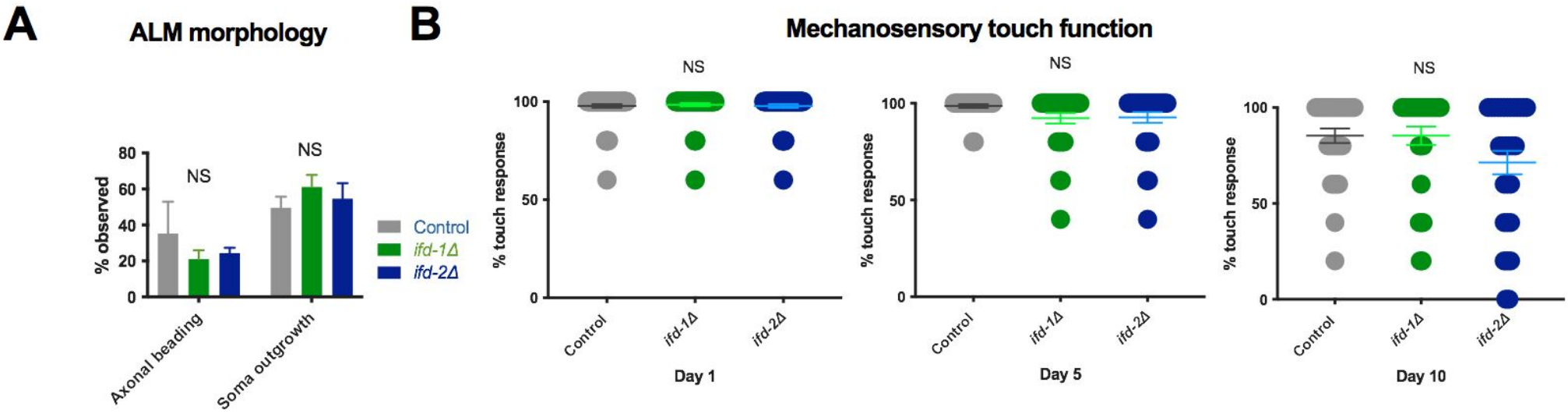

Arnold *et al.*,
Supplementary Figure 4

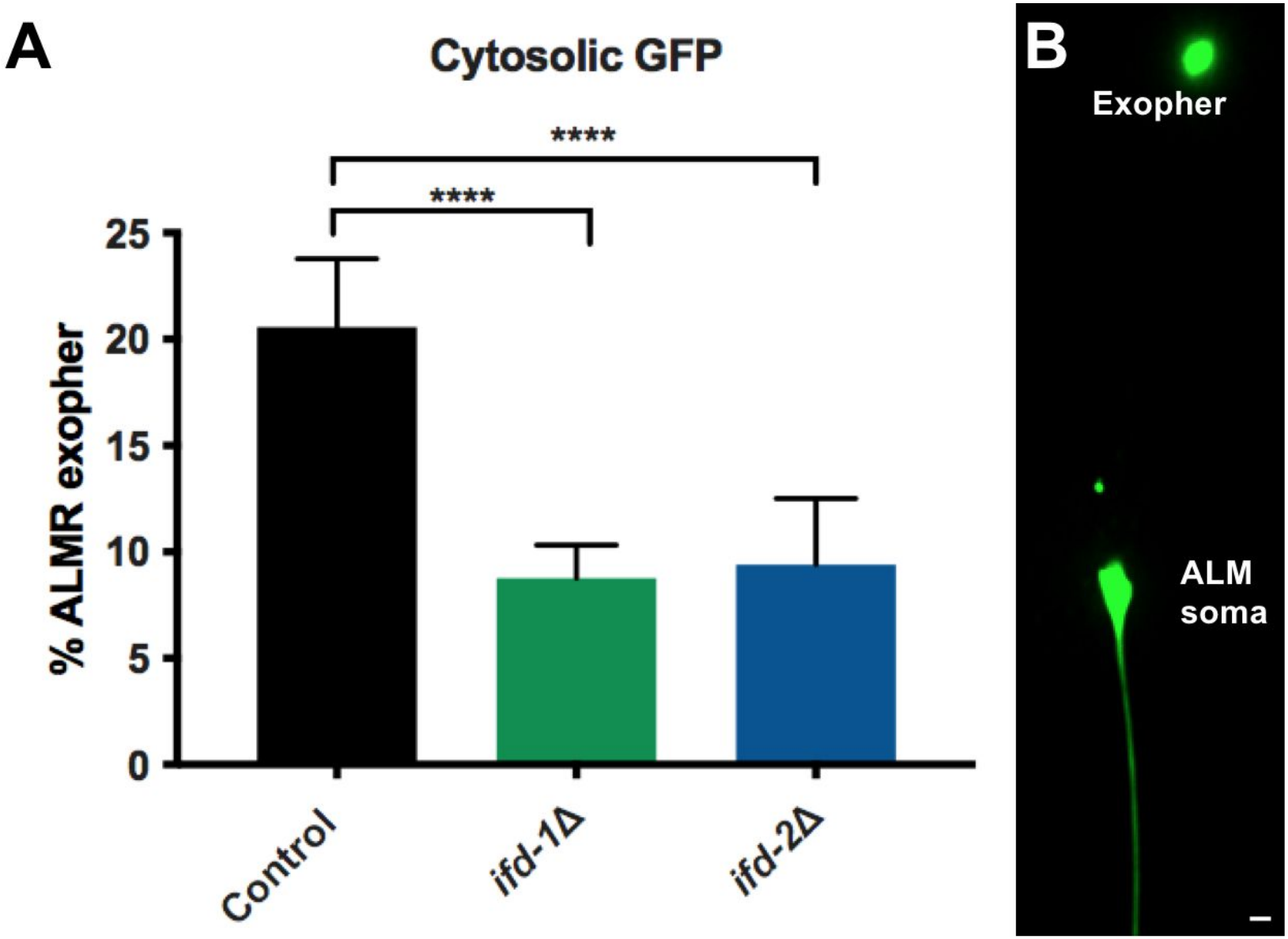

Arnold *et al.*,
Supplementary Figure 5

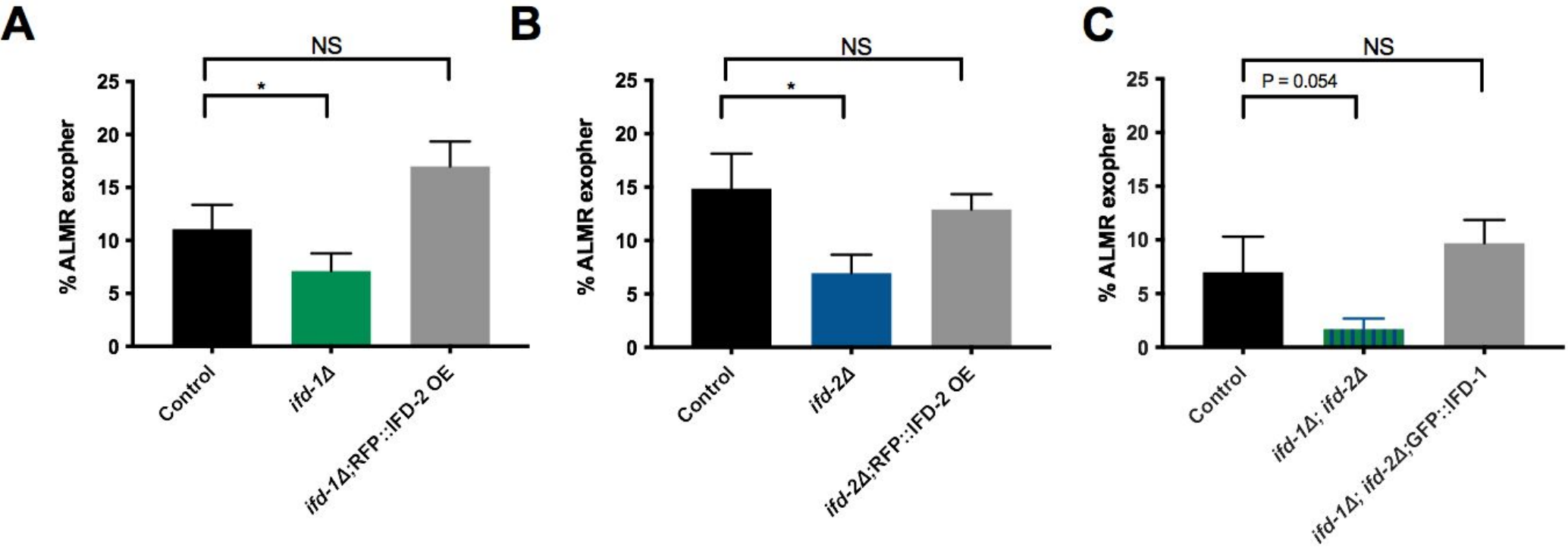

Arnold *et al.*,
Supplementary Figure 6

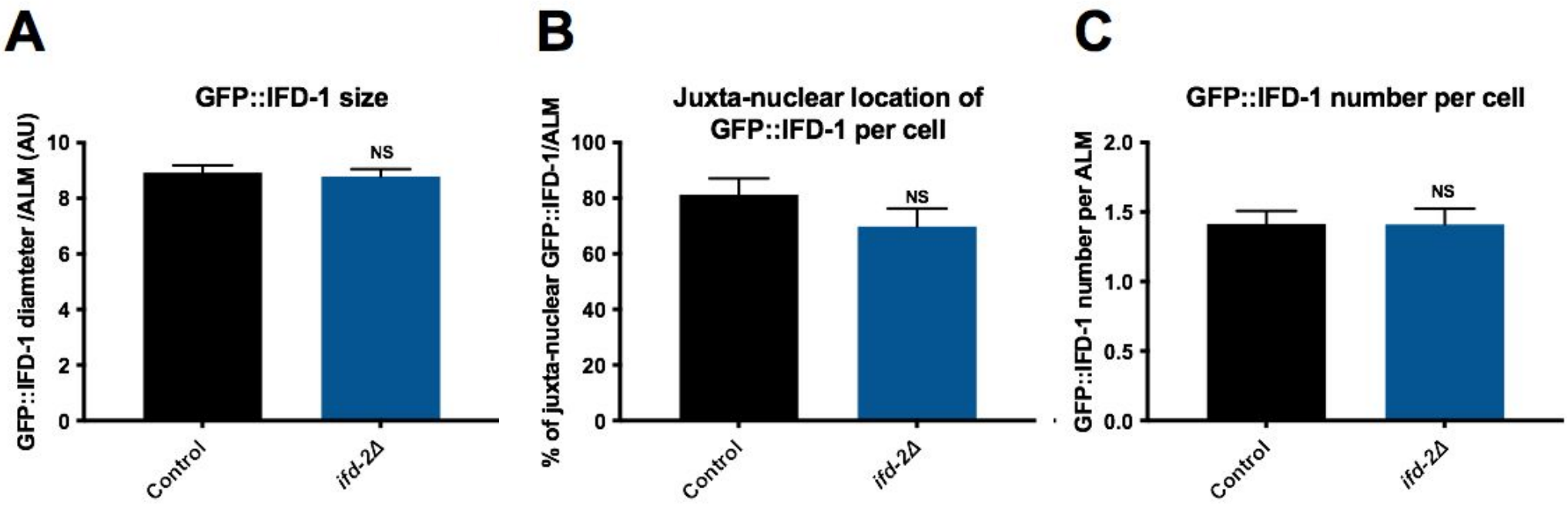

Arnold *et al.*,
Supplementary Figure 7

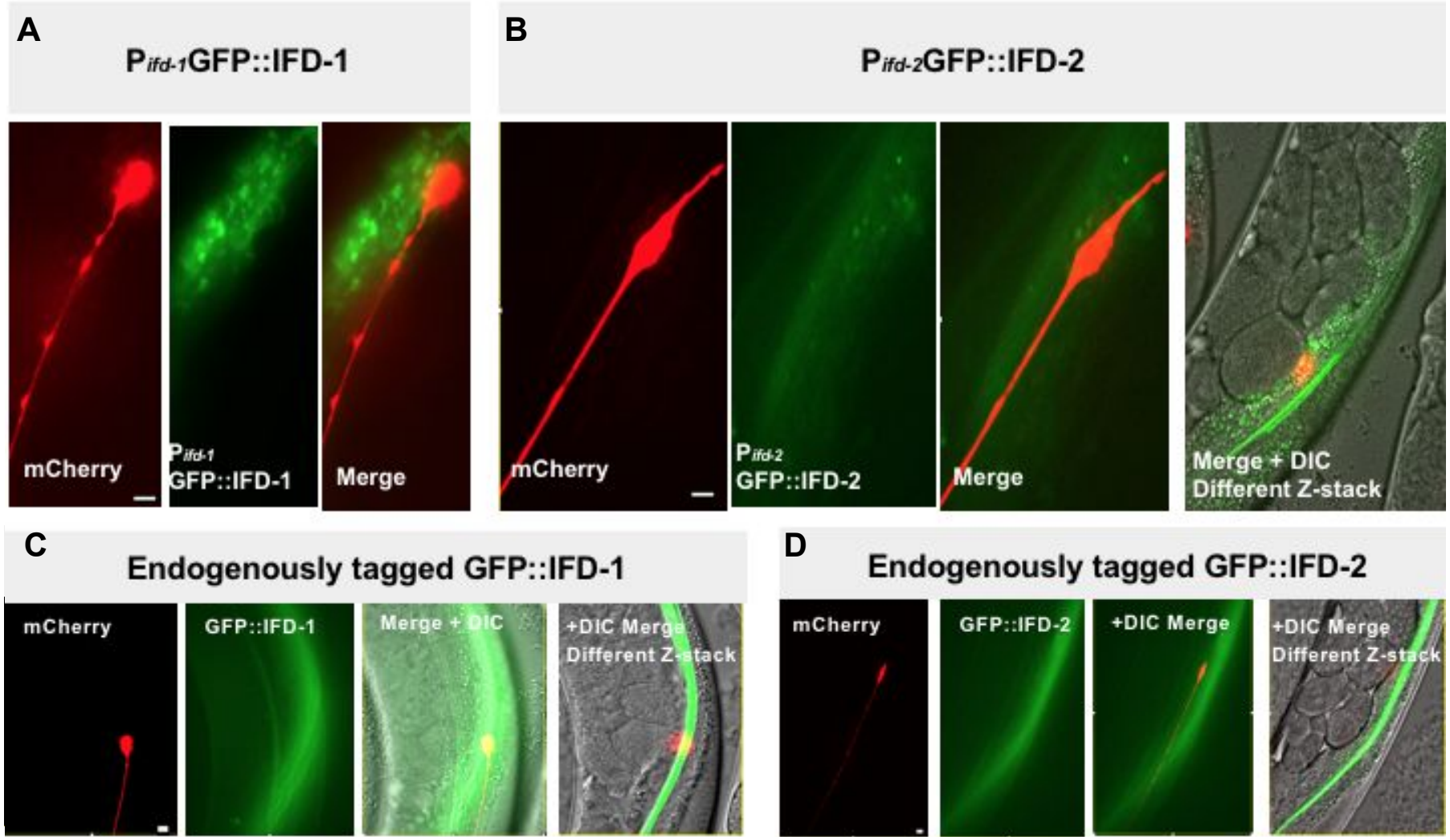

Arnold *et al.*,
Supplementary Figure 8

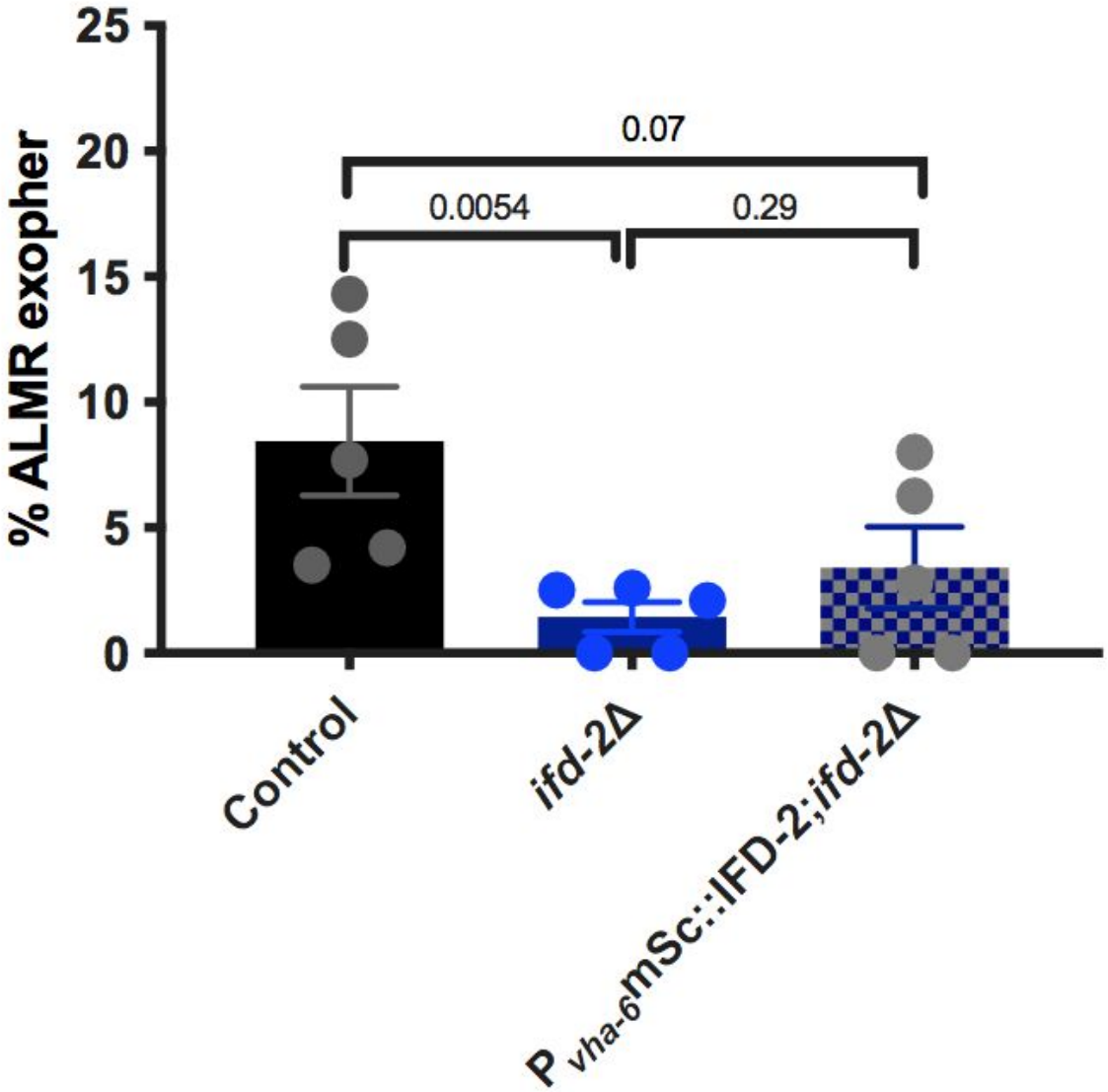

Arnold *et al.*,
Supplementary Figure 9

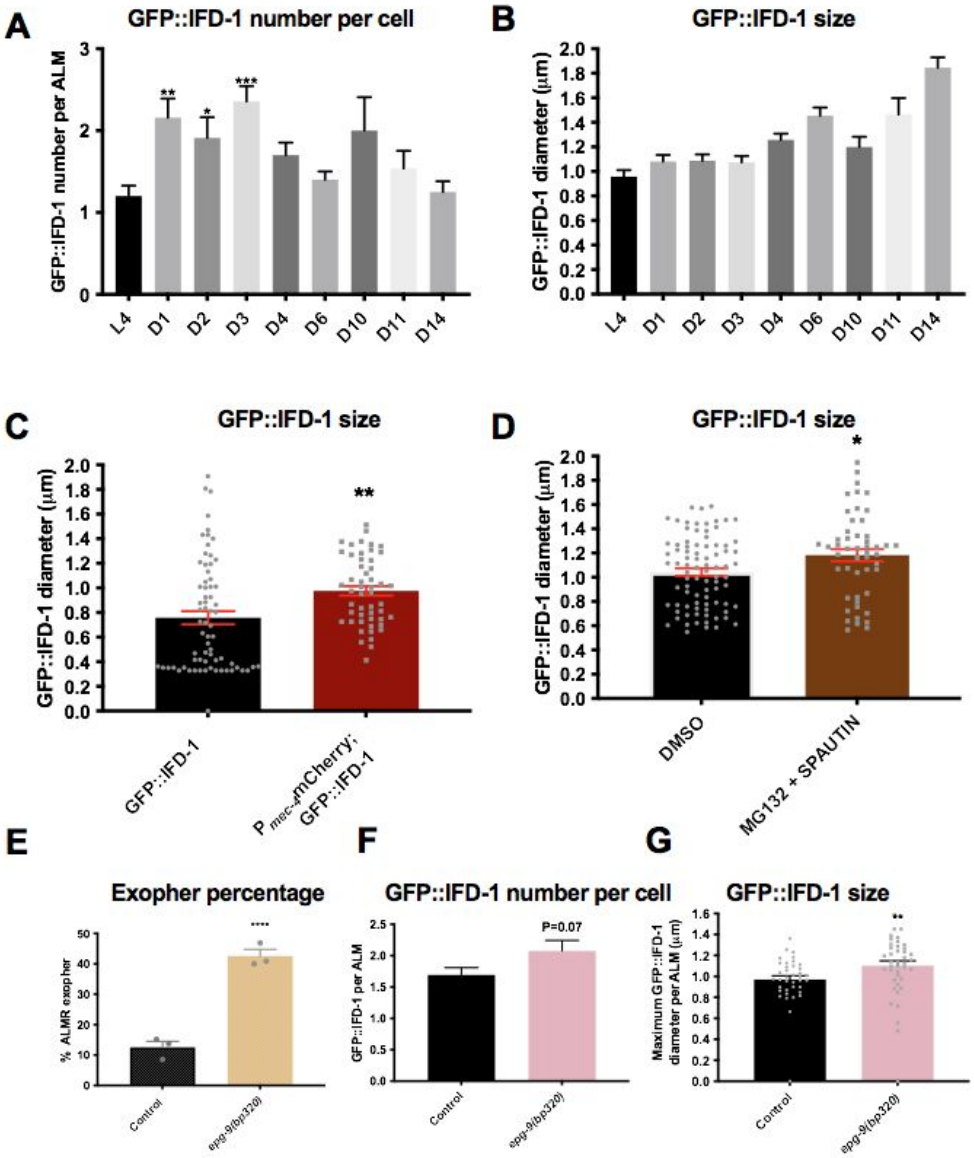

Arnold *et al.*,
Supplementary Figure 10

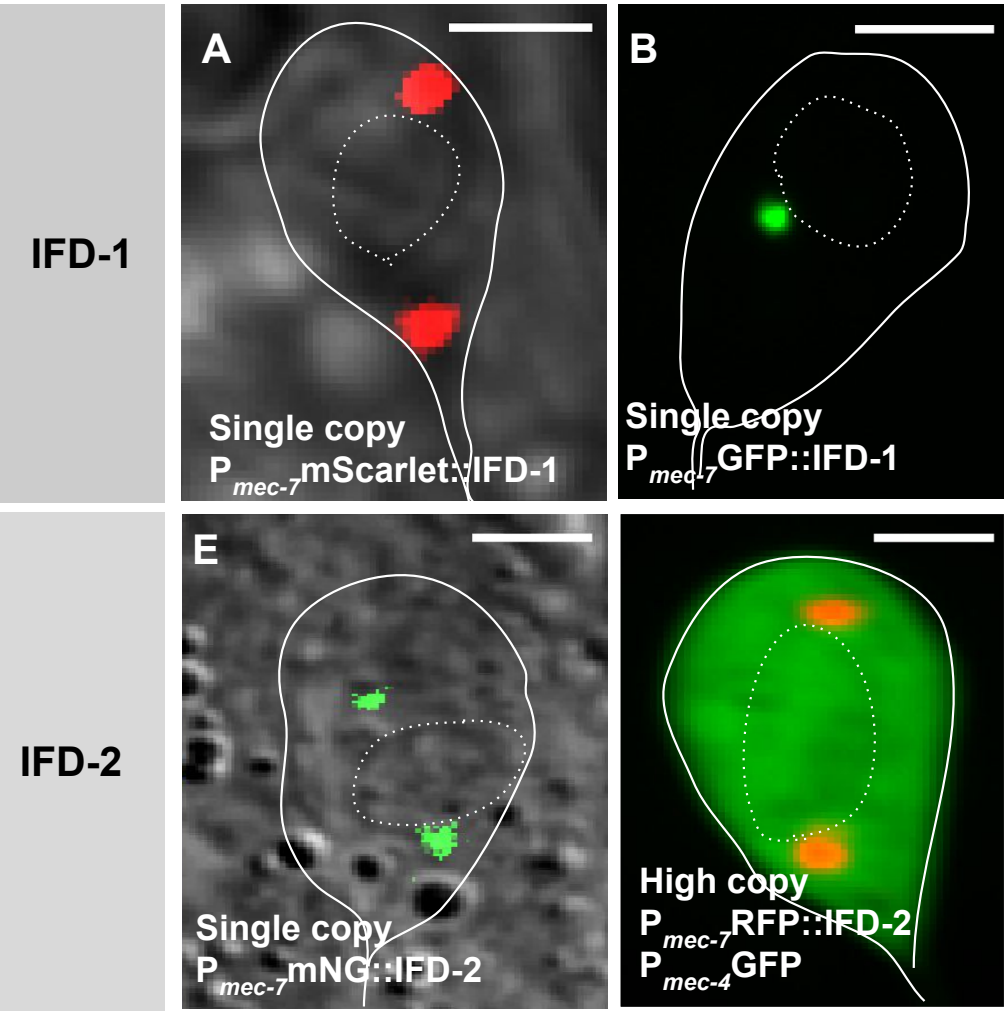

Arnold *et al.*,
Supplementary Figure 11

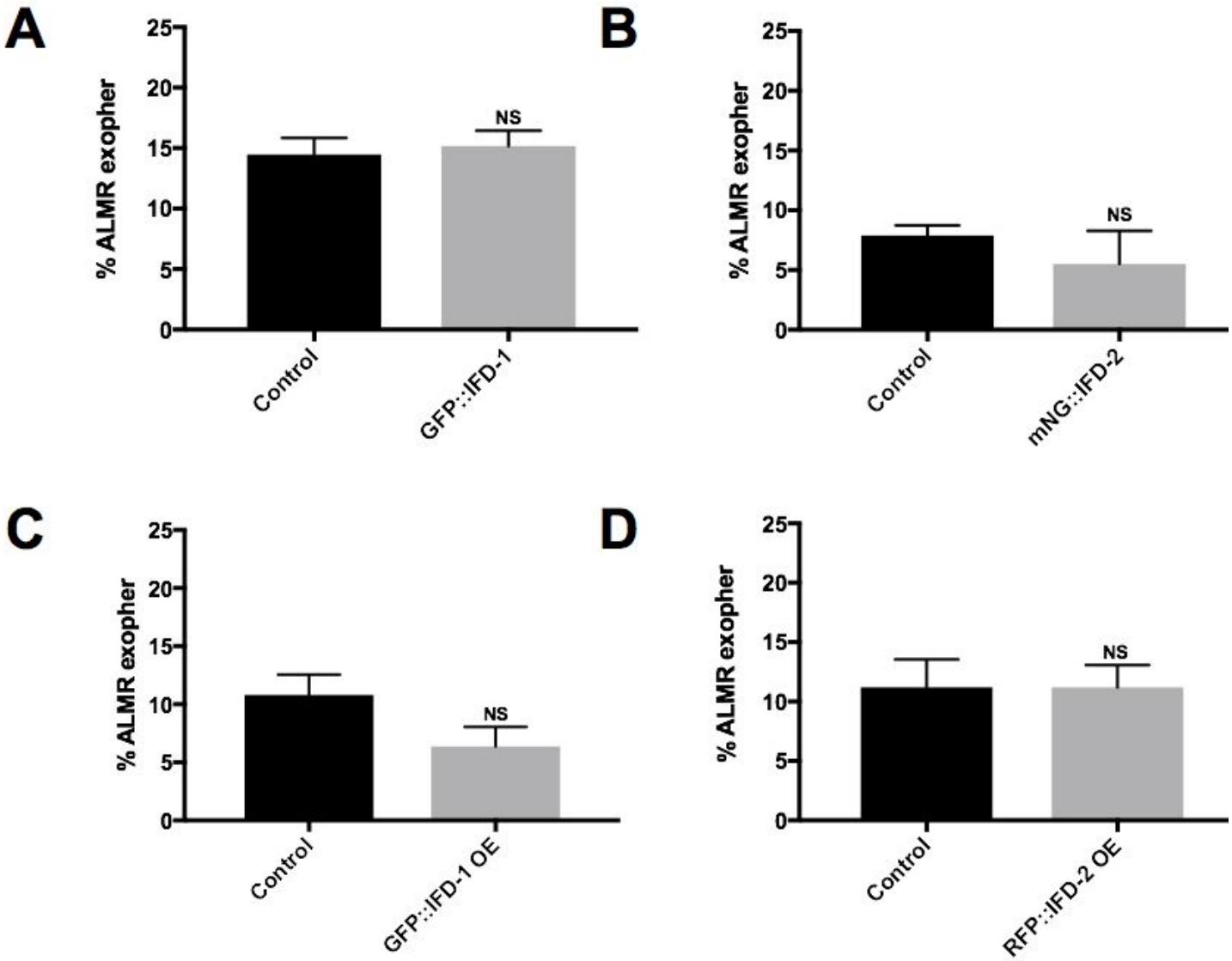

Arnold *et al.*,
Supplementary Figure 12

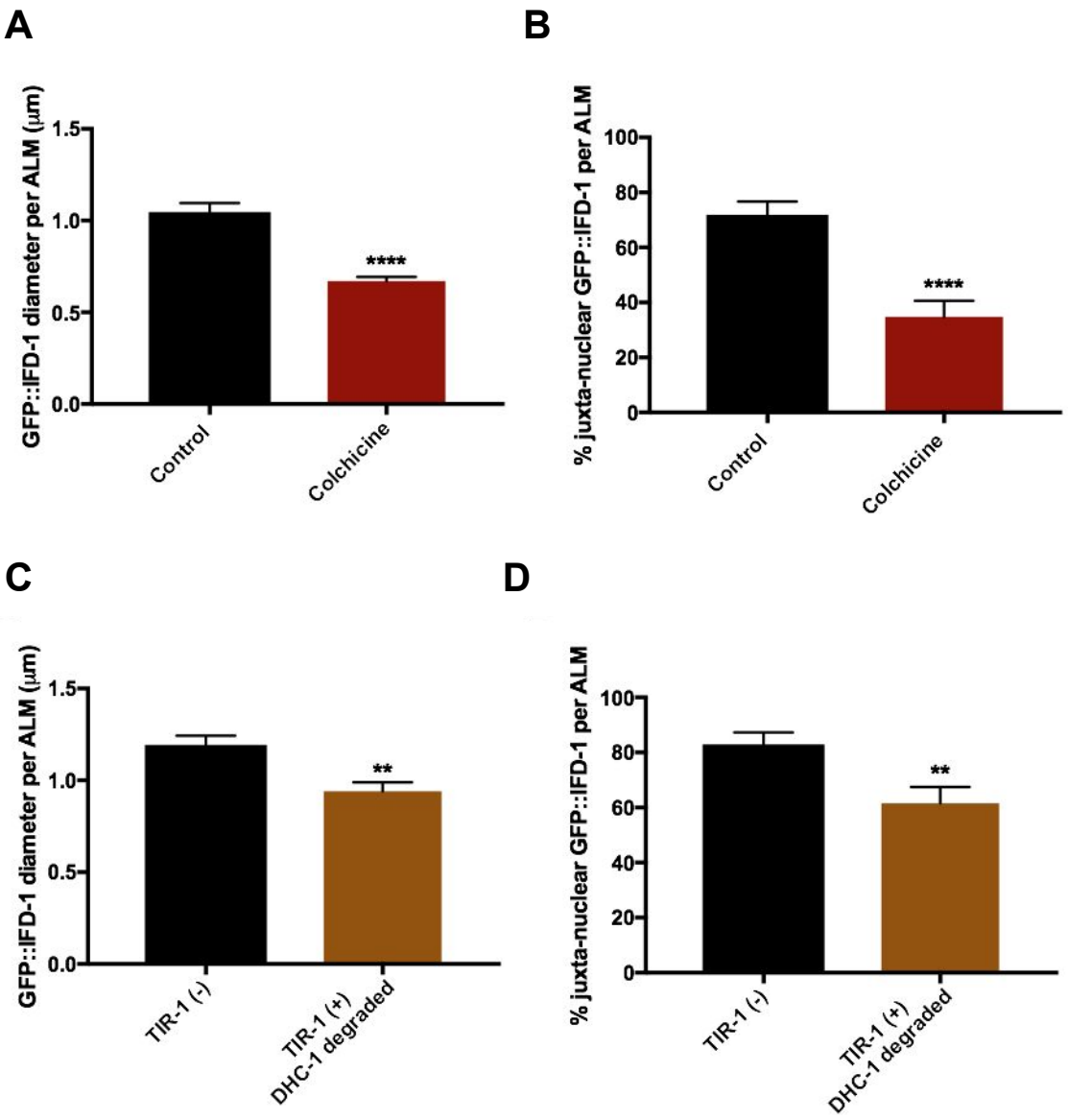

Arnold *et al.*,
Supplementary Figure 13

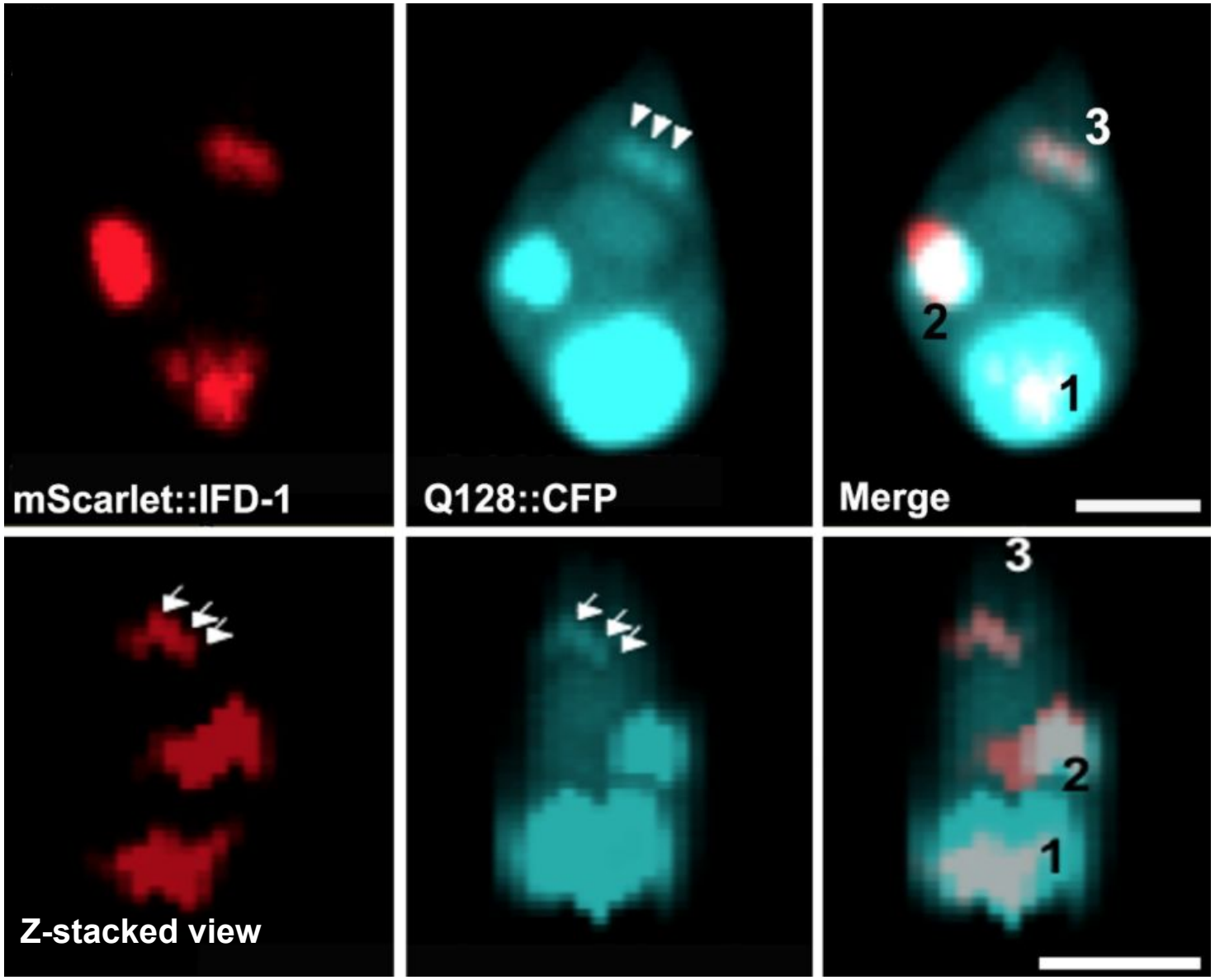

Arnold *et al.*,
Supplementary Figure 14

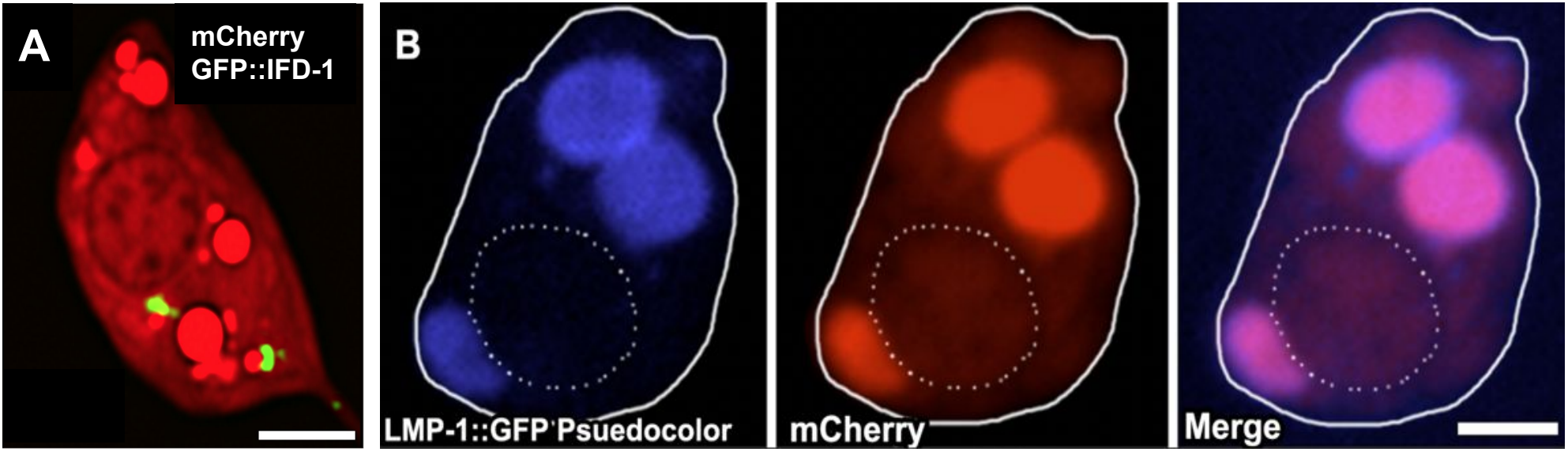

Arnold *et al.*,
Supplementary Figure 15

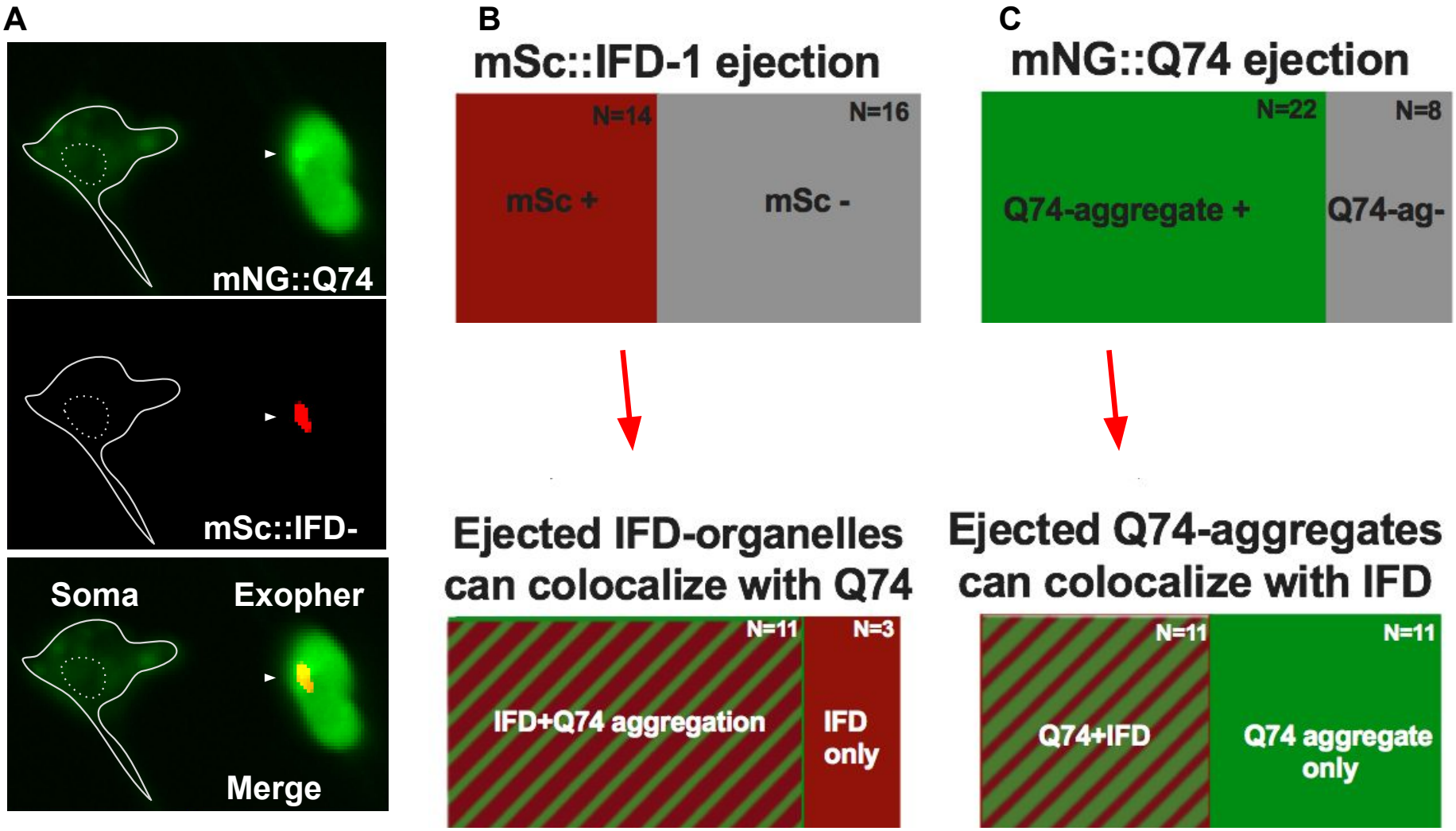

Arnold *et al.*,
Supplementary Figure 16

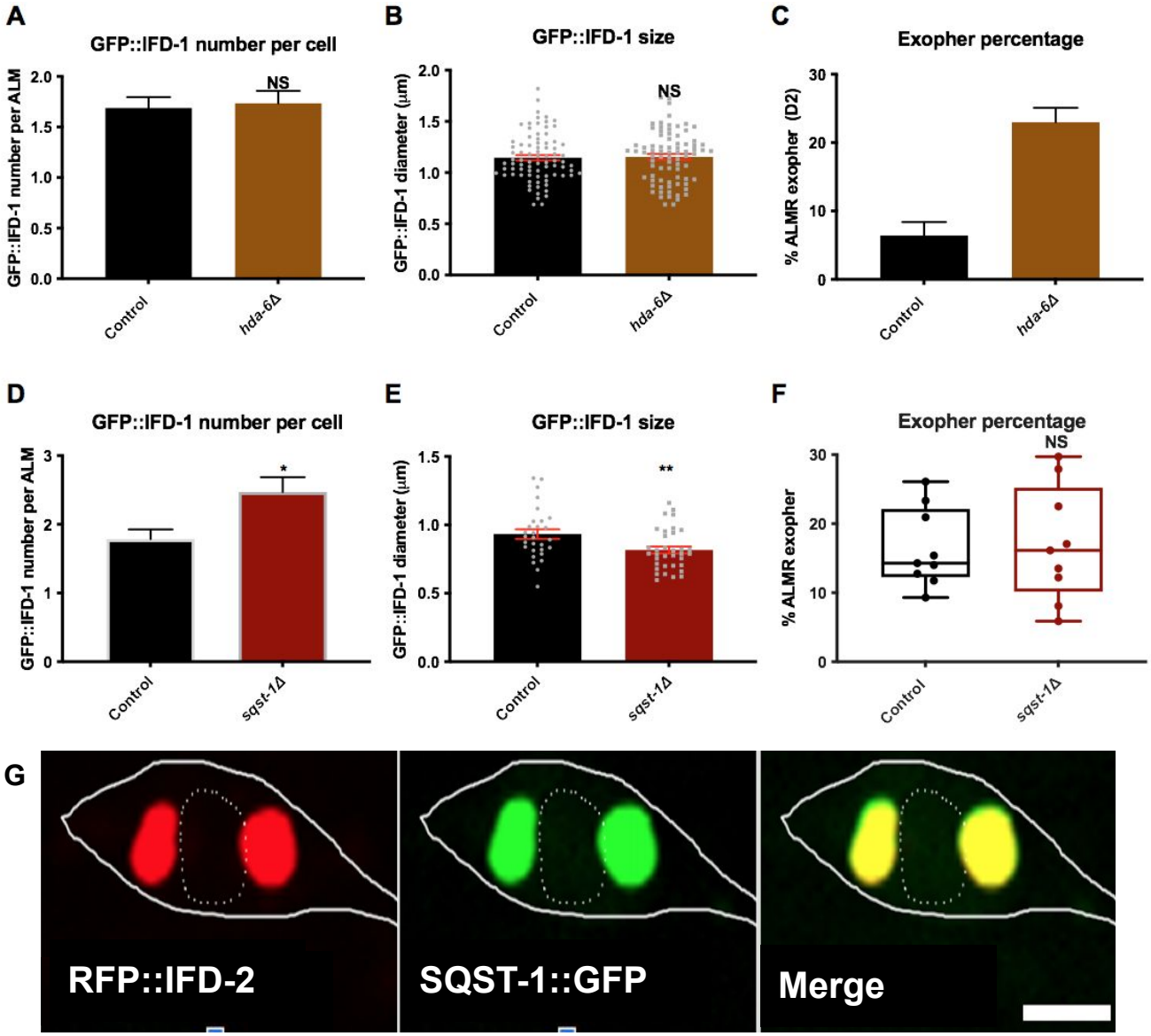

Arnold *et al.*,
Supplementary Figure 17

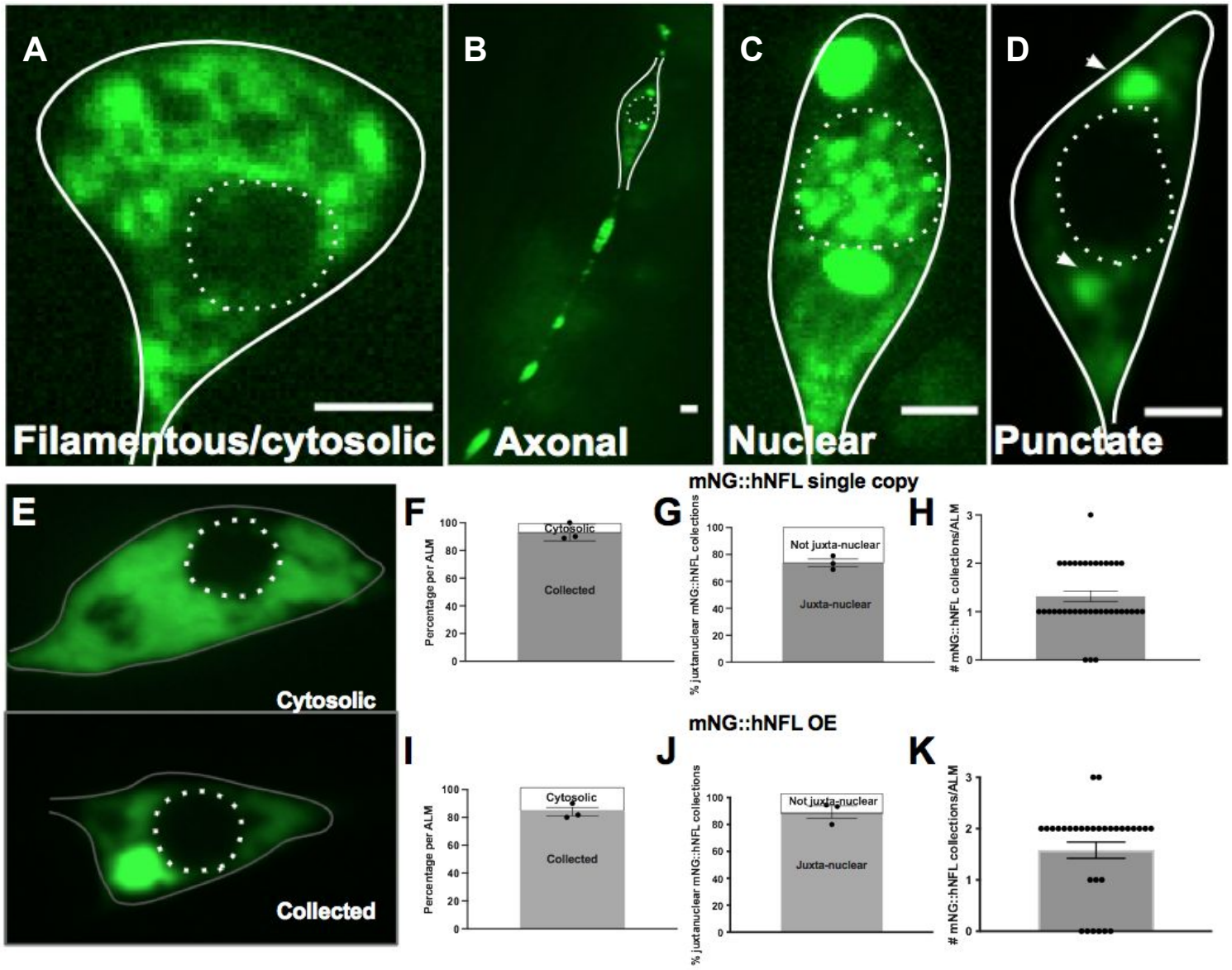

Arnold *et al.*,
Supplementary Figure 18

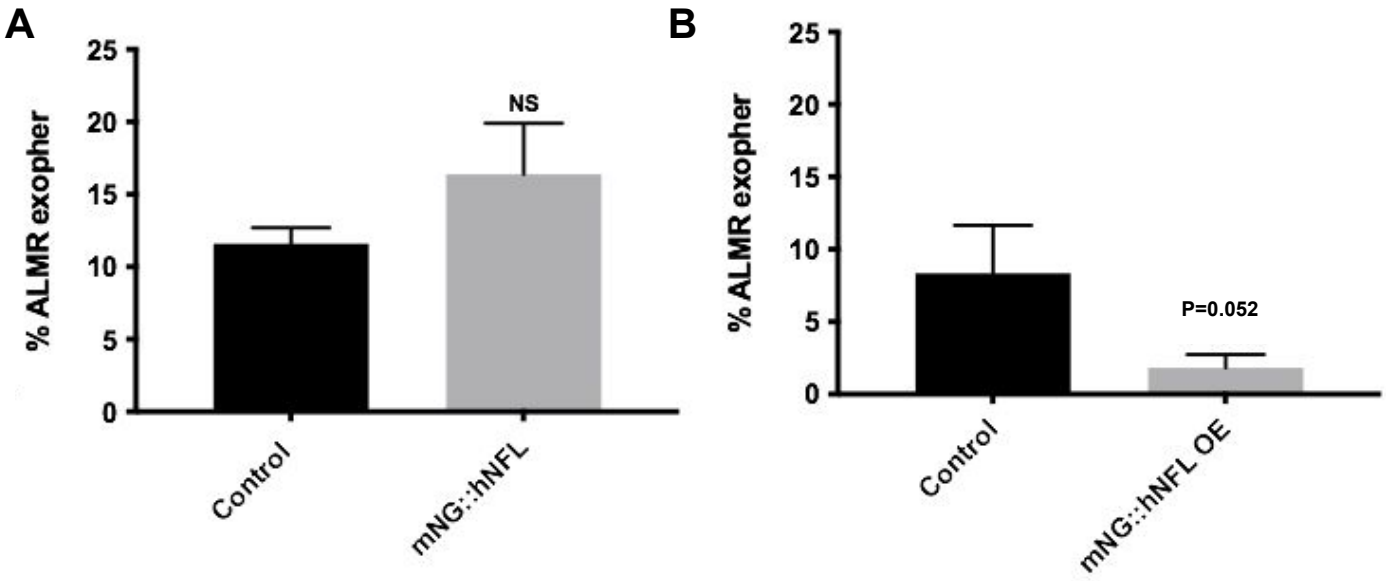

Arnold *et al.*,
Supplementary Figure 19

Video link 1: https://youtu.be/zMvtUJJbrzc
Video link 2: https://youtu.be/Gtex9gShdR8